CONVECTIVE MASS TRANSFER BETWEEN A HYDRODYNAMICALLY DEVELOPED AIRFLOW AND LIQUID WATER WITH AND WITHOUT A VAPOR PERMEABLE MEMBRANE

A Thesis Submitted to the College of

Graduate Studies and Research

in Partial Fulfillment of the Requirements

for the Degree of Master of Science

in the Department of Mechanical Engineering

University of Saskatchewan

Saskatoon

By

Conrad Raymond Iskra

PERMISSION TO USE

In presenting this thesis in partial fulfillment of the requirements for a Postgraduate degree from the University of Saskatchewan, I agree that the Libraries of this University may make it freely available for inspection. I further agree that permission for copying of this thesis in any manner, in whole or in part, for scholarly purposes may be granted by the professor who supervised my thesis work or, in his absence, by the Head of the Department or the Dean of the College in which my thesis work was done. It is understood that any copying or publication or use of this thesis or parts thereof for financial gain shall not be allowed without my written permission. It is also understood that due recognition shall be given to me and to the University of Saskatchewan in any scholarly use which may be made of any material in my thesis.

Requests for permission to copy or to make other use of material in this thesis in whole or part should be addressed to:

Head of the Department of Mechanical Engineering

University of Saskatchewan

Saskatoon, Saskatchewan, S7N 5A9

ABSTRACT

The convective mass transfer coefficient is determined for evaporation in a horizontal rectangular duct, which forms the test section of the transient moisture transfer (TMT) facility. In the test facility, a short pan is situated in the lower panel of the duct where a hydrodynamically fully developed laminar or turbulent airflow passes over the surface of the water. The measured convective mass transfer coefficients have uncertainties that are typically less than ±10% and are presented for Reynolds numbers (Re_D) between 560 and 8,100, Rayleigh numbers (Ra_D) between 6,100 and 82,500, inverse Graetz numbers (Gz) between 0.003 and 0.037, and operating conditions factors (H*) between -3.6 and -1.4. The measured convective mass transfer coefficients are found to increase as Re_D, Ra_D, Gz and H* increase and these effects are included in the Sherwood number (Sh_D) correlations presented in this thesis, which summarize the experimental data.

An analogy between heat and mass transfer is developed to determine the convective heat transfer coefficients from the experimentally determined Sh_D correlations. The convective heat transfer coefficient is found to be a function of Sh_D and the ratio between heat and moisture transfer potentials (S*) between the surface of the water and the airflow in the experiment. The analogy is used in the development of a new method that converts a pure heat transfer Nu_D (i.e., heat transfer with no mass transfer) and a pure mass transfer Sh_D (i.e., mass transfer with no heat transfer) into Nu_D and Sh_D that are for simultaneous heat and mass transfer. The method is used to convert a pure heat transfer Nu_D from the literature into the Nu_D and Sh_D numbers measured in this thesis. The results of the new method agree within experimental uncertainty bounds, while the

results of the traditional method do not, indicating that the new method is more applicable than the traditional analogy between heat and mass transfer during simultaneous heat and mass transfer.

A numerical model is developed that simulates convective heat and mass transfer for a vapor permeable Tyvek® membrane placed between an airflow and liquid water. The boundary conditions imposed on the surfaces of the membrane within the model are typical of the conditions that are present within the TMT facility. The convective heat and mass transfer coefficients measured in this thesis are applied in the model to determine the heat and moisture transfer through the membrane. The numerical results show that the membrane responds very quickly to a step change in temperature and relative humidity of the air stream. Since the transients occur over a short period of time (less than 1 minute), it is feasible to use a steady-state model to determine the heat and mass transfer rates through the material for HVAC applications.

The TMT facility is also used to measure the heat and moisture transfer through a vapor permeable Tyvek® membrane. The membrane is in contact with a water surface on its underside and air is passed over its top surface with convective boundary conditions. The experimental data are used to verify the numerically determined moisture transfer rate through the Tyvek® membrane. The numerical model is able to determine the mass transfer rates for a range of testing conditions within ±26% of the experimental data. The differences between the experiment and the model could be due to a slightly different mass transfer coefficient for flow over Tyvek® than for flow over a free water surface.

ACKNOWLEDGMENTS

I wish to thank my supervisor, Professor Carey J. Simonson, for his guidance, knowledge and inspiration throughout my undergraduate and graduate program at the University of Saskatchewan. I give thanks to my committee members (Professor R.W. Besant and Professor David Sumner) for their input in making this thesis a success.

I would like to thank my Mom and Dad and family for their love and support.

Appreciation is also extended to the University of Saskatchewan, CFI and NSERC SRO for their financial support.

DEDICATION

I dedicate this work to my parents, Raymond and Elaine Iskra, my sister, Mrs. Sherry Gibson and her loving family.

TABLE OF CONTENTS

page

LIST OF FIGURES

page

LIST OF TABLES

NOMENCLATURE

ACRONYMS

CFD computational fluid dynamics

RH relative humidity

SEE standard error estimate of a curve fit

TMT transient moisture transfer

ENGLISH SYMBOLS

A_s area of evaporating surface [m^2]

a width of the rectangular channel [m] (Lin et al., 1992), or one-half the distance between the top and bottom walls [m] (Lyczkowski et al., 1981)

b height of the rectangular channel [m] (Lin et al., 1992), or one-half the distance between the side walls (Lyczkowski et al., 1981)

C dimensionless species concentration (Yan, 1996)

C_{peff} effective specific heat capacity [J/kg·K]

C_p specific heat capacity [J/kg·K]

D inside diameter of circular duct [m], or mass diffusivity [m^2/s] (Lin et al., 1992; Yan, 1996), or diameter of cylindrical container [m] (Prata and Sparrow, 1986), or hydraulic diameter of the flow cross-section of the mass transfer section [m] (Chuck and Sparrow, 1987)

$\mathcal{D}$ binary mass diffusion coefficient [m^2/s] (Prata and Sparrow, 1986; Chuck and Sparrow, 1987)

D_{AB} binary mass diffusion coefficient [m^2/s]

D_e equivalent hydraulic diameter [m] (Yan, 1996; Lin et al., 1992)

D_{eff} effective vapor diffusion coefficient [m^2/s]

D_h hydraulic diameter of rectangular duct [m]

d average distance between the bottom of the pan and the water surface [m], or diameter of the Tyvek® fibers [m], or pan diameter [m] (Pauken, 1999)

Gr_m mass transfer Grashof number [Ra_D/Sc], or definition given by Lin et al. (1992), or denifintion given by Pauken (1999)

Gr_t heat transfer Grashof number (Lin et al., 1992)

Gz Graetz number

g gravitational acceleration [m/s^2]

H height of rectangular duct [m]

H* dimensionless operating condition factor that represents the ratio of latent to sensible energy differences between the air stream and the air in equilibrium with the water surface

h average distance between the water surface and top of pan [m], or heat transfer coefficient [$W/m^2 \cdot K$] (Lyczkowski et al., 1981)

$\bar{h}$ average heat transfer coefficient [$W/m^2 \cdot K$] (Yan, 1996)

h_{fg} enthalpy of vaporization [J/kg]

h_h convective heat transfer coefficient [$W/m^2 \cdot K$]

h_m convective mass transfer coefficient [m/s], or local mass transfer coefficient (Lin et al. 1992)

$\bar{h}_m$ average mass transfer coefficient [m/s] (Yan, 1996)

K mass transfer coefficient (Chuck and Sparrow, 1987; Prata and Sparrow, 1986)

k	thermal conductivity [W/m·K]
L	length of water pan [m], or thickness of the Tyvek® membrane [m], or Characteristic length [m] (Pauken, 1999), or streamwise length of the pan [m] (Chuck and Sparrow, 1987)
l	distance between the first and last static pressure tap immediately upstream of the test section [m]
ℓ	length of an elementary volume [m]
m	mass of moist Tyvek® [kg]
$\dot{m}$	mass flowrate of air [kg/s], or rate of phase change [kg/m^3·s]
m_{dry}	mass of dry Tyvek® [kg]
$\dot{m}_{evap}$	evaporation rate of water [kg/s]
m_{ss}	steady state mass transfer rate [kg/s]
N	buoyancy ratio (Yan, 1996)
Nu	Nusselt number
Nu_D	Nusselt number (based on the hydraulic diameter of the test section duct)
Nu_h	Nusselt number (based on pure heat transfer conditions)
$Nu_{h/m}$	Nusselt number (based on simultaneous heat and mass transfer conditions)
P	duct perimeter [m]
Pr	Prandtl number
p_{sat}	saturated water vapor pressure [Pa]
p	pressure [Pa]
Δp	pressure drop across the orifice plate [Pa]

q_e external energy transfer from the TMT surroundings [W]

q_l latent energy transfer from the evaporation of water [W]

q_s sensible energy transfer from the airflow [W]

R ideal gas constant [J/kg·K]

Ra_D Rayleigh number (based on the hydraulic diameter of the test section duct)

Ra^+ effective Rayleigh number (Lin et al.,1992)

Ra_d Rayleigh number (based on the average depth of water in the pan)

Re Reynolds number

Re_D Reynolds number (based on the hydraulic diameter of the test section duct)

Re_u Reynolds number (based on the hydraulic diameter of the duct immediately upstream of the test section)

r^2 correlation coefficient

S* dimensionless parameter that represents the ratio between mass and heat transfer

Sc Schmidt number

Sh Sherwood number

Sh_D Sherwood number (based on the hydraulic diameter of the test section duct)

$Sh_{h/m}$ Sherwood number (based on simultaneous heat and mass transfer conditions)

Sh_m Sherwood number (based on pure mass transfer conditions)

Sh_Z local Sherwood number (Lin et al., 1992)

T temperature [K]

ΔT temperature difference between the surface of the water and the air entering the test section [K]

t time [h], or time [s]

t Student t value at a 95% confidence level

Δt time step [s]

U uncertainty at a 95% confidence level

U_m overall mass transfer resistance [m/s]

u mass of moisture adsorbed per kg of dry Tyvek® [kg/kg]

$\bar{u}$ mean velocity of air flow in duct [m/s] (Prata and Sparrow, 1986)

V local velocity of air within the duct immediately upstream of the test section [m/s], or air velocity (Pauken, 1999)

V_{max} maximum velocity of air within the duct immediately upstream of the test section [m/s]

W width of duct [m]

ΔW humidity ratio difference between the surface of the water and the air entering the test section [kg/kg]

w width of water pan [m]

X distance from the water side of the membrane towards the air side of the membrane [m]

X* a dimensionless coordinate parallel to flow (equivalent to Gz^{-1}), which is a function of Sc

X_h^* a dimensionless coordinate parallel to flow (equivalent to Gz^{-1}), which is a function of Pr

ΔX grid size [m]

x horizontal distance along the flow direction of the duct immediately upstream of the test section [m]

y vertical distance from the bottom of the duct that is immediately upstream of the test section [m]

Z horizontal distance along the water surface in the airflow direction [mm]

GREEK SYMBOLS

α thermal diffusivity [m^2/s]

β thermal expansion coefficient [K^{-1}]

β^* coefficient of concentration expansion (Yan, 1996)

ε volume fraction

ϕ relative humidity of the ambient air

γ aspect ratio = W/H

μ dynamic viscosity [$N \cdot s/m^2$]

ν kinematic viscosity [m^2/s]

ρ density [kg/m^3]

$\rho_{v,a}$ vapor density of the air

ρ_{sat} saturated water vapor density [kg/m^3]

$\Delta\rho_v$ log-mean water vapor density difference [kg/m^3]

$\overline{\rho}$ mean mixture density of air [kg/m^3]

SUBSCRIPTS

1 bulk properties of air entering the test section

2 bulk properties of air leaving the test section

a dry air properties, or characteristic value in air (Pauken, 1999)

b	properties of the water at the bottom of the pan
d	property across the membrane fiber
dry	property containing no moisture
eff	effective property
f	film property (average of free stream and surface)
g	moist air property including dry air and water vapor, or gas, or referring to the fluid in the duct (Lyczkowski et al., 1981)
i	is an index where i = 1 at the inlet and i = 2 at the outlet of the test section, or characteristic value at the interface (Pauken, 1999)
∞	average properties across the test section
L	property across the membrane thickness
ℓ	property across the representative elementary volume
l	liquid
lm	log mean
o	property at the inlet of the duct (Yan, 1996)
s	properties at the surface of the water, or solid
w	value at the wall of the duct (Yan, 1996)
y	referring to the y-direction (Lyczkowski et al. 1981)
v	water vapor

CHAPTER 1

INTRODUCTION

1.1 Introduction

This thesis presents a numerical and experimental analysis of convective heat and mass transfer between an airflow and liquid water with and without a water vapor permeable membrane. The surface transfer coefficients of a rectangular duct within the test section of the transient moisture transfer (TMT) facility are measured by evaporative mass transfer. Evaporative mass transfer is also analyzed when a vapor permeable membrane is placed between the airflow and the water surface. The heat and water vapor transfer information gained for this membrane can be used in the development of a radiative type enthalpy exchanger. The membrane would act as the component of the enthalpy exchanger where the transfer of heat and water vapor occurs.

1.2 Convective Mass Transfer Coefficient

In this thesis, a fundamental problem of laminar and turbulent forced convective steady-state evaporation in a horizontal rectangular duct is examined. A rectangular container that is full of water is situated in the bottom panel of the rectangular duct. The water surface forms the base of the duct, where an airflow is passed over the surface of the water. The objective of this study is to measure the evaporation mass transfer that occurs and relate this to the geometrical and hydrodynamic flow conditions.

Evaporative mass transfer is a result of combined heat and mass transfer processes. The vapor above the surface of water is in equilibrium with the liquid phase, where the water vapor density at the surface of the water is larger than in the airflow above it. It is this difference that creates the driving potential for mass transfer of water vapor from the surface of the water to the airflow. As the water vapor above the surface is drawn into the airflow, liquid water is transformed into a gaseous state, which keeps the liquid water and vapor phases in equilibrium with each other. The change in phase from liquid to vapor is a result of the sensible heat exchange from the airflow to the surface of the water.

Due to the mass transfer of water vapor at the surface of the duct, a convective mass transfer coefficient can be measured. The convective mass transfer coefficient is an important parameter, since it is a measure of the resistance to mass transfer between the fluid flowing in the duct and the surface of the duct. The convective coefficient depends on the hydrodynamic, thermal and concentration boundary layers and is an important parameter when studying moisture and contaminant transfer between flowing air and porous media (Olutimayin and Simonson, 2005 and Osanyintola et al., 2005 and Zhang and Niu, 2003 and Zhang, 2006), as well as condensation and frosting in heat exchangers (Xia and Jacobi, 2005 and Sadek et al., 2006 and Yun et al., 2005). Despite its importance, there are few experimental data available in the literature on convective mass transfer coefficients for ducts. In most cases, convective heat transfer coefficients have been measured and an analogy between heat and mass transfer is used to determine the convective mass transfer coefficient.

1.2.1 Literature Review

A literature review shows that the present problem has been studied extensively, but there are still areas of study that have not been considered. The following literature review presents experimental and numerical work for both laminar and turbulent airflows for determining either convective heat or mass transfer coefficients for rectangular ducts. Based on this literature review, the areas of research that are still missing are pursued in this thesis.

Chuck and Sparrow (1987) and Chuck (1985) performed an experiment where a rectangular pan of water was set into the bottom panel of a duct and turbulent air was passed through the duct and over the surface of the water. The thermal conditions of the air and water and the evaporation rate were measured. The height of water in the pan was varied and two pan lengths of 12.5 and 27.9 cm were used. The convective mass transfer coefficient was determined and a correlation was developed for the Sherwood number $\left(\mathrm{Sh}_D = \frac{KD}{\mathcal{D}}\right)$, which served as an extrapolation formula for larger lengths of pans where L/D ≥ 23.8 and L/h ≥ 18 (L is the streamwise length of pan, D is the hydraulic diameter of the flow cross-section of the mass transfer section $\left(D = \frac{4(WH + wh)}{2(W + H + h)}\right)$ and h is the distance between the water surface and the top of the pan) (Chuck and Sparrow, 1987).

Prata and Sparrow (1986) performed a similar experiment to Chuck and Sparrow (1987), using a cylindrical container. The water level in the container was varied, and the resultant effect was measured and reported in the form of a Sherwood number

$\left(\mathrm{Sh}=\frac{\mathrm{KD}}{\mathcal{D}}\right)$ for Reynolds numbers $\left(\mathrm{Re}=\frac{\rho\bar{u}\mathrm{D}}{\mu}\right)$ between 7,300 and 48,600. It was found that the maximum Sherwood number occurred when the ratio of the step height of water from the top of the container to the diameter of the container was 0.5. The correlations of Chuck and Sparrow (1987), Chuck (1985) and Prata and Sparrow (1986) accurately quantify mass transfer for the turbulent flow regime, but many applications in building science and environmental engineering have lower air velocities and therefore require mass transfer coefficients for laminar or natural convection airflow.

Pauken (1999) performed experiments by evaporating heated water from a circular pan in a low speed wind tunnel. The evaporation boundary layer that resulted was a combined turbulent forced and turbulent free convection boundary layer, where the forced convection was dominated by the air velocity and the free convection was a result of the density difference between the air at the surface of the water and the ambient air. It was found that 30% of the evaporation rate was due to free convection when the ratio of the mass transfer Grashof number $\left(\mathrm{Gr_m}=\frac{\rho\left(\rho_a-\rho_i\right)\mathrm{gL}^3}{\mu^2}\right)$ over the Reynolds number $\left(\mathrm{Re}=\frac{\rho\mathrm{Vd}}{\mu}\right)$ squared ($\mathrm{Gr/Re^2}$) was 0.1. This study and others (Sparrow et al., 1983; Huang et al., 2005; Jang et al., 2005) demonstrate that natural convection is present in the evaporation boundary layer when the air speeds are low. These effects cannot be neglected in many building science and environmental problems such as moisture transfer between indoor air and porous building materials.

To further investigate the onset of convective instability for laminar forced convection in the entrance region of horizontal ducts, a numerical study was performed by Lin et al. (1992). The entrance region is the location where the air enters the duct to the point where the developing boundary layers become fully-developed. The top and two sidewalls of the duct were adiabatic, while the bottom wall had a thin heated water film with a constant wall temperature and concentration. The temperature and concentration boundary layers were developing throughout the length of the duct, with a fully developed, parabolic velocity profile set at the entrance of the duct. The effect of free convection on the local Sherwood number $\left(Sh_z = \frac{h_m D_e}{D} \right)$ was a result of combined thermal and mass diffusion effects and was quantified with an effective Rayleigh number $\left(Ra^+ = PrGr_t + ScGr_m \right)$. Results showed that an increase in Ra^+ resulted in an increase in Sh_z. Free convection effects on Sh_z were found to be insignificant when $Ra^+ < 1910$ and $Ra^+ < 1750$ for aspect ratios ($\gamma = \frac{a}{b}$) of 2 and 10 respectively.

Yan (1996) performed a numerical study of laminar mixed convection heat and mass transfer in horizontal rectangular ducts. The four duct walls were kept at a uniform temperature and concentration. A fully-developed, parabolic velocity profile was imposed at the entrance of the duct with constant temperature and concentration. The effects of the buoyancy ratio $\left(N = \frac{\beta^*(c_w - c_o)}{\beta(T_w - T_o)} \right)$ on the Sherwood numbers $\left(Sh = \frac{\bar{h}_m D_e}{D} \right)$ and Nusselt numbers $\left(Nu = \frac{\bar{h} D_e}{k} \right)$ were examined. The buoyancy ratio

represented the relative effects of species diffusion to thermal diffusion and was proportional to the ratio of concentration difference to the temperature difference between the duct walls and the air flowing through the duct. When N = 0, there was no mass diffusion, and the buoyancy force was a result of the temperature difference between the air flowing through the duct and duct walls. It was determined that when N > 0, buoyancy forces from mass and thermal diffusion are combined to assist the flow, and when N < 0, they oppose each other. Compared to the case when N = 0, the Sherwood and Nusselt numbers were always greater when N > 0 and smaller when N < 0.

Lyczkowski et al. (1981) performed a numerical analysis for fully developed laminar forced convection heat transfer in rectangular ducts. The problem was solved for the cases where there was insulation on no walls, one wall, two walls, and three walls with various finite resistances on the remaining walls. The local heat transfer coefficient was determined in the thermal entrance and fully developed regions for constant flux and constant temperature boundary conditions. For the case of one wall at constant temperature and $\gamma = \frac{b}{a} = 10$, the fully developed Nusselt number $\left(\mathrm{Nu_y} = \frac{\mathrm{h_y a}}{\mathrm{k_g}} \right)$ was within 4% of that in Shah and London (1978).

The above literature review suggests that convective mass transfer coefficients have been experimentally measured and correlated for turbulent flow through ducts, but not for laminar flow through ducts. In addition, the dependence of the convective mass transfer coefficient on Rayleigh number when the temperature of the bottom surface of

the duct is below that of the airflow has not been reported. Since little information is available at low air speeds, experiments in this thesis are predominantly conducted throughout the laminar flow regime. Laminar flow results are compared to the work of Lin et al. (1992), to gain an understanding of the effect of bottom wall temperature on the convective mass transfer coefficient. The heat transfer results of Lyczkowski et al. (1981) and the analogy between heat and mass transfer are used to further verify the experimental results. Turbulent flow is also investigated up to a Re_D (defined in Section 3.3.1) of 8,100, so a direct comparison to the work of Chuck (1985) can be made. In the experiments, the temperature and the relative humidity of the air are varied so the effect of Ra_D (defined in Section 3.3.2) due to the temperature and vapor density differences between the surface of the water and the air stream on the convective mass transfer coefficient can be quantified. Besides this thesis, the results from the experiments have been published by Iskra and Simonson (2006) in the International Journal of Heat and Mass Transfer.

1.3 Convective Mass Transfer with a Permeable Membrane

The purpose of studying a permeable membrane is to gain an understanding of the heat and mass transfer properties of the material for use in an enthalpy exchanger. An enthalpy exchanger is a device that is able to exchange sensible heat as well as latent heat between two fluids, such as air-air or air-water. The enthalpy exchanger of interest is a panel type enthalpy exchanger (shown in Figure 1.1) where the permeable membrane acts as the medium of the exchanger that separates a conditioning fluid (water or an aqueous solution) and air within a building space. Figure 1.1 shows a schematic of a rectangular enthalpy exchanger that has a permeable membrane attached to its

underside. A conditioning fluid is circulated through the exchanger where it either gains/releases heat and water vapor from/to air.

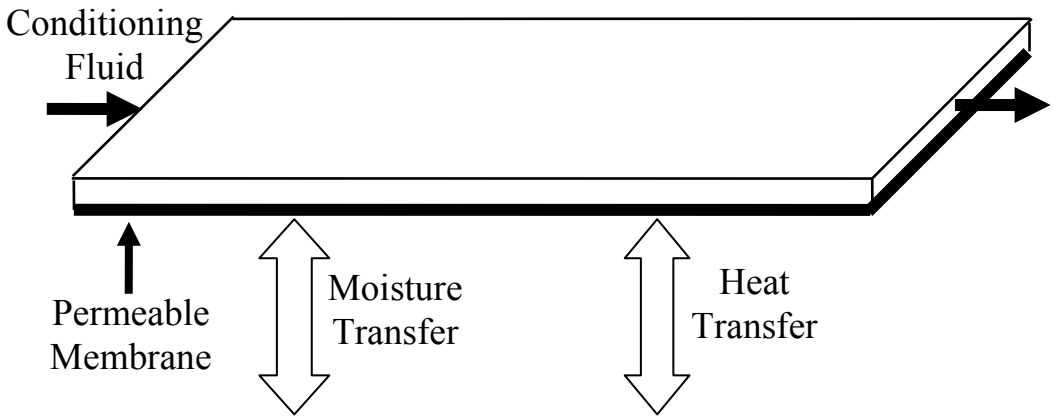

Figure 1.1 Schematic of a radiative type enthalpy exchanger where a vapor permeable membrane forms the base of the exchanger. Heat and moisture are transferred between air and a conditioning fluid that are separated by the membrane.

The enthalpy exchanger is intended to replace a traditional radiant heating/cooling panel, which provides sensible heat transfer only. The enthalpy exchanger could be used in commercial or residential buildings to condition an air space to comfortable temperature and relative humidity conditions. A panel type enthalpy exchanger may be a viable product since other membrane-based systems typically have long life spans as well as low energy consumption (Sander and Janssen, 1991).

Traditional radiant heating and cooling panels can be used in most commercial buildings provided there are no excessive internal heat gains. Because of the limited cooling output of the radiant panels, a radiant cooling system would not be able to maintain comfort conditions in buildings with high lighting loads (jewelry stores) or process loads (industrial facilities) (Advanced Buildings, 2006). Conversely, radiant systems are the ideal choice in buildings where air quality is critical (hospitals and operating rooms).

With radiant systems, only the ventilation air has to be filtered and delivered to space, which reduces ducting space and cost as well as fan energy compared to all air systems.

A traditional radiant heating and cooling panel system heats and cools a building by convective and radiation heat transfer. Typically, heated or chilled water is circulated through floor or ceiling panels to provide sensible heat exchange with the space. To provide latent heat exchange within a space, a hybrid (load-sharing) HVAC system is used where additional HVAC components are used to condition the ventilation air. The panels cover a large area of floor or ceiling and operate at temperatures close to room air temperature, approximately 15^{o}C in cooling mode and 35 to 50^{o}C in heating mode. The amount of heat transfer depends on the direction of heat flow. Air in contact with a cooled ceiling panel will naturally fall as it is cooled, increasing the movement of air over the panel. Conversely, air in contact with a warm ceiling will stratify at the ceiling resulting in lower convective heat transfer.

ASHRAE, 2004 provides a list of advantages that a traditional heating and cooling panel has over other heating and cooling systems. ASHRAE, 2004 states that comfort levels within a space can be better than those of other space-conditioning systems, since thermal loads can be directly satisfied within the space. ASHRAE, 2004 also states that a heating and cooling panel system can achieve draft-free environments since space air requirements usually do not exceed those required for ventilation and humidity control. The physical construction of a heating and cooling panel can also provide the advantage of reducing peak loads within a space due to the thermal energy storage within the panel's structure.

ASHRAE, 2004 also provides a list of disadvantages that a traditional heating and cooling panel has over other heating and cooling systems. ASHRAE, 2004 states that a heating and cooling panel can only satisfy sensible heating and cooling loads. If there are latent loads that need to be satisfied within a space, supplemental equipment would be needed. ASHRAE, 2004 also states that if latent loads are high, dehumidification and panel surface condensation may be a concern. In cooling mode, the temperature of the air at the surface of the panel may be reduced to the point where condensation becomes a problem.

An advantage of using an enthalpy exchanger in place of a traditional radiant heating and cooling panel would be to simultaneously transfer sensible energy as well as latent energy (moisture) within a space. Latent heat exchange would reduce the need for the ventilation air to add or remove moisture from the space. The enthalpy exchanger could meet both the sensible and latent loads of the space. Another advantage of using an enthalpy exchanger is to reduce the onset of condensation that occurs on a traditional cooling panel surface when the operating temperature of the exchanger is below that of the dew point temperature of the air within a space. With the use of a water vapor permeable membrane, the enthalpy exchanger may be able to reduce the relative humidity at the surface of the exchanger, by transferring water vapor from the membrane's surface to the conditioning fluid. If this is feasible, the enthalpy exchanger could be operated at lower temperatures than traditional cooling panels before the onset of condensation occurs at the surface of the exchanger, which could increase the cooling capacity of the exchanger.

In this thesis, a numerical model is developed, which is intended to simulate heat and water vapor transfer through a water vapor permeable membrane. Experiments are performed where the membrane is placed in between the airflow and the pan of water within the test section of the TMT facility. The membrane acts as an extra resistance to heat and moisture transfer between the airflow and the surface of the water. The model is used to determine the transient response of the material to heat and moisture transfer, as well as verify the steady-state experimental moisture transfer rates.

1.3.1 Literature Review

The following literature review introduces general experimental and numerical work on porous membranes, to give an idea of the type of work that has been performed to date.

Porous membranes have a low resistance to heat and moisture transfer since they are very thin and have a highly porous structure. The structure and the hydrophobic nature of these membranes allow transport of water vapor but prevent liquid water from entering into the membrane. These inherent characteristics of the membrane make it an ideal material as the transfer medium for an enthalpy exchanger that requires high heat and water vapor transfer rates.

The porous membrane that is being studied in this thesis is Tyvek®. Tyvek® is a spunbonded olefin composing of high density polyethylene fibers. The fibers are spun and then bonded together by heat and pressure to create a strong, lightweight and flexible sheet product of approximately 150 μm in thickness. Tyvek® is a common material that is used in many practical applications. Tyvek® is used on houses to prevent

airflow through walls, hold out bulk water and wind-driven rain as well as let water vapor to escape from within the building structure. It is used in protective garments to protect people from dirty environments and chemical spills. It is also used in envelopes that are tear, puncture and water resistant.

Recent work in this area of study has been performed by Fan (2005) and Zhang and Niu (2002) where membrane cores have been used in cross-flow enthalpy exchangers to transfer heat and moisture between the supply and exhaust air streams in buildings. Fan (2005) modeled a run-around heat and moisture recovery system that was comprised of two cross-flow semi-permeable plate exchangers that were coupled by an aqueous desiccant salt solution. A control volume method was used to develop the governing equations for the heat and moisture exchange. The numerical model was used to investigate the performance of such an exchanger, and it was found that an overall sensible, latent and total effectiveness of 70% was possible for a well designed practical system. It was determined that air-to-air enthalpy recovery with membrane exchangers has a large potential in energy efficient buildings (Zhang and Niu, 2002).

Zhang and Jiang (1999) developed a heat and mass transfer model for an energy recovery ventilator with a porous hydrophilic membrane core. The air-to-air heat exchanger incorporated alternating membrane layers to transfer heat and moisture from one air stream to the other. A finite-difference simulation was implemented that calculated the temperature and humidity fields in the exchanger. It was found that the effectiveness of sensible, moisture, and enthalpy transfer was higher when the exchanger was operated in a counter-flow arrangement as opposed to a cross-flow arrangement.

Findley et al. (1969) performed an experimental analysis that studied the rates of mass transfer of water vapor from a heated salt solution through a water repellent porous membrane to a cooled water condensate. The apparatus consisted of two chambers that were sealed by two rubber gaskets with a 110 cm^2 membrane placed between them. One side of the chamber was filled with 7% by weight sodium chloride and the other with distilled water. The experiment studied the relationship between the rate of evaporation and the vapor pressure difference, membrane thickness, and heat conduction through the membrane. They found that the major factor influencing the moisture transfer rate was the diffusion through the stagnant gas in the membrane pores. However, the film heat transfer coefficients, membrane thermal conductivity, and the temperature driving force had an effect on the rate of water vapor transfer as well.

Zhang et al. (2003) experimentally determined the permeability of six polytetrafluoroethylene membranes to five different gases, He, N_2, O_2, CO_2 and water vapor. A mathematical model was developed that considered Knudsen and molecular diffusion, as well as Poiseuille flow. Knudsen diffusion occurs when the mean free path is relatively long compared to the pore size, where molecular diffusion occurs when the mean free path is relatively short compared to the pore size. The predicted permeability values were in good agreement with the experimental data. Results showed that the gas permeability was influenced by the mean pore size and distribution, as well as thickness and tortuosity. It was also found that the mass transfer rate of water vapor increased as the temperature increased.

Fohr et al. (2002) used a one-dimensional dynamic model to study heat and water transfer through layered fabrics in clothing. A porous media model was implemented, which averaged the microscopic volumes within the material to formulate a macroscopic representation of the material. Within the averaged volume, local thermodynamic equilibrium between the solid, liquid and gas phases was assumed. The model was used to simulate basic experiments performed by Li and Holcombe (1992), Wehner et al. (1988) and Yasuda et al. (1992, 1994). It was found that the simulations compared well with experimental data.

A literature review has shown that to date there is little information in the literature on radiative type enthalpy exchangers that utilize a water vapor permeable membrane to exchange sensible as well as latent energy. As well, little numerical work has been performed that determines the transient response of a membrane when it is subjected to convective boundary conditions. Also, there is little information in the literature that compares numerical and experimental work where a membrane is subjected to the type of convective boundary conditions that are present in the TMT facility.

1.4 Research Objectives

The purpose of this study is to measure the convective mass transfer coefficient for the test section of the transient moisture transfer (TMT) facility and use these results to numerically and experimentally study heat and moisture transfer through a vapor permeable membrane.

The objectives of this research are listed below:

1. Experimentally measure the convective mass transfer coefficients for laminar and turbulent flow for a horizontal rectangular duct.
2. Compare results from objective 1 with experimental and numerical investigations provided in the literature.
3. Develop an analogy between heat and mass transfer to determine the convective heat transfer coefficient from the convective mass transfer results.
4. Develop a new method that is able to convert a pure heat transfer Nu_D and a pure mass transfer Sh_D into a Nu_D and Sh_D for simultaneous heat and mass transfer.
4. Experimentally measure the water vapor transfer rates across a Tyvek® membrane within the test section of the TMT facility.
5. With the results from objectives 1 and 3, develop a numerical model to simulate the experiments of objective 4, and determine the transient temperature and vapor density profiles within the membrane as a function of time.

1.5 Thesis Overview

Explanations of the experimental apparatus including the calibration of the instrumentation for the convective mass transfer experiments are covered in Chapter 2. Chapter 3 presents experimental data that are used to determine the precision uncertainty as well as the heat and mass balances of the experimental data. The results from the convective mass transfer experiments are given in Chapter 4 with comparisons to similar experimental and numerical data from the literature. Chapter 5 presents experimental and numerical results for mass convection with a permeable membrane. The findings from this research are summarized and future work is given in Chapter 6.

CHAPTER 2

EXPERIMENTAL FACILITY AND INSTRUMENTATION

2.1 Introduction

The purpose of the experiments are to measure the convective mass transfer coefficient for airflow in the rectangular test section of the transient moisture transfer (TMT) facility. The measurements determine the surface resistance to mass transfer of the test section for different Reynolds numbers and air relative humidities. The experimental results are used in Chapter 5 within a numerical model that is used to model heat and moisture transfer through a porous membrane. This chapter focuses on the experimental procedure, the apparatus, the instruments used and their calibrations, as well as the uncertainties in the measurements for the convective mass transfer experiments.

2.2 Apparatus and Procedure

The TMT facility is an experimental apparatus that determines the transient heat and moisture transport properties of porous materials. Olutimayin (2004) and Osanyintola (2005) measured transient vapor boundary layer growth in cellulose insulation and spruce plywood with the TMT facility. The test section within the TMT is a horizontal rectangular duct, where heat and mass transfer occur between flowing air and a stationary porous material at the bottom surface of the duct. In the facility, air at varying velocities, temperatures and relative humidities passes above the porous building material and the change in mass, relative humidity, and temperature in the material are

measured as a function of time. To fully document experimental results for the TMT, the convective mass transfer coefficient of this facility is required.

Mass transfer coefficients have been determined by using Naphthalene sublimation where complex flows and geometries are present (Goldstein and Cho, 1995). Since the geometry of the TMT facility test section (rectangular duct) and the airflow through it (purely axial) are simple in nature, a more convenient technique is used instead of using Naphthalene sublimation. Mass transfer coefficients can also be determined from experiments based on the adiabatic evaporation of a liquid (Kondjoyan and Daudin, 1993) where the mass transfer surface is flat, and this method is applied in this research. Since water vapor transfer is the only form of mass transfer in the TMT facility when experimenting on porous building materials, distilled water is used as the evaporating liquid to ensure that the same Schmidt number (Sc) is present in both experiments. The Schmidt number is a dimensionless number that is a measure of the relative effectiveness of momentum and mass transport by diffusion in the velocity and concentration boundary layers, respectively (Incropera and DeWitt, 2002). The convective mass transfer coefficient is determined for the horizontal rectangular duct by measuring: (1) the evaporation rate from a rectangular tray of water that is located in the lower panel of the duct and (2) the vapor density difference between the air stream and the surface of the water. The vapor density of the air stream is determined from the measured temperature and relative humidity of the air stream and the vapor density at the surface of the water is determined from the measured temperature of the water and the assumption that the air is saturated at the surface of the water.

2.2.1 Network of the Apparatus

A side-view and an expanded top-view schematic of the ducting upstream and downstream of the rectangular test section are shown in Figure 2.1 and Figure 2.2, respectively. All of the rectangular ducting shown has a width (W) of 298 mm. A variable speed vacuum pump supplies a hydrodynamically developed airflow at the entrance of the test section as shown in Figure 2.1 by means of a developing section upstream of the test section (Figure 2.3).

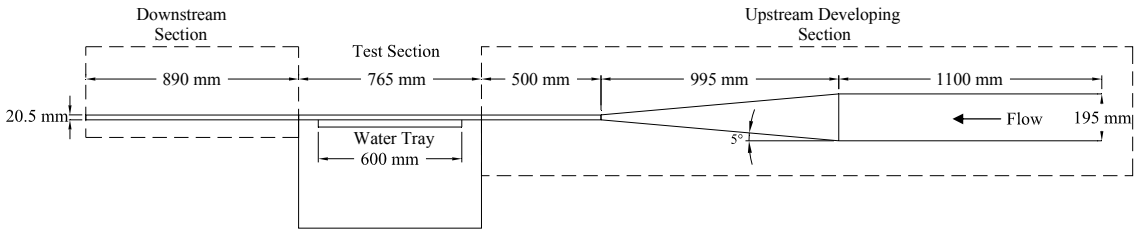

Figure 2.1 Schematic of the test facility showing a side view of the ducting network.

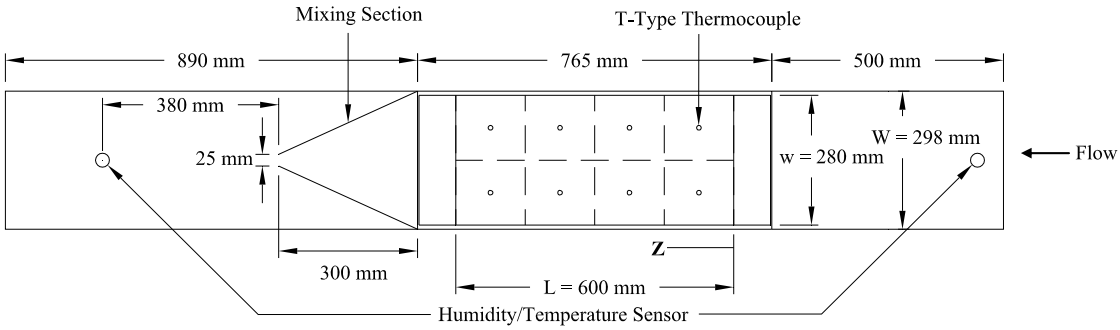

Figure 2.2 Schematic of the test facility showing a top view of the test section and the ducting connected to it.

First, the air flows through a 1100-mm-long duct that has a constant cross sectional area, which has several screens installed inside of it to aid in the straightening of the airflow. The air then passes through a 995-mm-long converging section that has a convergence angle of 5° to minimize the dynamic losses in the duct and aid in the development of the

flow. The ducts are constructed of ¼-inch (6.35-mm) steel plate, which are insulated on the outside with 2-inch (50.8 mm) polystyrene insulation to minimize heat transfer with the surrounding room. Following the converging section, the air enters a 500-mm-long (13.0 D_h, where D_h is the hydraulic diameter of the test section) straight duct that delivers the air to the test section. The duct of this section is constructed out of 2-inch (50.8 mm) polystyrene insulation with a top cover that is removable. The air then passes through the 765-mm-long (19.9 D_h) test section (close-up view shown in Figure 2.3) and then through a 890-mm-long (23.2 D_h) downstream section. The downstream section is composed of a 390-mm-long polystyrene duct with a removable top, and is connected to a 500-mm-long steel duct that is insulated the same as the other steel ducts. The removable top of the upstream and downstream ducts aids in the installation of the humidity/temperature sensors, and the removable top of the test section allows for the placement of the pan within the bottom surface of the duct. The ducts immediately upstream and downstream of the test section have the same hydraulic diameter as the test section when the evaporation pan is full of water (i.e., h = 0 mm in Figure 2.4).

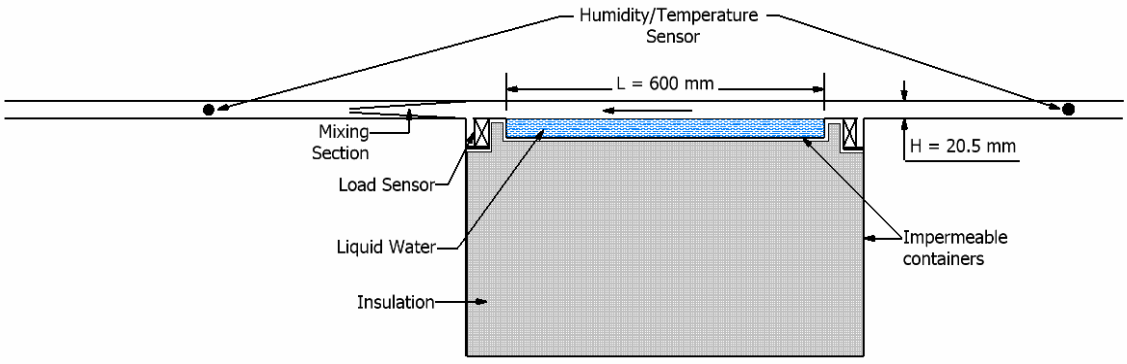

Figure 2.3 Schematic of the test facility showing a close-up view of the test section.

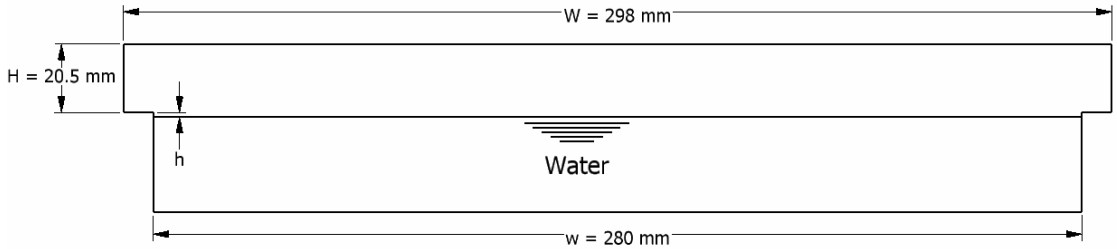

Figure 2.4 A cross-sectional view of the test section. In this view, airflow is into the page.

The test section and the ducting connected to it are insulated to minimize any heat transfer with the ambient environment. The top cover above the water pan, which creates the top surface of the test section, is constructed from 2-inch (50.8 mm) polystyrene foam insulation. It is sealed with aluminum foil tape along its edges to ensure there is no leakage of ambient air into or out of the test section during testing. The top cover is also lined on the inside with aluminum foil tape to prevent absorption of water vapor, and to reduce any radiative heat transfer between the top cover and the surface of the water. All the ductwork between the upstream and downstream humidity sensors are lined on the inside with foil tape to create a smooth surface and to prevent the absorption of water vapor. Therefore any change in humidity and temperature between the upstream and downstream sensors will be due to moisture and heat transfer between the free water surface and the air stream.

2.2.2 Test Section

The top view and cross-sectional view of the test section within the TMT facility are shown in Figure 2.2 and Figure 2.4, respectively. A tray with a water surface width (w) of 280 mm and a length (L) of 600 mm forms the lower panel of the duct (height (H) = 20.5 mm) in the test section. The sidewalls of the pan create a shelf within the test

section which causes the airflow width to be greater (18 mm) than the width of the water.

The air is delivered to the test section from an environmental chamber that controls the temperature and relative humidity of the air upstream of the test section within ±0.1°C and ±2% RH, respectively. The temperature and relative humidity of the air are measured upstream and downstream of the test section with Vaisala HMP233 humidity and temperature transmitters. Since the air is mixed within the environmental chamber and passes through over 2 m of impermeable and adiabatic ducting before it reaches the upstream sensor, the humidity and temperature profile at the upstream sensor (and entering the test section) can be assumed to be uniform. Therefore, the upstream sensor measures the bulk mean relative humidity and temperature of the air entering the test section.

On the other hand, the temperature and humidity profiles downstream of the test section will not be uniform since the evaporation process causes the air to have temperature and concentration gradients within the boundary layer. As a result, the air must be mixed before it reaches the downstream sensor to obtain the bulk mean properties of the air. Mixing is especially important when there are significant temperature and humidity differences between the air entering the test section and the air in contact with the surface of the water.

Mixing is accomplished with the use of a converging duct that is located within the downstream section (Figure 2.2). The air is mixed by converging the air from the

original duct width of 298 mm and height of 20.5 mm into a width of approximately 25 mm and height of 15 mm, which is a 16 times reduction in flow area. The reduction in flow area increases the Reynolds number of the airflow at the exit of the mixing section, which is eight times larger than the Reynolds number within the test section. Over the range of Reynolds numbers tested in this thesis, the increase in Reynolds number at the exit of the mixing section result in turbulent flow, which enhances mixing. Mixing is also enhanced with wire screen that covers the inside surface of the converging duct, which promotes tripping of the airflow.

2.2.3 Bottom Surface of the Test Section

A pan is situated in the bottom of the test section and forms the bottom panel of the rectangular duct when it is full of water. The pan is constructed of Lexan® polycarbonate which is chemically resistant to many fluids, including water. The pan rests on top of four load sensors that are located at each corner of the pan. The load sensors determine the mass of water that evaporates during an experimental. The temperature of the surface of the water is needed to determine the average saturated vapor density above the surface of the water (ASHRAE, 2005). The temperature of the water is measured with 8 T-Type thermocouples, which enter the test section through a sealed hole that is located in the side of the test section. The pan is divided into 8 imaginary, equally sized square sections and each thermocouple is placed into the center of each section (Figure 2.2). The thermocouple leads are secured to the bottom of the pan with aluminum foil tape and the thermocouple ends are positioned approximately 2 mm below the surface of the water.

2.2.4 Data Acquisition

The data acquisition consists of a personal computer that uses National Instruments (NI) LabView® 7.1 (a graphical development software package), which records the experimental data. Figure 2.5 shows LabView's user interface, which displays the data being recorded by the data acquisition system. The T-Type thermocouples and the load cells are connected into a NI SCXI 1000 chassis, which is connected to a 16-bit (NI PCI 6052E) data acquisition card. The relative humidity and pressure readings are fed into a (NI-CB-68LPR) connector block, which is connected to 12-bit (NI PCI 6024E) data acquisition card. Measurements of all temperature, relative humidity and pressure readings are recorded every 5 minutes and the mass change of water in the pan is recorded every 20 minutes. All measurement data are an average of 100 measurements taken over 0.1 s intervals at the measured time.

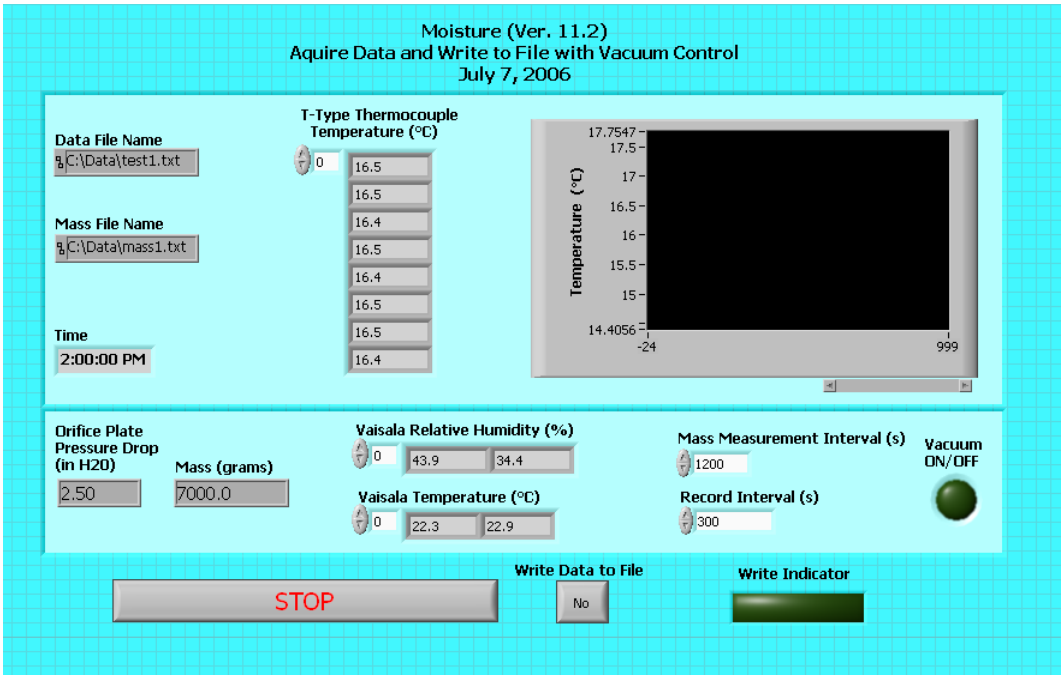

Figure 2.5 LabView 7.1 graphical user interface.

2.2.5 Hydrodynamically Fully Developed Flow

The velocity profile of the air entering the test section is an important parameter to consider, as this flow condition will influence the convective mass transfer coefficient. When the airflow enters the upstream development section of the TMT facility (Figure 2.1) from the environmental chamber, the velocity profile of the airflow begins to develop along the length of this section. Only when the velocity profile forms a parabolic profile for laminar flow is it considered to be fully developed. Fully developed flow is important to achieve before the airflow enters the test section for a few reasons.

They are:

1. To simulate the conditions of the convective mass transfer experiment in laminar flows, fully developed flow allows researchers to apply a simple parabolic velocity profile within their numerical models over a range of laminar flows.

2. The results in this thesis can be compared to past numerical and experimental research is for fully developed flow.
3. The effects of a developing concentration and thermal boundary layer can be determined if the hydrodynamic boundary layer is already developed.

The straightening screens, the small convergence angle (5°) and the 13.0-D_h duct immediately upstream of the test section ensure that the flow is hydrodynamically fully developed for turbulent flow in the duct (Tao et al., 1993), but the hydrodynamic conditions must be determined experimentally for laminar flow. In this thesis experiments are performed to determine if the airflow is hydrodynamically fully developed for laminar flow, and also for turbulent flow. To determine if the airflow is hydrodynamically fully developed before it enters the test section, the velocity profile along the height of the duct and the static pressure along the length of the duct immediately upstream of the test section are measured. Both methods require pressure measurements, which are measured with a pressure transducer. The transducer has a full-scale reading of 0.20 inH_2O (50 Pa), which corresponds to a 5 volt output. A Pitot-static probe with a tube diameter of 3.06 mm is used to determine the velocity profile within the duct.

Transverse pressure measurements are taken at increments of approximately 2 mm across the height of the duct with the Pitot-static probe. The average pressure reading at each position within the duct is determined by measuring the pressure reading every 6 seconds for 10 consecutive readings for the laminar flow, and every 3 seconds for 20

readings for the turbulent flow. The number of samples and the time increments were selected to minimize the precision uncertainty in the measurements.

The Pitot formula, given by White (1999), is used to calculate the air velocity at each location with the duct by using pressure readings measured with the Pitot-static probe. The average velocity within the duct for laminar (0.7 m/s) and turbulent (3.1 m/s) flow are small enough such that the airflow is not turbulent over the Pitiot-static probe diameter. Because of the low air velocity, an error in the pressure reading results, but this is corrected to increase the accuracy of the measurements. The pressure readings are corrected based on the measured air velocity using a correction equation provided by Chue (1975). The corrected velocities are up to 11% and 3% less than the measured velocities for a Re_u of 1700 and 7700, respectively. Another correction on the measured air velocity is performed that takes into account the displacement effect on the Pitot-tube measurements in shear flow (Raju et al., 1997). The measured velocity is corrected based on the equation given by Raju et al. (1997). The corrected air velocities are up to 27% and 24% less than the measured velocities for a Re_u of 1700 and 7700, respectively. Figure 2.6 contains transverse velocity measurements over the duct cross-section for laminar ($Re_u = 1{,}700$) and turbulent ($Re_u = 7{,}700$) flow at $x/l = 0.82$, where l is the distance between the first and last static pressure tap (Figure 2.7).

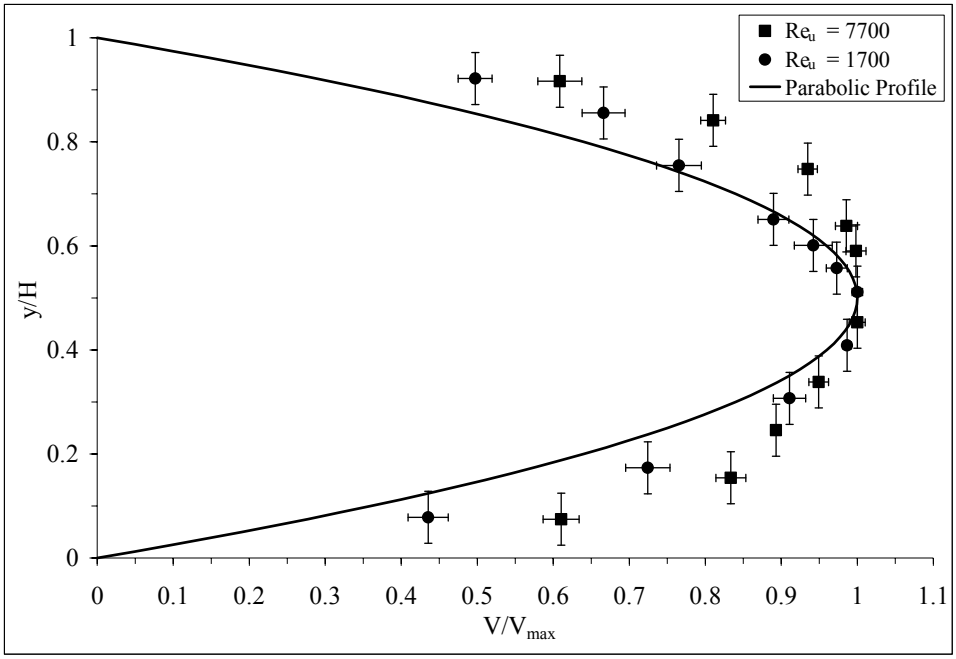

Figure 2.6 Measurements of the laminar and turbulent velocity profile at x/l = 0.82. The 95% uncertainties in the velocity ratio are given as error bars.

The measurements are quite uncertain because of the small dynamic pressures (0.2 to 0.6 Pa for laminar flow and 4.2 to 7.1 Pa for turbulent flow) and the difficulty in determining the exact location of the Pitot-static probe. The 95% confidence limits, based on the standard deviation of the mean of V/V_{max} are shown in Figure 2.6 with uncertainty bars. The uncertainty of the location of the tip of the Pitot-static probe within the duct is estimated to be ±1 mm, which gives an uncertainty in y/H of ±0.05 (shown in Figure 2.6 with uncertainty bars). The uncertainty in V/V_{max} increases as the Pitot-static probe approaches the duct wall, where the maximum uncertainty is ±4%. The velocity profile for laminar flow forms a velocity profile that is similar to (but broader than) the ideal parabolic Poiseuille velocity profile, which is characteristic of fully developed laminar flow. For turbulent flow, the velocity profile has a broader profile than the laminar case, which is characteristic of turbulent flow.

To measure the static pressure profile upstream of the test section, ¼ inch (6.35 mm) polyethylene tubing is used as the static pressure tap (inside diameter of 4.2 mm). The pressure taps are installed along the center width of the duct immediately upstream of the test section at intervals of 4 cm (Figure 2.7), and the pressure difference between each tap and the tap furthest from the test section (x = 0) is measured.

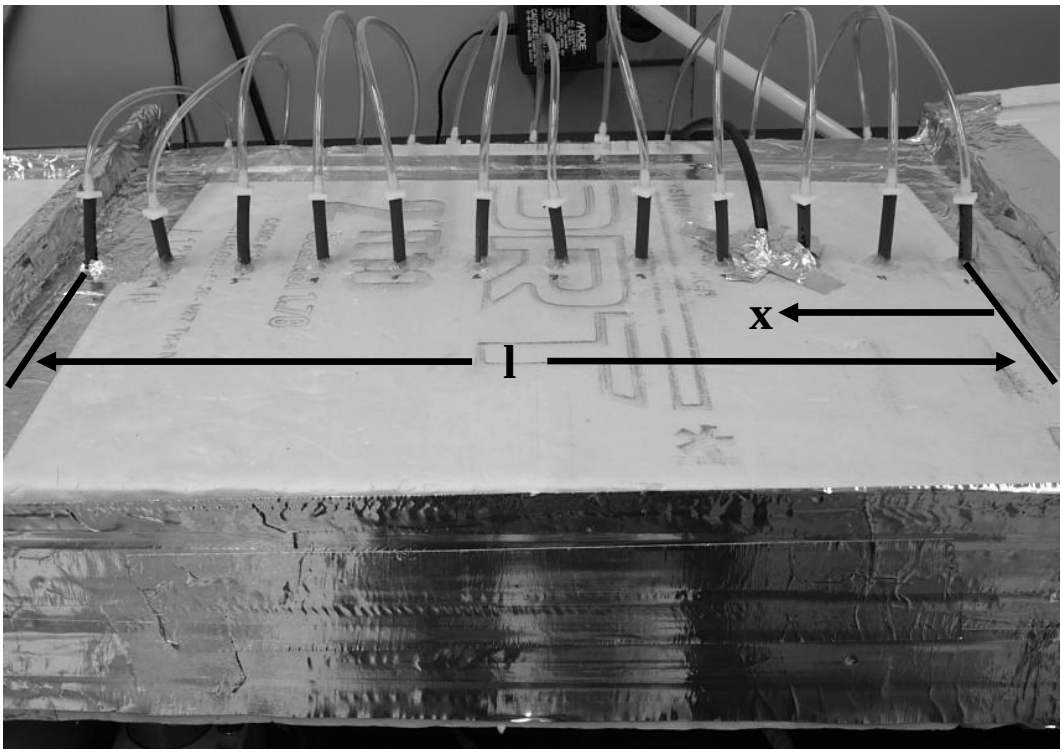

Figure 2.7 Static pressure taps installed along the center width of the duct immediately upstream of the test section. Pressure taps are spaced 4 cm from eachother. The pressure drop is measured with respect to the pressure tap at x = 0.

Figure 2.8 shows the pressure data for a Re_u of 2,000 and 4,000. The precision uncertainties in the measured static pressure drops are approximately the size of the data points in Figure 2.8. The static pressure drop varies nearly linearly with distance along the duct. The only exception is for 4 cm on either side of the mid point of the duct where the pressure levels. This leveling in pressure is likely due to a slight expansion of the duct near the mid point. The static regain due to even a 1 mm (5%) expansion over a 12

cm region at the mid point of the duct would overcome the friction pressure drop and result in a constant static pressure. The leveling of pressure from $0.4 \leq x/l \leq 0.65$ may explain why the velocity profile (measured at $x/l = 0.82$ and presented in Figure 2.6) is slightly different than the expected parabolic profile for fully developed laminar flow in a rectangular duct.

After the leveling region, the pressure recovers since the pressure drop is slightly larger than the pressure drop before the leveling region. The pressure does not fully recover, however, which indicates that the duct may be slightly larger near the exit. Despite the leveling of the pressure at the midpoint of the duct, the pressure drop becomes linear with distance before the air enters the test section ($x/l = 1$). Since the velocity profile is nearly parabolic (Figure 2.6) and the pressure gradient is linear at the entrance of the test section (Figure 2.8), it is concluded that the airflow entering the test section is hydrodynamically fully developed.

If the velocity profile is not hydrodynamically fully developed, the Sh_D determined in this thesis will be larger than that for a hydrodynamically developed airflow, due to larger velocity gradients at the surface of the water. It will be shown in Chapter 4 that the Sh_D determined in this thesis are consistently less than the Sh_D found in the literature (for hydrodynamically developed airflows), which suggests that the airflow in this thesis is hydrodynamically full-developed. The reasons for a lower Sh_D will be discussed in Chapter 4.

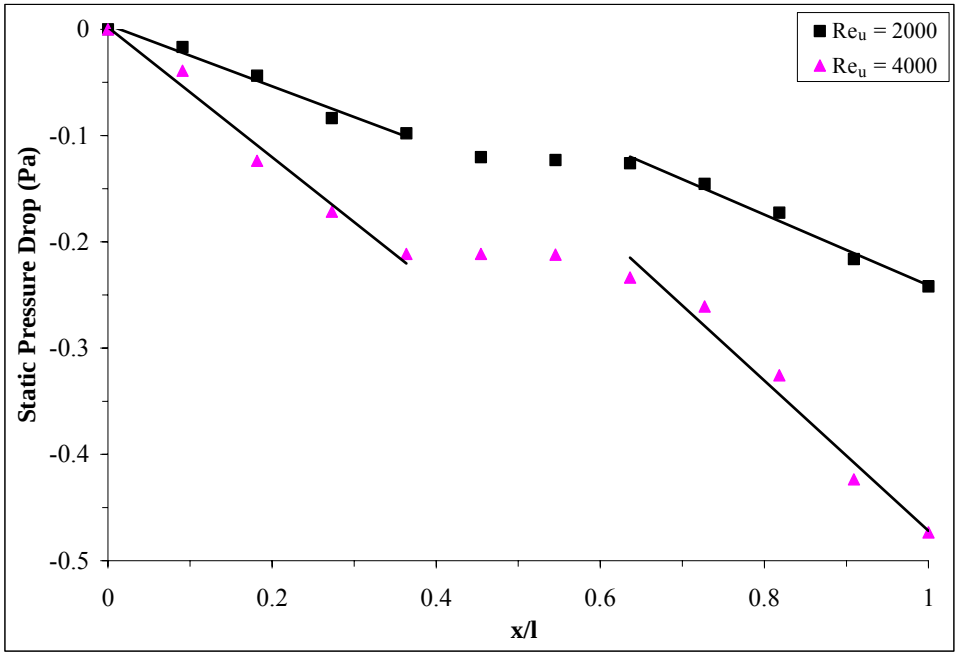

Figure 2.8 Measurements of the static pressure drop along the length of the duct just upstream of the test section (x/l = 1 corresponds to the point where the upstream duct joins the test section).

2.3 Measurements and Calibration of Instruments

The following section introduces the different instrumentation used to measure the convective mass transfer coefficient for the rectangular duct within the TMT facility. Each instrument is calibrated, and the bias uncertainty is determined.

2.3.1 Temperature Sensors

The vapor density of the airflow in the test section is required in order to determine the concentration difference between the airflow and the air at the surface of the water. To determine this vapor density, Vaisala HMP233 temperature and humidity transmitters are used to measure the bulk temperature and relative humidity of the airflow upstream and downstream of the test section (Figure 2.2 and Figure 2.3). Psychrometric equations are used to calculate the average vapor density of the airflow from the measured temperature and relative humidity.

The temperature sensors within the transmitters are Platinum 100 RTD type and are internally calibrated against a dry-well temperature generator that has a bias uncertainty of ±0.1°C. A two-point calibration technique is used, which calibrates the sensors at 10°C and 60°C. Post-calibration temperature measurements are taken between 20°C and 40°C against the temperature generator to determine the bias uncertainty of the temperature sensors. Figure 2.9 shows the range of temperatures that are measured, and the temperature difference between the thermocouple reading and the temperature generator. The majority of the temperature readings are taken between 20°C and 25°C since the majority of experiments are performed over this range. The 95% bias uncertainty of the sensors with respect to the temperature generator are ±0.05°C and ±0.06°C for sensor number 21053 (upstream) and 21054 (downstream), respectively. After combining the bias uncertainty of the temperature generator with the sensor bias uncertainty, the total 95% bias uncertainty of the sensors are ±0.11°C and ±0.12°C for the Vaisala HMP233 21053 and 21054, respectively.

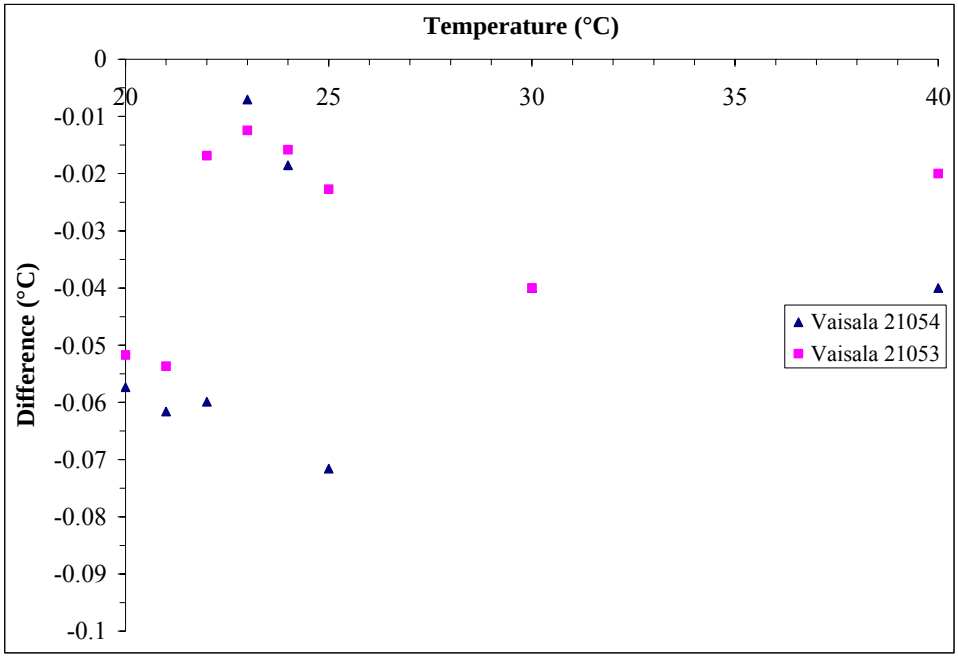

Figure 2.9 The temperature difference between the readings of the temperature sensors manufactured by Vaisala and the dry-block temperature calibrator at different temperatures.

The vapor density of the air at the surface of the water is determined by measuring the temperature of the surface of the water with eight T-Type thermocouples. By measuring this temperature and assuming that the water vapor at the surface of the water is saturated (Incropera and DeWitt, 2002), psychrometric equations are used to obtain the vapor density. The thermocouples are calibrated with the dry-well temperature generator for a temperature range between 12°C to 23°C. The thermocouples are numbered 0 through 7, and the temperature differences between the thermocouple reading and the generator are given in Figure 2.10. Since the thermocouples cannot be internally calibrated, a calibration curve is generated for each thermocouple from the data in Figure 2.10 to reduce the bias uncertainty between the thermocouple and the temperature generator. The 95% bias uncertainty of the thermocouples, based on the calibration curves, are between ±0.02°C and ±0.14°C, depending on the individual thermocouple.

After combining the bias uncertainty of the temperature generator and the bias uncertainty in the calibration curves, the total 95% bias uncertainty of the thermocouples range between ±0.10°C and ±0.17°C.

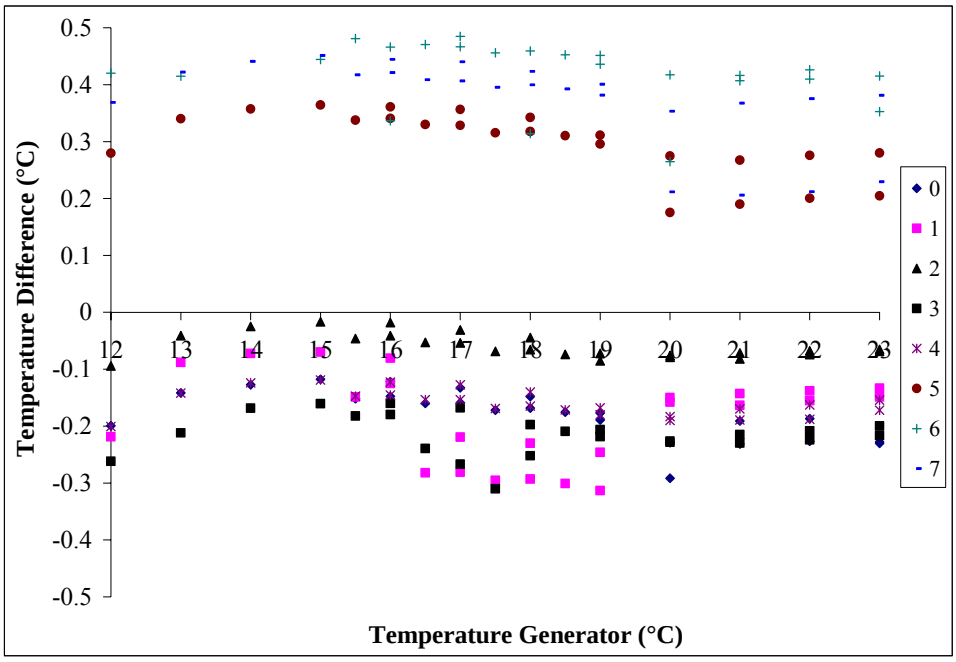

Figure 2.10 Temperature difference between the readings of the T-Type thermocouples and the dry-well temperature generator.

2.3.2 Relative Humidity Sensors

The relative humidity sensors of the Vaisala HMP233 temperature and humidity transmitters are HUMICAP® type capacitance sensor and are internally calibrated using a humidity generator and a General Eastern chilled mirror hygrometer as a transfer standard. The bias uncertainty of the chilled mirror is ±0.5% RH at 40% RH and ±1.25% at 95% RH. Two calibration attempts are performed to reduce the bias uncertainty in the relative humidity sensors. The first calibration attempt is a two point calibration at a relative humidity of 20% RH and 70% RH. A post-calibration check after this two point calibration shows that the sensor readings are not within the bias uncertainty of the

chilled mirror over the range that the sensors are used. To reduce the bias uncertainty, a second calibration of the sensors at the midpoint of the two-point calibration (45% RH) is done, and a post-calibration check over the sensor testing range shows that the sensors are within the bias uncertainty of the chilled mirror.

During the end of the experimental testing, it was found that a mass balance across the test section based on the humidity sensor readings for the convective mass transfer experiments did not compare within experimental uncertainty to the mass balance determined by the load sensors. To determine the cause of this, the relative humidity sensors were checked against the chilled mirror to determine if the relative humidity sensors calibration had changed over the testing time. Figure 2.11 shows the difference between the relative humidity measured by the sensors and the chilled mirror. It was found that the bias uncertainty increased over the testing time and was larger than the bias uncertainty of the chilled mirror. To account for this change in the sensors, a third order polynomial calibration curve was generated from Figure 2.11 to correct the experimental data, and reduce the bias uncertainty in the sensors. After correction, the 95% bias uncertainty of the sensors with respect to the chilled mirror are ±0.8% RH and ±0.3%RH for sensor 21054 and 21053 respectively. The total 95% bias uncertainty of the sensor (which takes into account the bias uncertainty in the chilled mirror), is ±0.9% RH and ±0.6% RH for sensors 21054 and 21053 respectively. The RH sensor readings were corrected based on the calibration equation, and the mass balance between the RH sensors and the load sensors were then found to be within the experimental uncertainty.

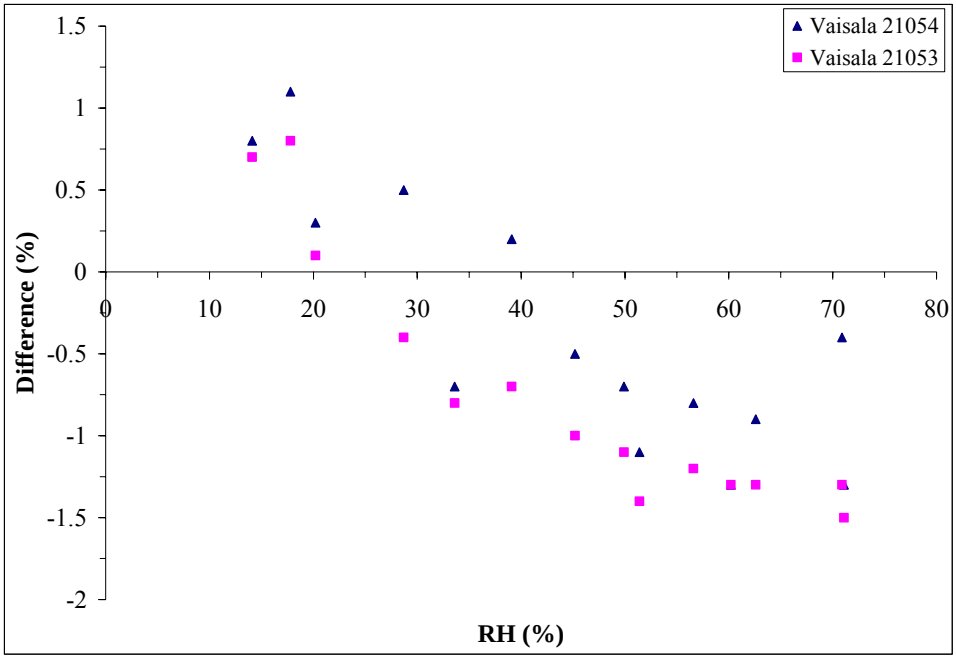

Figure 2.11 The difference between the readings of the humidity sensors manufactured by Vaisala and the chilled mirror. Measurements are taken after all the experimental tests are finished.

2.3.3 Gravimetric Load Sensors

Gravimetric load sensors are used to measure the mass of water that evaporates from the water pan during the experiment. Four load sensors located at each corner of the water tray (Figure 2.3) give a total load capacity of 8 kg. The uncertainty of the load sensors are determined by in-situ calibration with calibration masses. First, a base reading is established by loading up the water tray with masses until the total mass is approximately 6750 g, which corresponds to the lowest measured mass in the convective mass transfer experiments. This mass is recorded every 15 seconds for 10 consecutive readings. The average of the 10 mass readings is determined to obtain an average base reading. Once the base reading is determined, successive calibration masses are placed on the pan and an average mass reading is measured. Figure 2.12 shows the difference between the mass readings with the calibration masses and the base reading. The base

reading is the data point on the graph where the mass difference is 0 g. The 95% standard deviation of the average of the mass readings is an indication in the repeatability in the mass measurement, and is shown with error bars on the graph. Since the error bars of each mass overlap the uncertainty in the base reading, the load cells are found to be measuring the correct mass within uncertainty limits. The bias uncertainty in the mass measurement of the load cells is taken as ±2 g, which corresponds to the maximum mass difference for the majority of the mass readings shown in Figure 2.12.

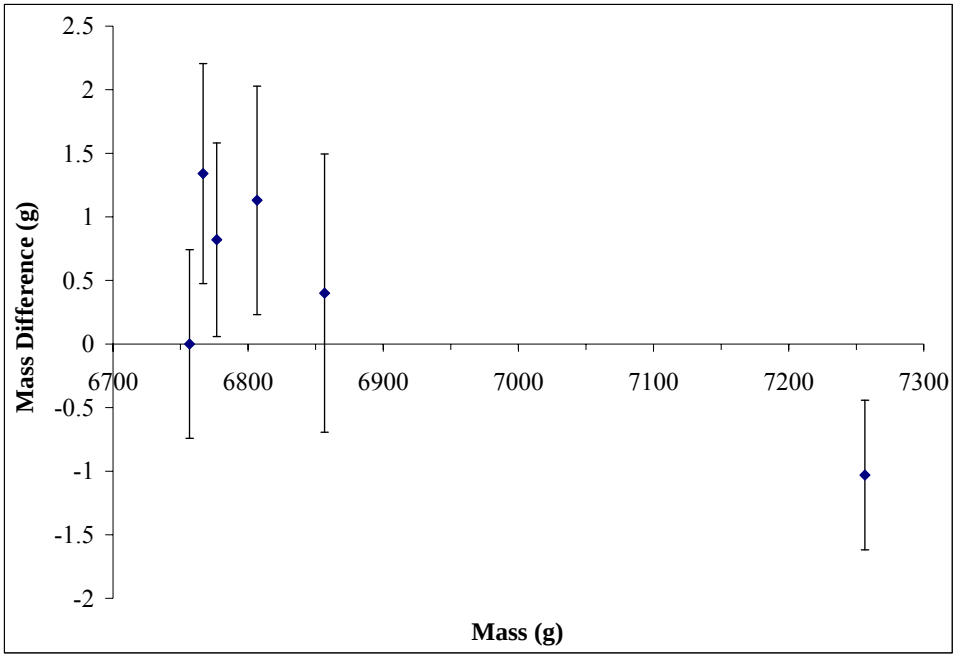

Figure 2.12 Calibration of the load sensors with in-situ calibration masses. The difference between the average load sensor reading and the base reading is shown. The 95% uncertainty of the average mass reading is shown with error bars.

2.3.4 Orifice Plate

Located further downstream of the test section is a rectangular to circular transition section that has a circular duct (D = 72.5 mm) connected to it (not shown in schematics). The circular duct contains a tapered orifice plate that is located 32D downstream of the transition section. The pressure drop across the orifice plate is used to calculate the mass

flow rate of air within the test section of the TMT. 15-mm and 30-mm tapered orifice plates are used for the laminar and turbulent flow regimes respectively. The pressure differential across the orifice plate is measured with a Validyne DP103-12 electronic pressure transducer with a full-scale reading of 5 inH_2O (1244 Pa) (bias uncertainty is determined in Section 2.3.5).

The mass flow rate using ISO 5167-1 (1991) for orifice plates with D and D/2 pressure tappings could not be accurately determined, since the standard was not developed for laminar flow at the orifice plate (which also coincides with laminar flow through the test section of the TMT). Therefore, a separate apparatus is constructed in order to calibrate the 15-mm orifice plate for laminar flow.

The apparatus constructed to calibrate the orifice plate consists of two mass flow controllers with a bias uncertainty of ±0.043 g/s each and circular ducting with the same diameter as the ducting in the TMT facility. Upstream of the orifice plate, ducting with the same length as in the TMT (2.29 m or 32D) and a longer length (4.58 m or 63D) are used to determine if there are any flow development effects since the airflow may not be fully developed at the orifice plate within the TMT. A downstream length of 0.90 m (12D) is used, since this is the same length in the TMT. Figure 2.13 shows the calibration curve for the 15 mm orifice plate, with the two different lengths of upstream pipe. It is found that the lengths of the upstream section tested did not produce any appreciable change in results. From calibration, the orifice plate produces a 9% increase in mass flowrate, compared to the ISO standard (ISO 5167-1, 1991). The mass flow rate

equation determined from the measured pressure drop in the experiment for the 15-mm orifice plate is

$$\dot{m} = 0.00017\Delta p^{0.5}, \tag{2.1}$$

where the units used are the same as in Figure 2.13. The bias uncertainty in the above equation is dependant on the pressure differential being measured. Over the calibration range of 0.2 inH_20 (50 Pa) to 5.0 inH_20 (1244 Pa), the bias uncertainty ranges from ±13% to ±1%. The major contribution to this uncertainty is from the bias uncertainty in the pressure transducer, which becomes relatively larger as the pressure difference reduces. For the experimental conditions in this research, the pressure differential is between 0.4 inH_20 (100 Pa) and 5.0 inH_20 (1244 Pa), which results in bias uncertainties between ±7% and ±1%,

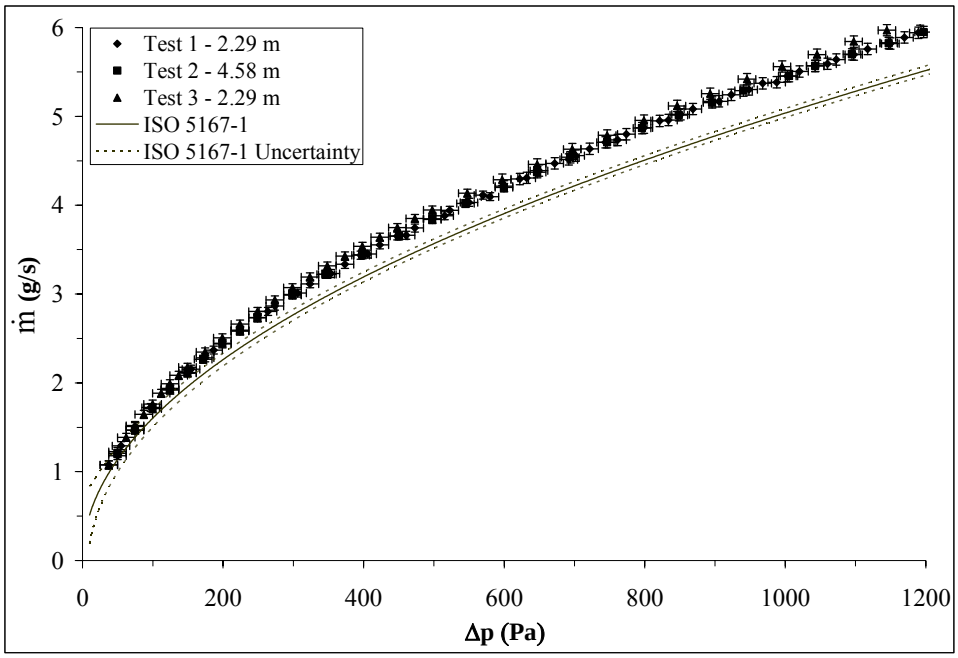

Figure 2.13 Calibration data for the 15-mm orifice plate compared to ISO 5167-1 (1991) for three laminar flow trials with different upstream development section lengths. The 95% bias uncertainties in the measured parameters are shown with error bars.

To improve the accuracy for turbulent flow through the test section, the 30-mm orifice plate is also calibrated. The calibration results, shown in Figure 2.14, show that when the flow is turbulent before the orifice plate, the measured and calculated (ISO 5167-1, 1991) mass flowrates agree better than when the flow is laminar (which is expected). The resulting calibration equation is

$$\dot{m} = 0.00069\Delta p^{0.5}, \tag{2.2}$$

and has a bias uncertainty of ±1 to ±3% over the range of flow rates that occur during the convective mass transfer experiments.

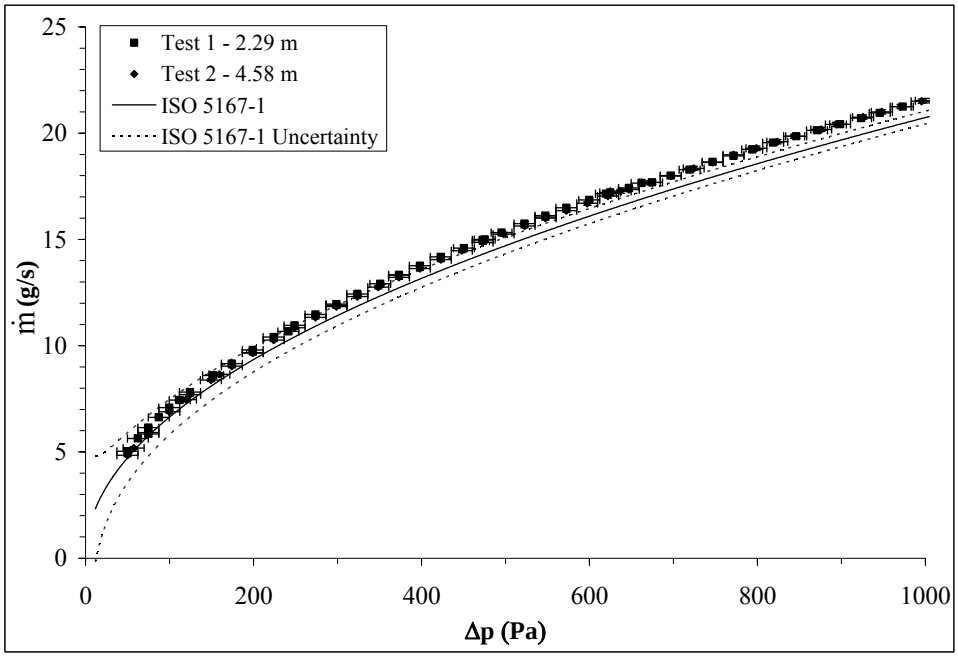

Figure 2.14 Calibration data for the 30-mm orifice plate compared to ISO 5167-1 (1991) for two turbulent tests with different upstream development section lengths. The 95% bias uncertainties in the measured parameters are shown with error bars. The uncertainties in the mass flowrate are too small to be viewed on the graph.

2.3.5 Pressure Transducer

A water manometer is used to calibrate the pressure transducer that is used to measure the pressure drop across the orifice plate. The transducer has a maximum output of

5 volts, and is calibrated up to a pressure drop of 5 inH_20 (1244 Pa). The pressure transducer is calibrated at two different pressure differences: 0 inH_20 and 5 inH_20 (1244 Pa). After calibration, the pressure transducer is checked against the water manometer at a range of pressures, and the differences between the readings of the two instruments are given in Figure 2.15. The maximum difference between the manometer and the orifice plate is 0.01 inH_20 (2.5 Pa). The precision uncertainty of the water manometer is ±0.05 inH_20 (12.5 Pa), which corresponds to half a division on the manometer scale. Since the pressure reading differences between the two instruments are much smaller than the precision uncertainty in the manometer, the total uncertainty in the pressure transducer is mainly due to the precision uncertainty in the water manometer, and is ±0.05 inH_20 (12.5 Pa).

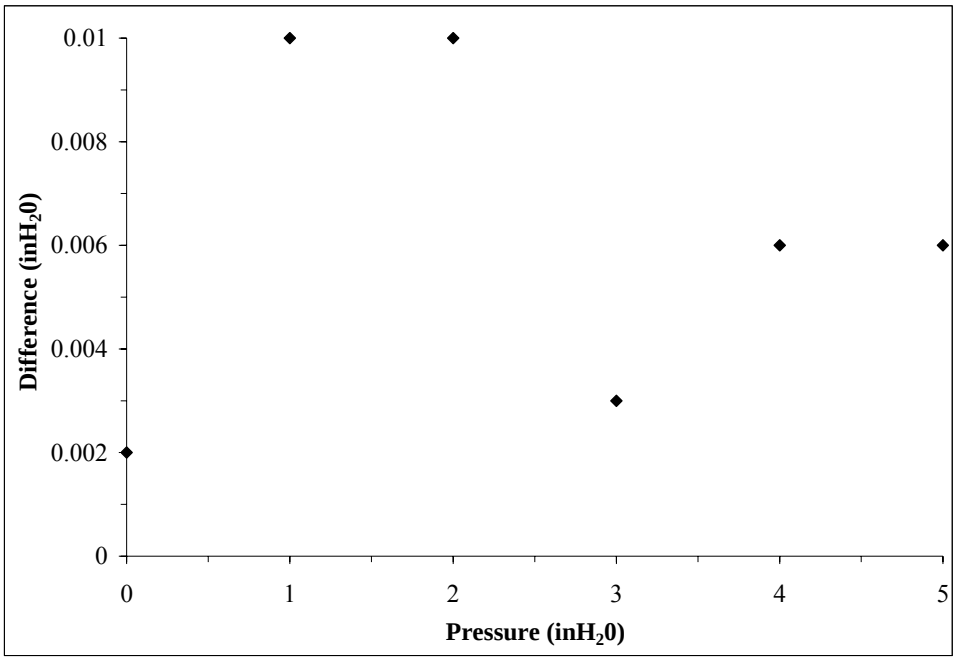

Figure 2.15 Post-calibration pressure differences between the pressure transducer and water manometer.

CHAPTER 3

DATA ANALYSIS

3.1 Introduction

This chapter presents preliminary experiments that determine the precision uncertainty of the measured data during the transient and steady state time periods of the convective mass transfer experiments. As well, steady state experiments are performed to determine the bias and precision uncertainty of the water surface temperature. Following this, the equations that are used to determine property data, the flow conditions of the air and the convective mass transfer coefficient are presented. Finally, the conservation equations of heat and mass are applied to ensure that the experiment satisfies these equations within uncertainty bounds.

3.2 Transient Data and Precision Uncertainty

The following section will present experimental data from a laminar and turbulent test, showing the pre-test transient period and the steady state period. The data will show when steady state has been achieved, and will help quantify the precision uncertainty of the experiment.

A steady state energy balance results when the evaporation of water reduces the temperature of the water to a point where the sensible heat transfer from the air to the water equals the latent heat required to evaporate water from the pan. Prior to this

(e.g. t < 8 to 10 hours), the experiment is in a transient state as shown in Figure 3.1 and Figure 3.2 for tests at a Re_D of 1500 and 6000.

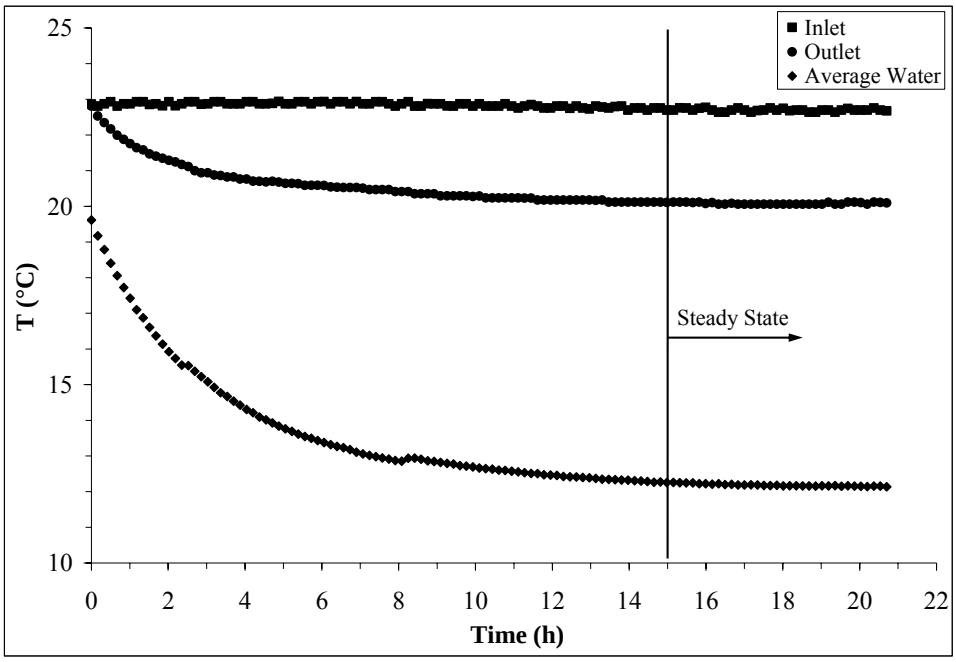

Figure 3.1 Temperature of the air entering and leaving the test section and the average surface temperature of the water for Re_D = 1500.

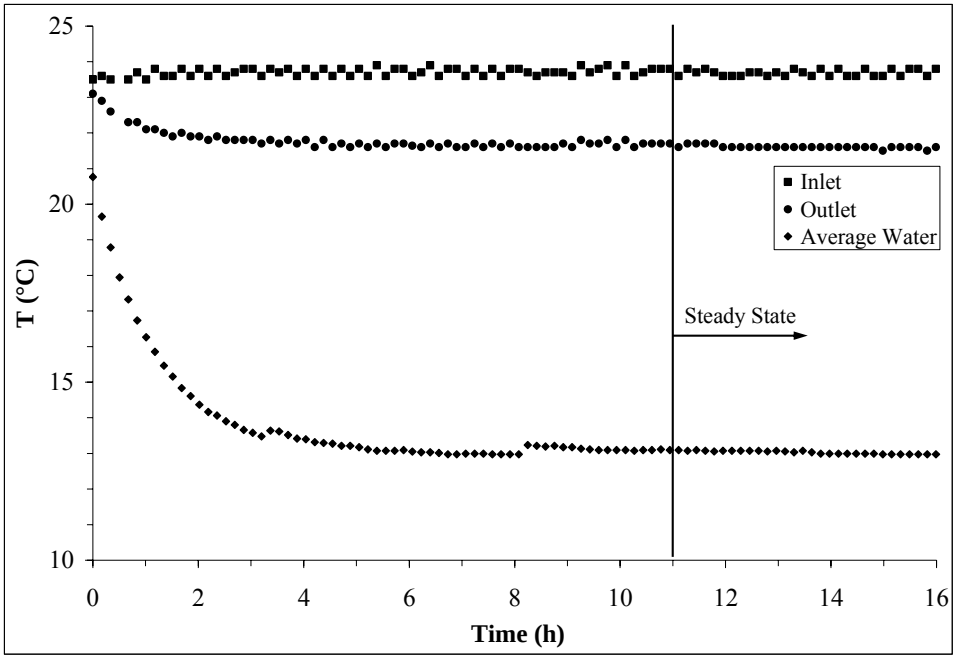

Figure 3.2 Temperature of the air entering and leaving the test section and the average surface temperature of the water for $Re_D = 6000$.

Figure 3.1 and Figure 3.2 show the temperature measurements of the air at the inlet and outlet of the test section as well as the average temperature of the water surface. At the beginning of each test, the water in the tray had an initial temperature of approximately 20°C, and once the airflow passes through the test section, evaporation reduced the temperature of the water and the air leaving the test section. The water and air temperatures continue to decrease until an equilibrium (or steady) state exists, where the heat loss from the air equals the heat required to evaporate the water. Steady state is determined by selecting a period during the experiment (determined by visual inspection) when all temperature measurements are within ± 0.1°C and the air relative humidity measurements are within $\pm 0.2\%$ RH of the average measurement for that time period. The time selected to reach steady state is greater for laminar flow (15 hours) than for turbulent flow (11 hours) due to the lower convection rates in the laminar flow. All

individual air temperature data points are within ± 0.1°C from the mean and the water temperature data points are ± 0.1°C from the mean between hours 15 and 21 for laminar flow and hours 11 and 16 for turbulent flow.

Figure 3.3 and Figure 3.4 show the relative humidity at the inlet and outlet of the test section for the laminar and turbulent tests, respectively. The humidity fluctuations are less than $\pm 0.2\%$ RH during the steady-state periods. Since the fluctuations of the temperature and humidity shown in Figure 3.1 through Figure 3.4 are small during these steady state periods, steady state is deemed to occur.

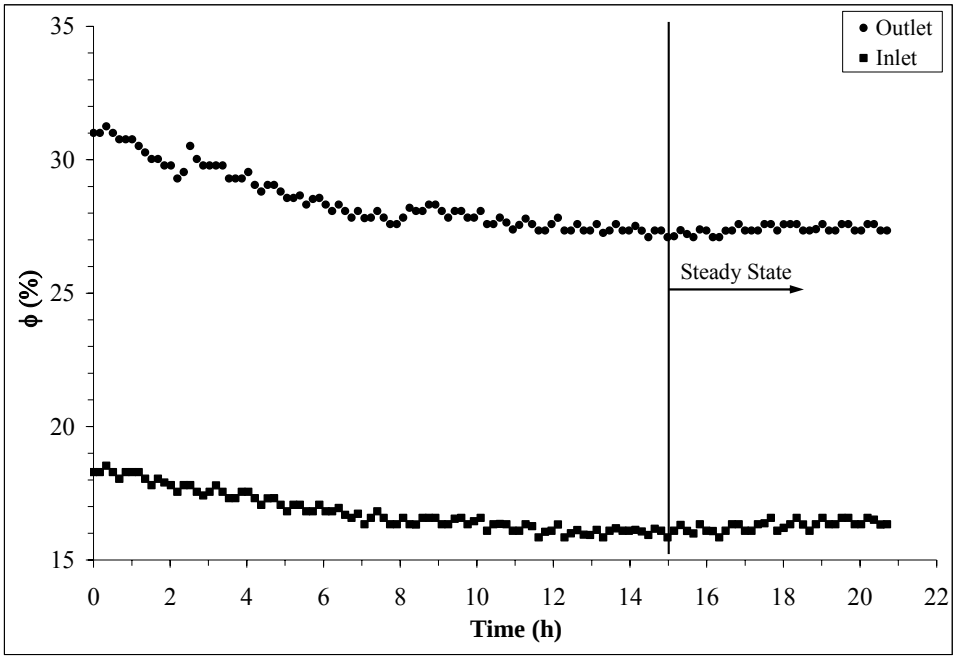

Figure 3.3 Relative humidity of the air entering and leaving the test section for $Re_D = 1500$.

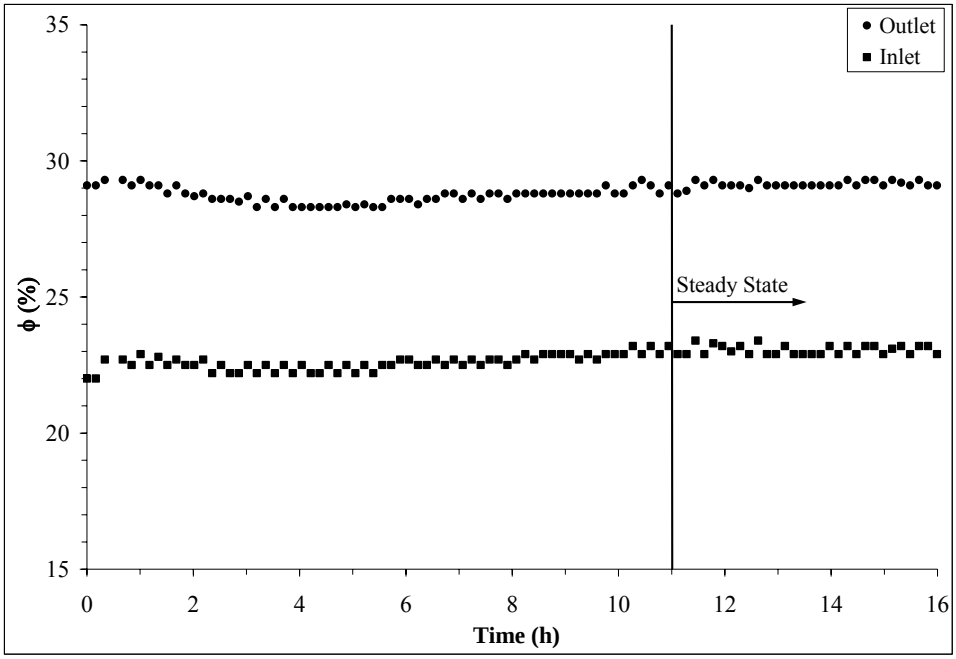

Figure 3.4 Relative humidity of the air entering and leaving the test section for $Re_D = 6000$.

The mass of the water pan during the experimental period is shown in Figure 3.5. The water height is level with the top of the pan at a mass of approximately 7200 g, which is found by measuring the height (30 mm) of the water in the center of the pan. Over the range of Re_D tested, the surface of the water was viewed (through an inspection window located on the side of the test section) to be steady (no ripples or waves). During the experiment, water evaporates from the pan and is periodically filled during the transient period to keep the pan as full as possible during the steady state portion. The water is added through a hole in the top of the test section cover. The hole in the cover is sealed when the pan is not being filled. The instantaneous changes in mass at $t \approx 3$ h and $t \approx 8$ h are a result of the pan being filled to make up for any evaporated water during the test. The effect of the addition of water can also be seen in Figure 3.1 and Figure 3.2 where the temperature of the water increases at these two respective times since the

water temperature being added is above that of the water in the pan. The pan is slightly over filled (i.e., above 7200 g) to create a water surface above that of the top of the pan to decrease the number of times the pan has to be filled before the steady state period begins. A linear curve fit is performed on the data during the steady state periods to determine the average evaporation rate during this time. The linear curve fits give a correlation coefficient (r^2) of 0.997 for $Re_D = 1500$ and 1.000 for $Re_D = 6000$, suggesting that the evaporation rate is constant during the steady state periods. The 95% precision uncertainty in the average value of $\dot{m}_{evap}$ is ±0.4 g/h (±2.4%) for $Re_D = 1500$ and ±0.5 g/h (±1.1%) for $Re_D = 6000$ during the steady state period.

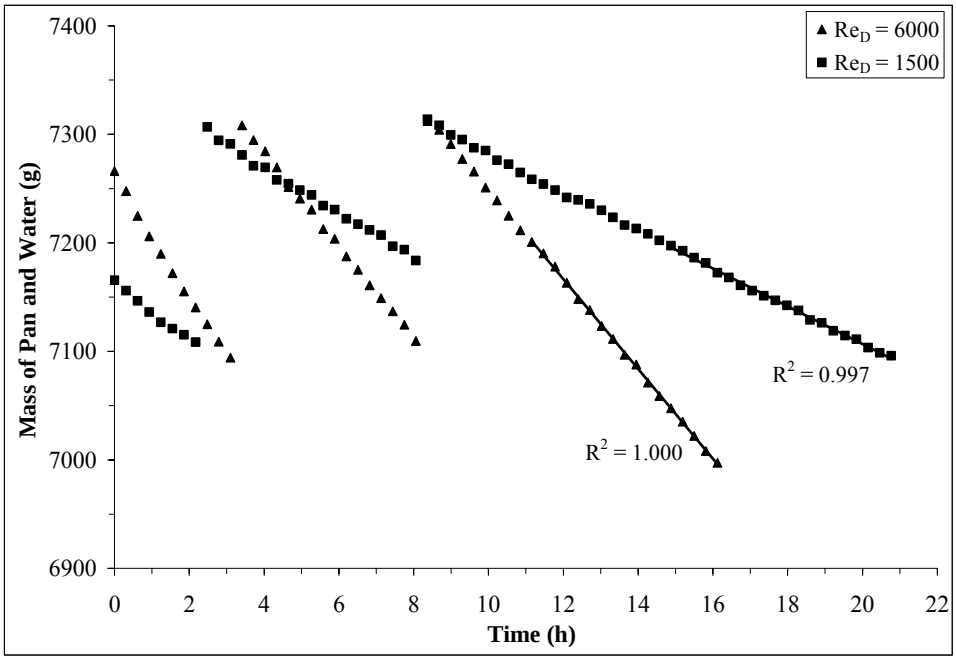

Figure 3.5 Measured mass of pan and water during test with laminar and turbulent flow.

Figure 3.6 shows the average mass evaporation rate over 2 hour time periods for the two experimental tests. For example, for hour 1, data are averaged over hours 0 and 2. At first, the evaporation rate ($\dot{m}_{evap}$) is the greatest since the water temperature is the

highest at the beginning of the trial, but $\dot{m}_{evap}$ decreases during the experiment as the water temperature decreases. During the steady state period, the 95% precision uncertainty (tSEE) is ±3 g/h (±17%) for Re_D = 1500 and ±1.7 g/h (±4%) for Re_D = 6000.

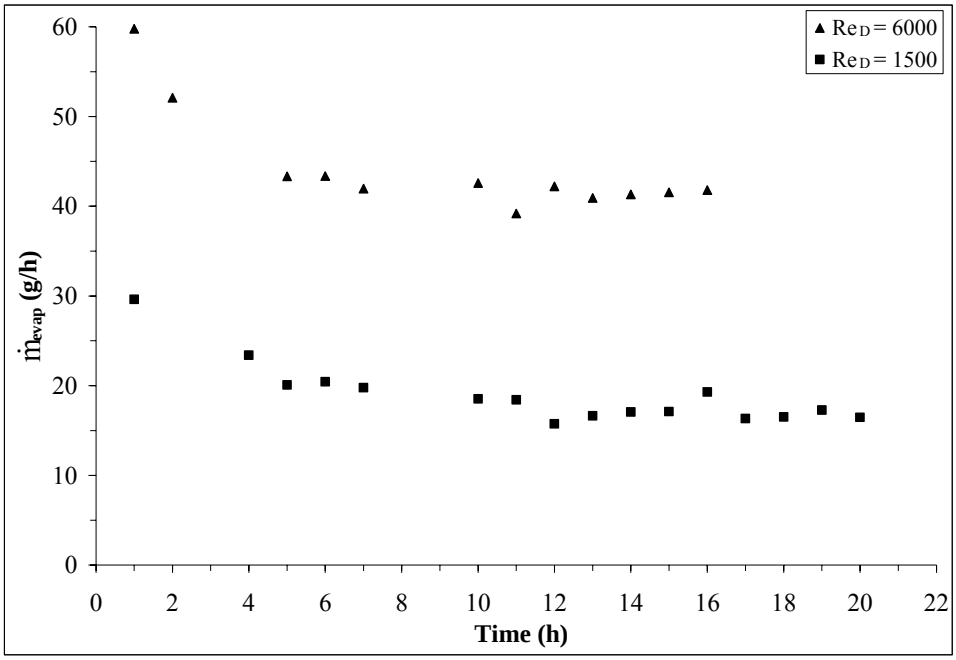

Figure 3.6 Measured evaporation rate of water for the laminar and turbulent tests.

Figure 3.7 presents Sh_D (defined in Section 3.4.5) as a function of time during the experiments by averaging the temperature, relative humidity and mass measurements over 2 hour periods. Sh_D is based on $\dot{m}_{evap}$ from Figure 3.6, which causes the profiles of $\dot{m}_{evap}$ and Sh_D to be relatively similar, especially after the experiment has started to run for a few hours. If $\dot{m}_{evap}$ is determined using the slope in Figure 3.5, the Sh_D results change little and are not presented. During the steady state period, the average Sh_D, calculated from the 2 hour averages in Figure 3.7 (i.e., based on Figure 3.6), is within ±1.5% (Re_D = 1500) and ±0.2% (Re_D = 6000) of the average Sh_D that is determined using the slope in Figure 3.5. Since the hourly Sh_D does not vary greatly over the steady

state time period, the experimental data are averaged over the entire steady state time period, and one Sh_D is calculated for each test condition. The evaporation rate is determined using the slope (e.g., Figure 3.5) because it results in the smallest precision uncertainty (±3%) in Sh_D.

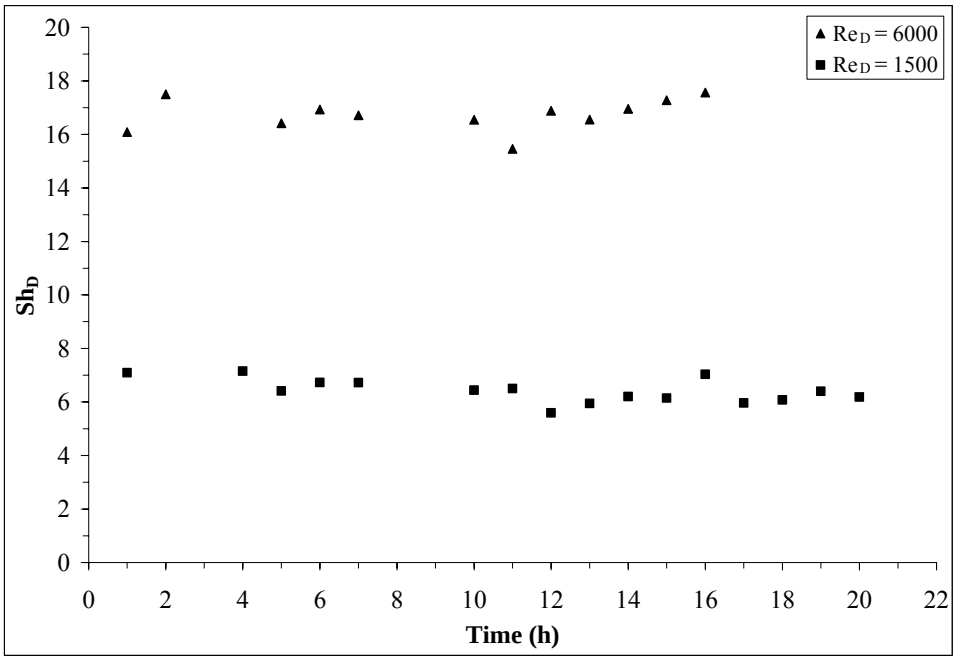

Figure 3.7 Calculated Sherwood number for tests with laminar and turbulent flow.

The repeatability of the experiment is determined from two different sets of data, one for laminar flow and one for turbulent, by comparing experimental tests with similar test conditions. At $Re_D = 1400$ and 4300, Sh_D was repeatable within ±1.1% and ±2.4%, respectively, when the relative humidity and temperature difference of the airflow entering the test section between two trials are less than 3% RH and 0.1°C. Sh_D compares well when similar operating conditions exist, which shows the high repeatability of the experiment and confirms the precision uncertainty of ±3% in Sh_D.

3.3 Bias and Precision Uncertainty of the Surface Water Temperature

Preliminary experiments are conducted to determine if the water surface temperature is uniform across the water surface area and the pan depth. Temperature gradients within the water along the depth, length and width of the pan during an experimental tests may cause or result from buoyancy induced fluid circulation. Fluid circulation would be in the form of evenly spaced rolls, which could create a rough water surface, as well as an unstable temperature gradient within the water.

The temperature gradient along the depth of the water is measured by placing one thermocouple 2 mm below the surface of the water, and one at the bottom of the pan at the same location within the pan. Two sets of temperature measurements are taken along the center width of the pan, at Z = 200 and 400 mm (Figure 2.2). The conditions of the air entering the test section are 22°C and 20% RH at a Re_D of 1900. Temperature readings are taken once the temperature of the water is observed to be constant. The temperature difference between the surface of the water and the bottom of the pan are given in Figure 3.8 for an 8-hour test. The results show that the temperature gradient along the depth of the pan is typically no greater than 0.1°C. At one location, the temperature at the surface is higher than at the bottom, and in the other location, the opposite occurs. The difference in the temperature gradient between the two locations may be due to the bias uncertainty in the thermocouples which are typically ±0.1°C (Section 2.3.1), or an unstable temperature gradient due to natural convection. The presence of natural convection within the water can be determined by calculating a Rayleigh number (Ra_d) (Incropera and DeWitt, 2002), which is based on the temperature

difference between the surface (T_s) of the water and the water at the bottom (T_b) of the pan.

$$Ra_d = \frac{g\beta(T_b - T_s)d^3}{\nu\alpha}, \tag{3.1}$$

where, g is gravitational acceleration, β is the coefficient of thermal expansion of water, d is the average water depth, ν is the kinematic viscosity of water and α is the thermal diffusivity of water.

The Rayleigh number for a temperature difference of 0.1°C for an average water depth (d) of 0.0295 m, results in $Ra_d = 16{,}000$. For Rayleigh numbers in the range $1708 < Ra_d < 50{,}000$, fluid motion consists of regularly spaced roll cells (Incropera and DeWitt, 2002). The Nusselt number for the given Rayleigh number, based on the correlation given in Incropera and DeWitt, 2002, is 2.7. Since the Nusselt number is 2.7 times larger than the Nusselt number for pure conductive heat transfer (Nu = 1), heat transfer through the water is dominated by free convection. The effects of free convection in the convective mass transfer experiments will be seen as a precision uncertainty in the temperature measurement of the surface of the water. A separate experiment is conducted to determine this precision uncertainty, and these experimental results are given next.

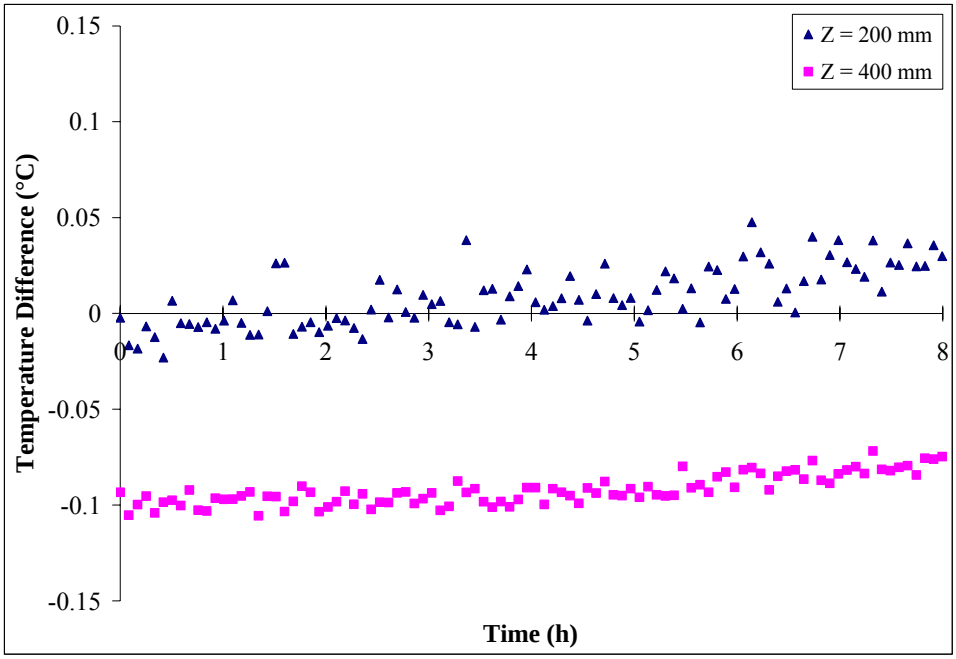

Figure 3.8 Measured temperature gradient along the depth of the water pan at two locations (Z = 200 and 400 mm) down the center width of the pan.

The variation of the surface water temperature along the length and width of the water pan for three experimental tests are given in Figure 3.9. The temperature readings are taken once the water surface temperature is viewed to be constant over the eight thermocouple readings. The temperature difference between each thermocouple and the average of all 8 thermocouples is given for three different Reynolds numbers. It is shown that the water temperature readings across the width and length of the pan vary by less than ±0.15°C, and typically less than ±0.1°C, which are within the bias uncertainty of the thermocouples (determined in Section 2.3.1). Even though free convection may be present within the water, the effects are not important, since the temperature difference between the thermocouples is not large enough to cause a significant precision uncertainty in the measured data. Since these temperature readings are within the bias uncertainty of the instruments, the eight temperature readings are

averaged for each convective mass transfer experiment and one temperature is reported as the average temperature of the surface of the water. The total uncertainty of the average temperature reading is based on the bias and precision uncertainties of the eight temperature readings.

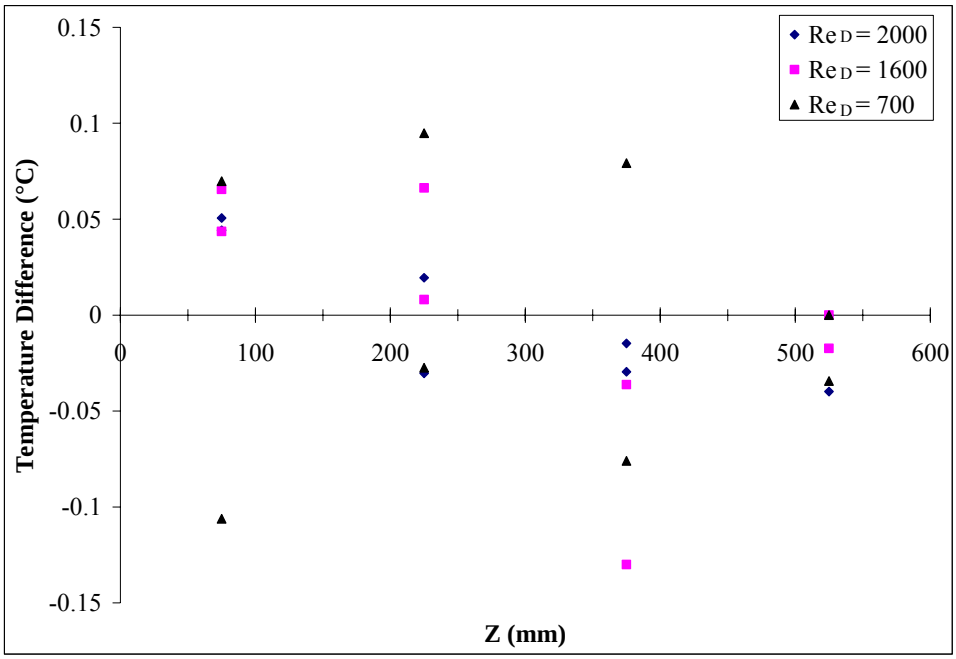

Figure 3.9 Temperature difference from the mean along the length of the pan. The thermocouples are spaced as shown in Figure 2.2.

The temperature gradient along the depth of the water pan is typically less than 0.1°C, and the average temperature readings of the eight thermocouples near the surface of the water are within ±0.1°C of the average surface water temperature. Therefore it is satisfactory to average the eight thermocouple readings for each experimental trial since the differences between the thermocouple readings are within the bias uncertainty of the thermocouples.

Steady state operating conditions are important since they allow an averaged convective mass transfer coefficient to be determined over the testing time period for a specific set of relative humidity, temperature and mass flowrate conditions of the upstream airflow. The test procedure allows steady state conditions to be achieved by operating the convective mass transfer experiment until the temperature and relative humidity of the air and the water temperature are viewed to be constant. The water that evaporates from the pan during this time period is replaced until steady state conditions are observed. After steady state conditions are reached, each test is conducted for four to eight hours (depending on the specific testing conditions) and the data acquired are averaged over this time span.

3.4 Dimensionless Variables and Properties

The main objective of the data reduction is to calculate the independent parameters: Reynolds number (Re), Rayleigh number (Ra), a non-dimensional development length (Gz^{-1}), an operating condition factor (H*), as well as the dependent parameter, Sherwood number (Sh), from the experimental data. The 95% confidence intervals for the calculated independent and dependent parameters are determined according to ANSI/ASME PTC 19.1 (1998), which includes both bias and precision uncertainties. Further detail in determining the 95% confidence intervals for the independent and dependent parameters are given in Appendix A.

3.4.1 Reynolds Number

The Reynolds number (Re_D) of the airflow through the rectangular test section is based on its hydraulic diameter. The cross-section of the test section is shown in Figure 2.4. The Reynolds number is given as

$$Re_D = \frac{4\dot{m}}{\mu_f P}, \tag{3.2}$$

where P is the perimeter of the rectangular duct,

$$P = 2(W + H + h), \tag{3.3}$$

and $\dot{m}$ is the mass flowrate of air. μ_f is the viscosity of dry air because humidity has a small effect (less than 0.3%) for the conditions in this thesis (Chuck and Sparrow, 1987; Prata and Sparrow, 1986; and Wexler and Wildhack, 1965). μ_f is determined with the Sutherland law (White, 1999) at film temperature (T_f),

$$\mu_f = \mu_o \left(\frac{T_f}{T_o}\right)^{3/2} \left(\frac{T_o + S}{T_f + S}\right), \tag{3.4}$$

with T_o = 273 K , μ_o = 1.71 E-5 kg/(m·s), S = 110.4 K and

$$T_f = \frac{T_s + \frac{T_1 + T_2}{2}}{2}, \tag{3.5}$$

where T_s is the temperature at the surface of the water, and T_1 and T_2 are the bulk temperatures of the airflow upstream and downstream of the test section, respectively. The duct perimeter varies depending on the average change in height (h) between the top of the pan and the surface of the water during an experimental trial. During most trials, the average change in the water height from the full state is 0.5 mm. This change in height results in a 0.2% increase in the perimeter compared to the full state, which has negligible effect on Re_D during an experimental trial, but is included for completeness. The uncertainty in Re_D for the airflow in the experiment is ±4%, which is mainly due to the uncertainty in the mass flow rate of the air.

3.4.2 Rayleigh Number

Temperature and concentration differences exist between the surface of the water and the bulk airflow. The evaporation process causes the vapor concentration to be highest and the temperature to be lowest at the surface of the water. The resulting density difference between the air-water vapor mixture at the surface of the water and in the bulk air stream results in natural convection, which can be quantified with a Rayleigh number (Ra_D) defined as

$$Ra_D = \left[\frac{[g\bar{\rho}_g(\rho_{g,s} - \rho_{g,\infty})D_h{}^3}{\mu_f{}^2} \right] Sc, \tag{3.6}$$

where D_h is the average hydraulic diameter of the test section during the test, $\bar{\rho}_g$ is the mean mixture density of the air in the boundary layer, $\rho_{g,s}$ is the is the density of moist air at the surface of the water, $\rho_{g,\infty}$ is the density of moist air in the ambient.

D_h varies depending on the average change in height (h) of water during an experimental trial:

$$D_h = \frac{4(WH + wh)}{2(W + H + h)}. \tag{3.7}$$

The uncertainty in D_h for this experiment is ±2%. It should be noted that the average change in height (h = 0.5 mm) accounts for a 2% increase in the hydraulic diameter compared to that of the full state.

The density of moist air at the surface of the water ($\rho_{g,s}$) is based on the sum of the partial densities of water vapor and dry air at the surface of the water,

$$\rho_{g,s} = \rho_{v,s} + \rho_{a,s}. \tag{3.8}$$

The partial pressure of water vapor at the surface of the water ($p_{v,s}$) is calculated using psychrometrics (ASHRAE Fundamentals, 2005), where

$$p_{v,s} = p_{sat}(T_s). \tag{3.9}$$

The partial pressure of air at the surface of the water ($p_{a,s}$) is calculated assuming that the total pressure (p_g) is constant,

$$p_{a,s} = p_g - p_{v,s}. \tag{3.10}$$

Due to low airflow velocities within the test section of the TMT facility (over the range of Re_D tested in this thesis), the total pressure within the chamber is not significantly different than the atmospheric pressure within the laboratory. As a result, the total pressure (atmospheric pressure) is measured in the laboratory with a mercury barometer during each experimental trial. The ideal gas law is used to determine $\rho_{v,s}$ and $\rho_{a,s}$ at T_s. The density of moist air in the ambient ($\rho_{g,\infty}$) is the average of the inlet and outlet densities,

$$\rho_{g,\infty} = \frac{\rho_{g,1} + \rho_{g,2}}{2}. \tag{3.11}$$

With the use of the ideal gas law and the measurements of the relative humidity and dry bulb temperatures upstream and downstream of the test section, the water vapor and dry air densities are determined at these two locations. The partial pressure of water vapor is determined by:

$$p_{v,i} = \phi_i p_{sat}(T_i), \tag{3.12}$$

$$p_{a,i} = p_g - p_{v,i}, \tag{3.13}$$

where i = 1 at the inlet and i = 2 at the outlet of the test section. The mean mixture density of air in the boundary layer ($\overline{\rho}_g$) is

$$\overline{\rho}_g = \frac{\rho_{g,s} + \rho_{g,\infty}}{2}. \tag{3.14}$$

The bias uncertainty in Ra_D is ±8%, which is mainly due to the uncertainty in D_h.

3.4.3 Inverse Graetz Number

A dimensionless axial distance (X*) in the flow direction for the entrance region of the rectangular duct is typically specified as the inverse of the Graetz number (Gz). For mass transfer,

$$X^* = \frac{L}{D_h Re_D Sc} = \frac{1}{Gz}. \tag{3.15}$$

X* is a measure of how developed the concentration boundary layer is for any length of duct. The concentration boundary layer is considered to be developing for X* < 0.05 (Incopera and DeWitt, 2002) and in this thesis the maximum value of X* is 0.04. The bias uncertainty in X* is ±5%.

3.4.4 Mass and Thermal Diffusion Relationship

A measure of the importance of the energy transport through mass diffusion relative to that through thermal diffusion is represented by S* (Lin et al., 1992; Jang et al., 2005), where

$$S^* = \frac{\rho_g D_{AB} h_{fg} \Delta W}{k_g \Delta T}. \tag{3.16}$$

S* is a result of simultaneous heat and mass transfer due to the evaporation process, which varies throughout the experiment depending on the conditions of the air entering

the test section. This dimensionless parameter is similar to the dimensionless operating condition factor (Yan, 1996; Simonson and Besant, 1999a,b; Zhang and Niu, 2002)

$$H^* = 2500\frac{\Delta W}{\Delta T}, \tag{3.17}$$

where

$$\Delta W = W_s - W_l, \tag{3.18}$$

$$\Delta T = T_s - T_l \tag{3.19}$$

and the coefficient (2500) has units of kg·K/kg. H* accounts for the coupling between heat and moisture transfer and varies between -3.6 and -1.4 for the experimental conditions in this thesis. The differences between H* calculated with equation (3.17) and S* calculated with equation (3.16) are less than ± 0.3, and the small differences are mainly due to the constant properties used in calculating the coefficient of 2500 kg·K/kg in equation (3.17). Since H* is an important parameter when correlating the effectiveness of air-to-air energy exchangers (Simonson and Besant, 1999a,b) it will be used in this research as well to correlate Sh_D and show the effect of operating conditions on the convective mass transfer coefficient.

3.4.5 Sherwood Number

The Sherwood number (Sh_D) represents a dimensionless concentration gradient at the interface between the air and water. Sh_D non-dimensionalizes the convective mass transfer coefficient (h_m) and is based on the hydraulic diameter (D_h) of the test section.

$$Sh_D = \frac{h_m D_h}{D_{AB}}, \tag{3.20}$$

where D_h is from equation (3.7) and the convective mass transfer coefficient (h_m) depends on the measured evaporation rate of water ($\dot{m}_{evap}$), the surface area of the water pan ($A_s = w \cdot L$), and the log mean vapor density difference ($\Delta\rho_v$) between the bulk air and the surface of the water.

$$h_m = \frac{\dot{m}_{evap}}{A_s \Delta\rho_v} \tag{3.21}$$

$$\Delta\rho_v = \frac{(\rho_{v,s} - \rho_{v,2}) - (\rho_{v,s} - \rho_{v,1})}{\ln[(\rho_{v,s} - \rho_{v,2})/(\rho_{v,s} - \rho_{v,1})]} \tag{3.22}$$

The binary diffusion coefficient (D_{AB}) for water vapor in air up to 1100°C depends on T_f and p_g and is calculated from ASHRAE Fundamentals (2005).

$$D_{AB} = \frac{0.000926}{p_g}\left(\frac{T_f^{2.5}}{T_f + 245}\right) \tag{3.23}$$

The 95% confidence intervals for Sh_D are strongly dependent on the log mean density difference between the air and the water ($\Delta\rho_v$) and the evaporation rate ($\dot{m}_{evap}$). For the range of test conditions in this thesis, $\dot{m}_{evap}$ and $\Delta\rho_v$ have bias uncertainties in the range of $\pm 1\%$ to $\pm 5\%$ and $\pm 2\%$ to $\pm 8\%$ respectively, resulting in bias uncertainties in Sh_D of $\pm 3\%$ to $\pm 9\%$.

3.5 Mass and Energy Balances

In any experiment, it is important to verify that mass and energy are conserved. Applying the basic principles of conservation of mass and energy over a control volume can help determine how well the experiment is set up to measure heat and mass transfer, and identify bias errors in the experiment. It is important that mass and energy balances are satisfied within experimental uncertainties. If the mass and energy balances are not

satisfied within the experimental uncertainties, systematic errors exist within the experiment, such as heat and mass transfer with the ambient environment or improper setup of the experiment and instruments, or the measurement uncertainties have been underestimated.

As noted previously, it is essential to mix the air leaving the test section to accurately measure the bulk relative humidity and temperature. In the experiment, the evaporation of water from the tray is measured using load sensors and the change in humidity of the air stream is measured with humidity sensors. By comparing the evaporation measured with the load sensors to the moisture gained by the air as it travels through the test section, as measured by the humidity sensors, the adequacy of the mixing section downstream of the test section (Figure 2.2) can be determined. The mass balance is satisfied within the experimental uncertainties for all tests when the mixing section is used and when the humidity of the air entering the test section (ϕ_1) exceeds 80% RH regardless of whether the mixing section is used or not. When $\phi_1 > 80\%$ RH, the water vapor density difference between the surface of the water and the air stream entering the test section is small and the downstream mixing section has a small effect on the results because the vapor density is quite uniform in the boundary layer. On the other hand, the mass balance is not satisfied within the experimental uncertainty when the mixing section is not used and $\phi_1 < 80\%$ RH.

The bias uncertainty in the evaporation rate determined using the load sensors (±1 to ±5%) is as much as 10 times lower than the bias uncertainty in the evaporation rate determined using the measured humidity and temperature difference between the inlet

and outlet air streams. Therefore, the outlet conditions of the airflow can be accurately calculated by applying mass and energy balances across the test section using the evaporation rate measured by the load sensors. If the outlet temperature and relative humidity conditions of the air stream are calculated in this way, Sh_D changes by less than $\pm 4\%$ compared to the case where Sh_D is determined using the outlet conditions measured downstream of the mixing section. This uncertainty is within the experimental uncertainty and verifies the energy and mass balances in the experiment. A similar agreement exists for the tests when $\phi_1 > 80\%$ RH with or without the mixing section.

In the tests where the mixing section is not used and $\phi_1 < 80\%$ RH, Sh_D is as much as $\pm 16\%$ different when using the calculated and measured outlet air temperatures and humidities. As this is outside the 95% confidence limits for this experiment, it indicates a systematic error when a mixing section is not used.

About half of the tests are performed without the mixing section and with $\phi_1 < 80\%$ RH, resulting in mass balances outside the experimental uncertainty. Instead of rejecting these data, a Sh_D based on the calculated outlet air conditions is used for these experiments. The bias uncertainty associated with this calculation increases the uncertainty in Sh_D by 1 to 6% (depending on the vapor density difference between the air and the water surface) and is included in the reported uncertainty values.

CHAPTER 4

MEASURED CONVECTIVE COEFFICIENTS

4.1 Introduction

Chapter 3 presents experiments that are conducted to analyze the transient response of the convective mass transfer experiments. In this chapter, only the steady-state experimental data are used to determine the steady state convective mass transfer coefficient for the rectangular test section of the TMT facility. A summary of the experimental conditions (water surface temperature, Reynolds number, air relative humidity and temperature) that occur for the laminar and turbulent flow experiments are given. The effect of the air relative humidity on the convective mass transfer coefficient is shown. The Sh_D data obtained during the steady state period for a range of test conditions as well as the correlations developed from this data are provided in this chapter. Comparisons to data in the literature are also given.

An analogy between heat and mass transfer is developed in this chapter to determine the convective heat transfer coefficients from the measured convective mass transfer results. The analogy is used in the development of a new method that is able to convert a pure heat transfer Nu and a pure mass transfer Sh into a Nu and Sh for simultaneous heat and mass transfer. The new method is applied to a case found in the literature to determine its feasibility.

4.2 Convective Mass Transfer Coefficient

When performing the experiment to measure the convective mass transfer coefficient, a range of test conditions is used, but each experimental test is carried out with constant upstream air properties: temperature, relative humidity and mass flowrate. The temperature of the air upstream of the test section is typically 23°C, but three tests are performed with an air temperature of 37°C. The tests cover a range of air relative humidities from 15% to 80% and Re_D through the test section from 560 to 8,100.

4.2.1 Laminar Flow

The experimental data for the laminar flow experiments are summarized in Table 4.1 and Table 4.2. Table 4.1 contains the experimental conditions and results when the mixing section is used, and Table 4.2 is for when the mixing section is not used.

Table 4.1 Laminar flow experimental data when the downstream mixing section is used.

Re_D	T_s [°C]	RH [%]		T [°C]		Ra_D	H*	Sh_D	U (Sh_D) [%]
		Upstream	Downstream	Upstream	Downstream				
699	14.5	33.6	45.8	21.9	20.2	40,100	-1.7	5.5	2.9
796	12.5	17.2	30.3	22.3	20.0	55,600	-1.7	5.3	2.6
844	17.4	53.1	60.9	22.4	21.3	17,400	-1.9	4.5	3.8
1303	14.5	35.2	43.3	22.1	20.5	41,600	-1.6	6.1	2.9
1340	13.2	23.0	32.2	22.8	20.7	53,800	-1.5	6.3	2.6
1531	17.2	54.7	60.1	22.0	20.9	16,600	-1.9	5.5	3.8
1583	12.7	19.7	28.1	22.7	20.8	55,500	-1.5	6.3	2.6
1863	13.7	25.4	32.7	23.1	21.5	55,700	-1.5	7.0	2.7
2059	14.4	34.5	40.8	22.3	20.9	45,300	-1.5	7.3	2.9
2077	17.1	54.5	58.8	22.0	21.1	17,400	-1.8	6.0	3.8
2079	12.2	17.9	25.7	22.9	20.8	60,700	-1.4	7.7	2.7

Table 4.2 Laminar flow experimental data when the mixing section is not used.

Re_D	T_S [°C]	RH [%]		T [°C]		Ra_D	H*	Sh_D	U (Sh_D) [%]
		Upstream	Downstream	Upstream	Downstream				
563	15.5	31.2	50.3	22.8	19.0	37,800	-2.1	4.6	3.8
665	18.8	66.8	79.7	21.1	19.3	6,100	-3.6	4.4	6.3
722	21.2	29.0	43.5	32.6	28.4	52,200	-1.6	4.8	3.7
732	12.6	17.7	35.3	22.6	18.3	50,700	-1.6	5.7	3.0
779	21.4	77.6	84.7	23.3	22.3	7,200	-2.9	4.2	13.1
1004	21.3	78.8	84.7	23.0	22.2	6,500	-3.1	4.5	13.2
1047	15.1	30.5	42.6	22.7	20.1	42,400	-1.9	5.5	3.3
1310	22.0	23.5	32.4	36.1	32.8	69,600	-1.5	5.8	3.5
1322	16.5	37.9	47.7	23.4	21.4	37,900	-2.0	5.8	3.7
1404	21.4	79.9	84.4	23.0	22.3	6,300	-3.2	4.8	13.3
1410	18.6	55.4	63.6	23.1	21.8	22,300	-2.1	5.7	5.1
1417	18.9	58.1	65.9	23.1	21.8	20,200	-2.2	5.7	5.3
1486	12.3	17.5	27.5	22.6	19.9	58,500	-1.5	6.9	2.8
1519	21.5	79.4	83.7	23.3	22.7	7,500	-2.8	5.1	13.4
1613	16.2	36.5	45.0	23.4	21.6	42,400	-1.8	6.3	3.6
1806	21.4	79.6	83.3	23.1	22.6	7,700	-2.8	5.4	13.5
1810	17.5	48.3	55.6	23.0	21.7	29,300	-2.0	6.2	4.6
1948	12.1	17.1	25.3	22.6	20.4	62,700	-1.5	7.6	2.8
2010	22.4	21.7	28.2	37.9	35.2	82,500	-1.4	7.0	3.5
2032	21.4	80.6	83.8	23.1	22.7	7,300	-2.9	5.3	13.7
2038	17.2	46.4	53.6	23.1	21.8	34,800	-1.8	7.2	4.2
2052	15.9	37.2	45.1	23.0	21.3	42,300	-1.8	7.6	3.6
2054	18.5	57.2	63.6	23.1	22.0	23,500	-2.0	6.9	5.2
2071	15.7	38.4	46.3	22.9	21.3	40,300	-1.7	7.7	3.6

Figure 4.1 presents the convective mass transfer coefficients, h_m (m/s), for a range of Re_D and inlet air relative humidity. The convective mass transfer coefficient decreases when the relative humidity of the air entering the test section increases. The convective mass transfer coefficient can change as much as 35% when the air relative humidity varies from 18 to 80% RH. Similar results are seen in Figure 4.2, which presents the non-dimensional mass transfer coefficient (Sh_D) as a function of the relative humidity of the air entering the test section.

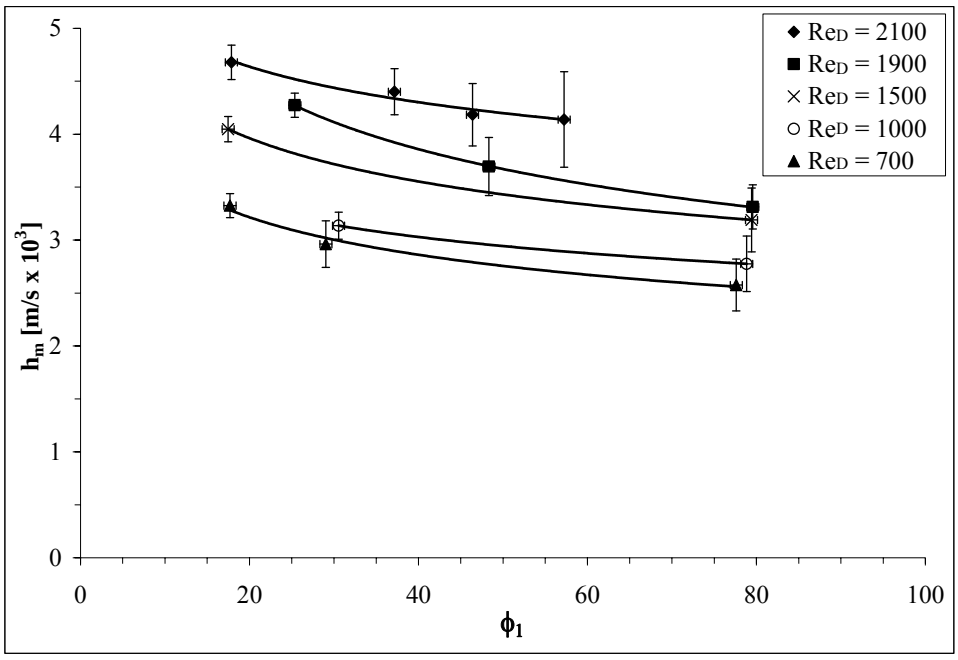

Figure 4.1 Convective mass transfer coefficient (h_m) as a function of Re_D and the relative humidity of the air entering the test section (ϕ_1).

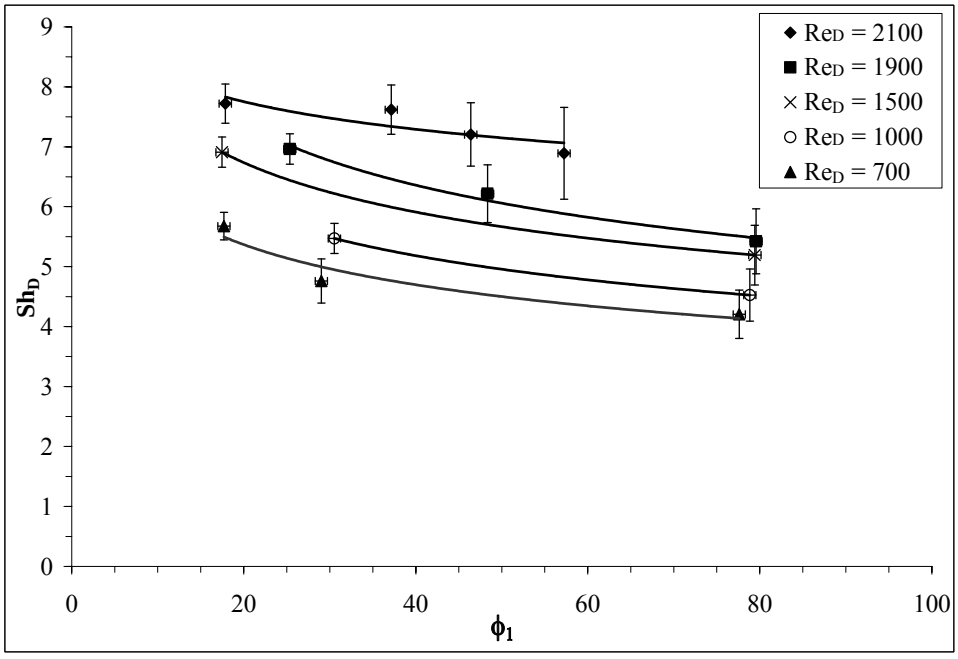

Figure 4.2 Sherwood number as a function of Re_D and the relative humidity of the air entering the test section (ϕ_1).

To fully capture the effects of the relative humidity on the convective mass transfer coefficient, Ra_D (equation (3.6)) and H* (equation (3.17)) are used, which take into account the temperature and relative humidity of the air at the surface of the water and in the bulk airflow. The Sh_D is determined for laminar flow between a Re_D of 560 and 2,100, which corresponds to an X* between 0.037 and 0.011, and Ra_D between 6,100 and 82,500 ($0.003 < Gr_m/Re_D^2 < 0.2$), and is presented in Figure 4.3. Figure 4.3 shows a general trend of increasing Sh_D as Re_D increases (X* decreases), which is expected (Incropera and DeWitt, 2002) since the test section is not long enough for the temperature and concentration boundary layers to become fully developed. The work of Dr. Prabal Talukdar, post doctorial fellow in the research team, simulated the duct geometry and boundary conditions with a computational fluid dynamics (CFD) model. Dr. Talukdar determined that at a Re_D of 2100 and 700 the thermal boundary layer thicknesses are 41% and 70% of the duct height (H = 20.5 mm), and the concentration boundary layer thicknesses are 55% and 76% of the duct height respectively, at the exit of the test section. As Re_D increases, the thermal and concentration boundary layers become thinner and less developed over the surface of the water. A thinner boundary layer results in a larger concentration gradient at the surface of the water, which contributes to an increase in forced convection mass transfer at the surface of the water.

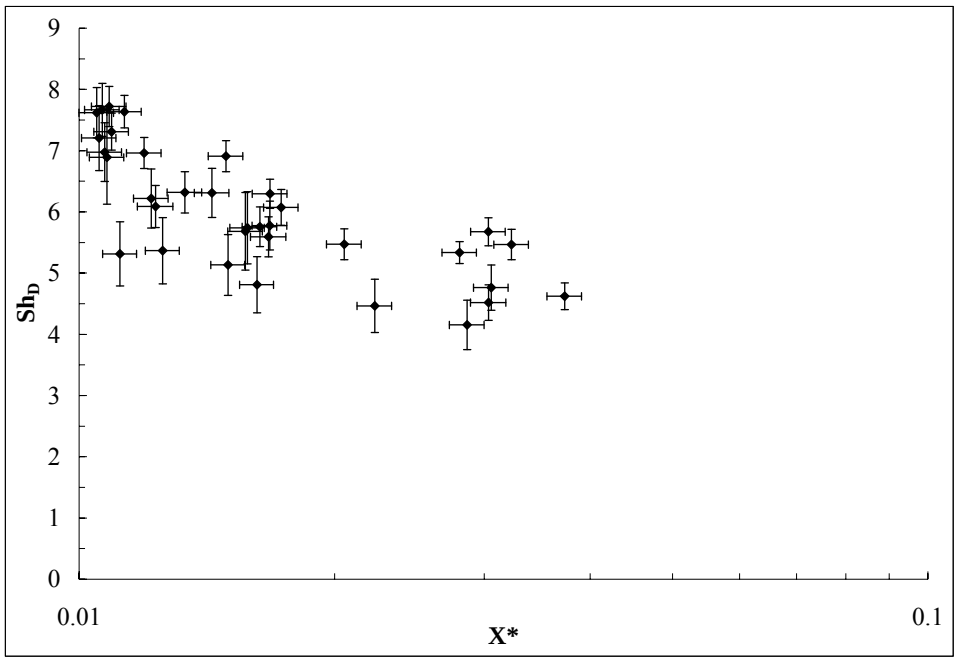

Figure 4.3 Laminar flow results of Sh_D for a range of X* and Rayleigh numbers (Ra_D) for all the experimental tests

Figure 4.3 also shows that there is a large variation in Sh_D and the uncertainty in Sh_D for a given X*. The values of Sh_D range from 4 to 8 and the total uncertainties in Sh_D range from ±3% to ±13% with only 6 (out of 35) values exceeding ±10%. This scatter in Sh_D is a result of each data point having a unique Ra_D associated with it. Since the temperature of the water is not controlled during the experiments, but is dependent on the phase change rate, Ra_D cannot be precisely controlled from one experimental test to the other. To determine if Sh_D is dependent on Ra_D, Figure 4.4 shows four curve fits to data points over a small range of Ra_D. The data points for a range of Ra_D are within ±10% of the average Ra_D for that range.

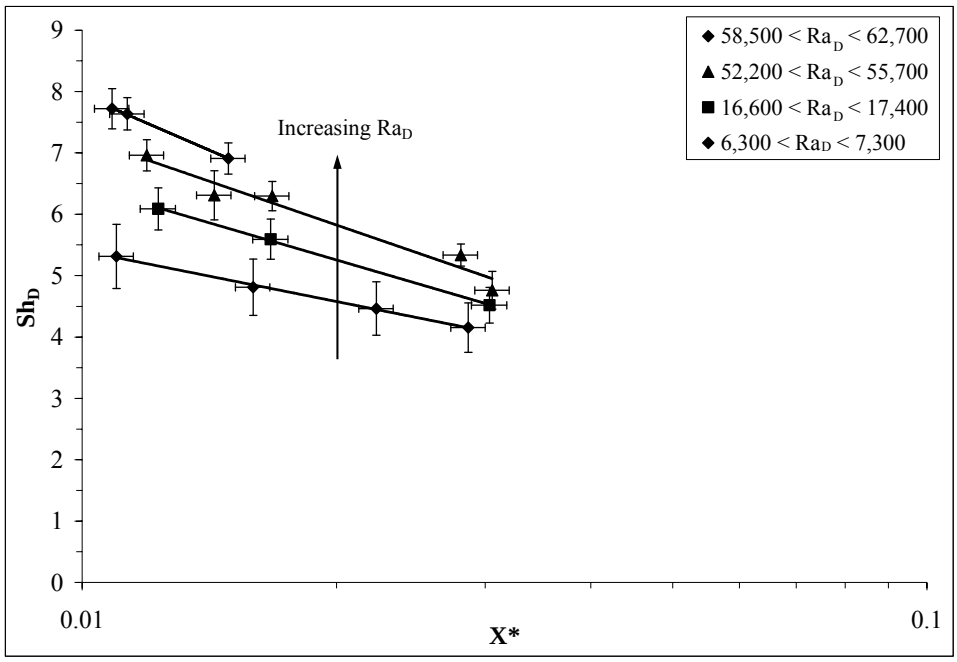

Figure 4.4 Laminar flow results of Sh_D for a range of X* and specific ranges of Rayleigh numbers (Ra_D), where the variation in Ra_D is less than ±10% in each group.

The data in Figure 4.4 show that as Ra_D increases, Sh_D increases and the uncertainty in Sh_D decreases. Ra_D increases as the moist air (air-water vapor mixture) density difference between the bulk airflow and that at the surface of the water increases, as shown in equation (3.6). In this experiment, the density of the moist air at the surface of the water is always larger than that of the bulk airflow, since the water temperature is always less than the bulk airflow temperature, which causes a buoyancy-driven downflow from the air towards the surface of the water (Sparrow et al., 1983). Sparrow et al. (1983) found that this type of downward airflow dominated the evaporation of water from circular pans when the water temperature was less than the ambient air temperature. Other researchers have demonstrated the importance of natural convection heat transfer for thermal developing flow in rectangular ducts. Ou et al. (1974) and Basak et al. (2006) show the secondary flow patterns that result as cooled air flows

down the wall and recirculates in the centre of the duct cavity. A similar flow pattern is expected in this experiment, which may be enhanced by non-uniform conditions in the experiment (Basak et al., 2006).

As the relative humidity of the air delivered to the test section decreases for a constant X*, the temperature at the surface of the water decreases. For the experiments in this thesis, the water temperature is 1-14°C colder than the bulk air temperature, depending on the relative humidity, temperature and Re_D of the airflow. A decrease in the relative humidity of the bulk airflow results in an increase in the vapor concentration difference between the bulk airflow and the surface of the water. Also, a decrease in water temperature causes the moist air (air-water vapor mixture) density difference between the bulk airflow and that at the surface of the water to increase, which results in an increase in Ra_D (equation (3.6)). The effect of the air relative humidity and the temperature of water suggests that evaporation is greater with dry air than with humid air (Huang et al., 2005; Jang et al., 2005), due to the simultaneous increase in the vapor concentration difference and Ra_D. The combined effects of natural convection and the effect of the relative humidity of the airflow on the evaporation process influences the convective mass transfer coefficient and these effects are represented well by Ra_D.

From the experimental data, Sh_D has a dependence on X* and Ra_D. A curve fit to the data shown in Figure 4.3 results in

$$Sh_D = 0.417 \frac{Ra_D^{0.124}}{X^{*0.334}}, \tag{4.1}$$

which is valid for $0.037 < X^* < 0.011$, $6{,}100 < Ra_D < 82{,}500$ and where $r^2 = 0.90$ and 95% of the experimental data fall within ±10.0% of the correlated line.

As noted previously, the temperature and humidity of the air entering the test section influences Ra_D as well as S* (equation (3.16) and H* (equation (3.17)). Therefore, the temperature and humidity of the airflow cannot be neglected for simultaneous heat and moisture transfer. In fact, it is equally possible to correlate Sh_D with H* (or S*). Figure 4.5 shows three curve fits to data points over a small range of H*. The data points for a range of H* are within ±5% of the average H* for that range. It is shown that as H* decreases (becomes more negative) Sh_D also decreases. This type of relationship is shown by Yan (1996), where Sh_D decreases as the energy transport through mass diffusion acts in the opposite direction of that through thermal diffusion (i.e. as $N < 0$ or as $H^* < 0$).

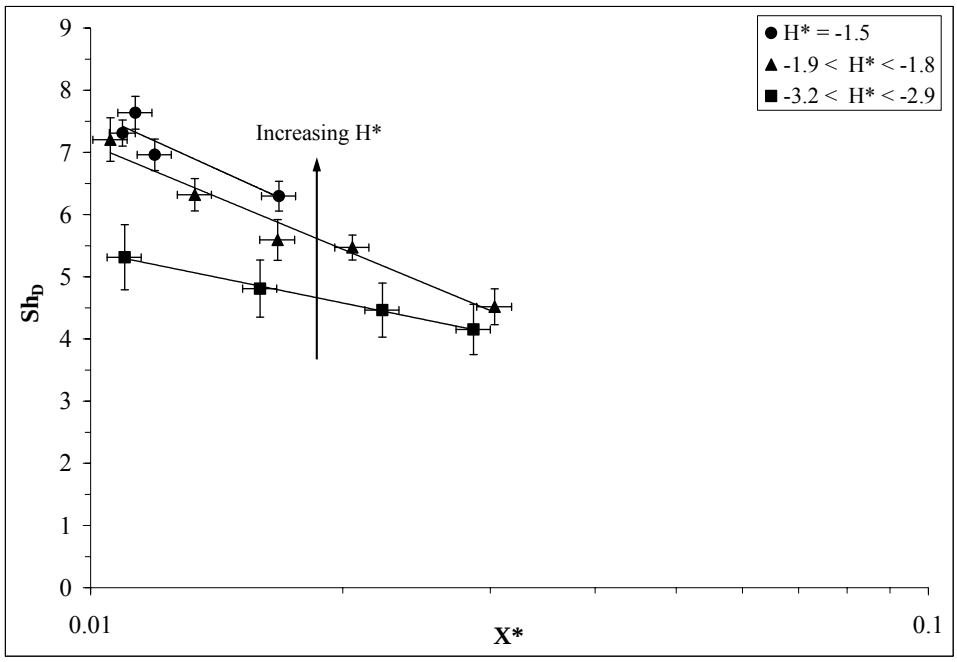

Figure 4.5 Laminar flow results of Sherwood number for a range of X* and specific ranges of H*, where the variation in H* is less than ±5% in each group.

The correlation that results when all the experimental data are used is

$$Sh_D = \frac{2.11}{X^{*\,0.308}\left|H^*\right|^{0.371}} \tag{4.2}$$

which is valid over a range of $-3.6 < H^* < -1.4$ and $0.037 < X^* < 0.011$. The above equation fits the experimental data with an r^2 of 0.89 and 95% of the experimental data falls within ±9.4%. The better fit of equation (4.2) compared to equation (4.1) indicates that H* is equally as good or even possibly a better fitting parameter than Ra_D.

To increase the confidence in the experimental data (Figure 4.3) and the correlation equation (4.1), they are compared with data in the literature in Figure 4.6. Figure 4.6 shows a reasonable agreement between the numerical results of Lin et al. (1992) and the present work. However, Sh_D calculated by Lin et al. (1992) is slightly larger than Sh_D measured in this thesis for the same value of Ra_D. The reason for the higher Sh_D is that

the numerical results were determined for evaporation from heated water rather than cooled water as in the current experiment. The heated water creates an upward natural convection airflow, which results in a greater convective transfer coefficient than in the present study, which has a cooled water surface. This is well known for free convection heat transfer from the top surface of a heated plate (Incropera and DeWitt, 2002) and therefore Figure 4.6 helps confirm the validity of the correlation developed in this thesis (equation 4.1). The effects of H* on Sh_D were not determined by Lin et al. (1992), but have only been quoted as part of the experimental test conditions. In the work of Lin et al. (1992), $H^* > 0$, and in the present work $H^* < 0$. Based on results shown by Yan (1996), the Sherwood number is greater when $H^* > 0$, and this confirms why the work of Lin et al. (1992) produces a Sh_D that is greater than the present work when the Rayleigh numbers are the same. Comparison to correlation equation (4.2) can not be performed since no information in the literature exists to date that uses H* (or even S*) as a fitting parameter for Sh_D and the geometry of the present study.

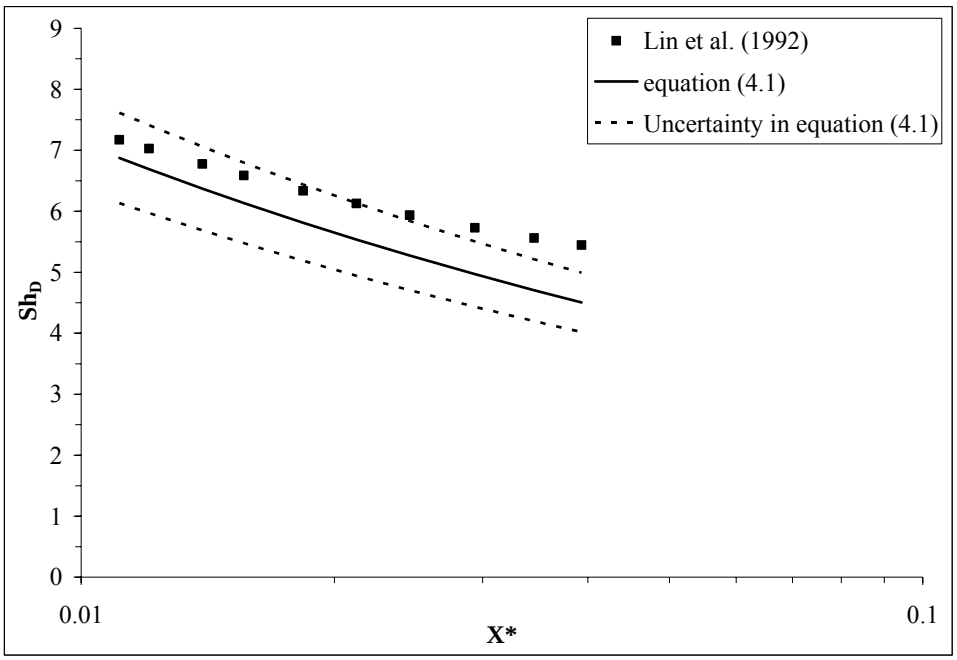

Figure 4.6 Comparison of the Sh_D determined in this thesis with Lin et al. (1992) when Ra_D = 35,300.

Another useful comparison is to compare the measured mass transfer coefficients with heat transfer coefficients from the literature using the analogy between heat and mass transfer with

$$Sh_D = Nu_D \left(\frac{Sc}{Pr} \right)^{1/3} . \tag{4.3}$$

Equation (4.3) is valid when mass transfer rates are low. When mass transfer rates and the bulk fluid motion required to overcome the diffusion of air to the water surface are high, equation (4.3) needs to be corrected (Yan, 1996). For the range of testing conditions in this paper, the maximum correction of equation (4.3) is 1% (Yan, 1996). Since the correction is small, the experiments are considered to be low mass transfer experiments and equation (4.3) is used without any correction.

The study in the literature that most closely represents the current experiment is a numerical study of laminar flow forced convection heat transfer within a heated rectangular duct (Lyczkowski et al., 1981). The flow is hydrodynamically developed and thermally developing, but natural convection is neglected. To compare the results for one heated wall based on the ½ height of the duct, the Nusselt number of Lyczkowski et al. (1981) is converted to a Nusselt number based on the hydraulic diameter by multiplying the former by $4/(1+1/\gamma)$.

A comparison between the predicted mass transfer results of Lyczkowski et al. (1981) and the present study are given in Figure 4.7. It is shown that the results of Lyczkowski et al. (1981) are within the range of measured Sherwood numbers, and compare well at the upper range of Rayleigh numbers. This comparison shows that the work of Lyczkowski et al. (1981) does predict Sh_D within the range of experiment results, but the effects of Ra_D (or even H*) are not accounted for.

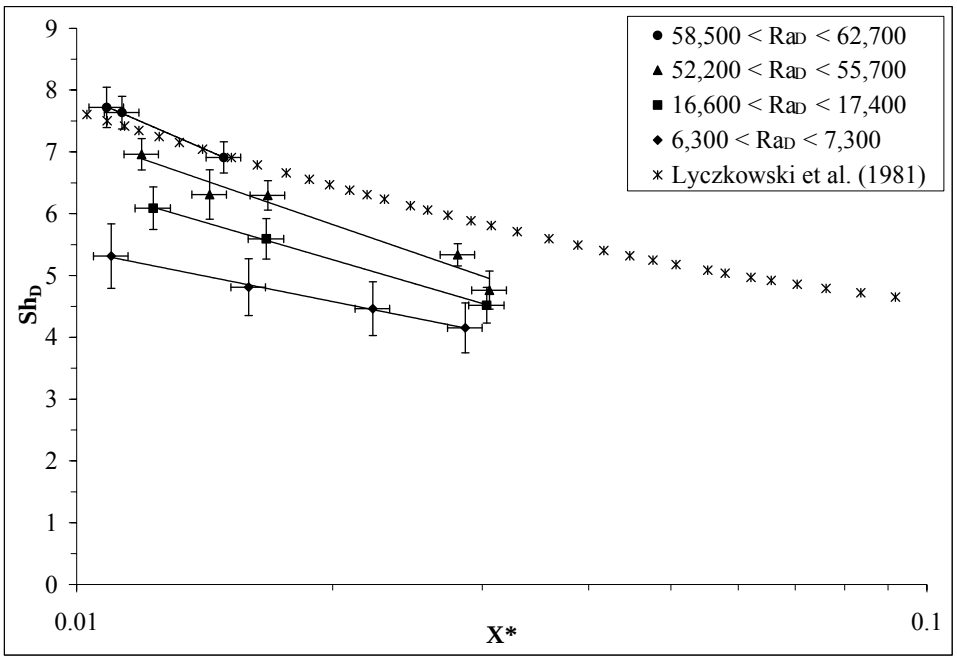

Figure 4.7 Comparison of the Sh_D determined in this thesis with Lyczkowski et al. (1981).

Chen et al. (2002) developed an equation to calculate the mass to heat transfer coefficient ratio (h_m/h_h) for evaporation of a water droplet. The derivation was based on a steady-state heat balance with an equal exchange of sensible and latent heat between a water droplet and an airflow. For an air temperature of 40°C and a range of relative humidities (0 – 50% RH) Chen et al. (2002) determined that h_m/h_h was consistently 14% less than h_m/h_h predicted by equation (4.3) for the same conditions. The differences between the present work and that of Lyczkowski et al. (1981) are a result of using equation (4.3) and neglecting the effects of Ra_D, which can result up to a 30% error in predicting Sh_D.

4.2.2 Turbulent Flow

The experimental data for the turbulent flow experiments are summarized in Table 4.3 and Table 4.4. Table 4.3 contains the experimental conditions and results when the mixing section is used and Table 4.4 is for when the mixing section is not used.

Table 4.3 Turbulent flow data when the downstream mixing section is used.

Re_D	T_s [°C]	RH [%]		T [°C]		Ra_D	H*	Sh_D	U Sh_D [%]
		Upstream	Downstream	Upstream	Downstream				
4295	10.9	16.5	23.5	21.4	19.7	41,200	-1.4	12.9	2.9
4303	10.8	15.3	22.4	21.3	19.4	44,100	-1.4	13.2	2.8
4409	13.3	29.5	35.7	22.0	20.5	35,00	-1.4	12.9	3.2
6321	11.0	16.7	23.3	21.7	19.7	46,400	-1.4	18.5	3.0
6351	13.5	30.1	35.8	22.5	21.0	36,400	-1.4	17.4	3.4
8097	13.8	30.0	35.1	22.8	21.3	37,200	-1.4	20.3	3.5

Table 4.4 Turbulent flow data when the mixing section is not used.

Re_D	T_s [°C]	RH [%]		T [°C]		Ra_D	H*	Sh_D	U Sh_D [%]
		Upstream	Downstream	Upstream	Downstream				
3117	17.7	53.5	59.4	22.8	21.8	28,500	-1.8	9.8	3.7
3193	17.9	59.4	64.8	22.0	21.1	21,100	-2.0	9.3	5.3
5032	18.4	57.2	62.3	23.0	22.1	25,800	-1.9	14.1	3.8
5106	18.1	60.4	65.2	22.1	21.3	21,100	-2.1	13.6	5.1
6968	17.7	51.7	56.7	23.1	22.2	30,800	-1.7	18.3	3.4
6983	17.7	61.3	65.8	21.5	20.8	20,900	-2.0	17.5	5.1
7914	17.2	56.0	60.4	21.7	21.0	26,200	-1.9	18.9	4.5

Turbulent flow experiments are performed in order to develop a relationship for Sh_D that includes both developing flow (X*) and buoyancy forces (Ra_D), and also to further verify the experiments by comparing to experiments in the literature (Chuck and Sparrow, 1987; Chuck, 1985), which are for turbulent flow. The turbulent flow data of the present work cover a range of Re_D between 3,100 and 8,100, and Ra_D between 20,900 and 46,000. The various Ra_D are created by the air relative humidity between

15% RH and 61% RH at a constant air temperature of approximately 23°C. The results in Figure 4.8 show that as Ra_D increases, Sh_D increases. The contribution of natural convection compared to that of forced convection is measured by Gr_m/Re_D^2. This ratio is approximately 20 times less than that for the laminar flow experiments, which suggests that the contribution of natural convection evaporation is smaller in the presence of forced convection turbulent flow than in laminar flow.

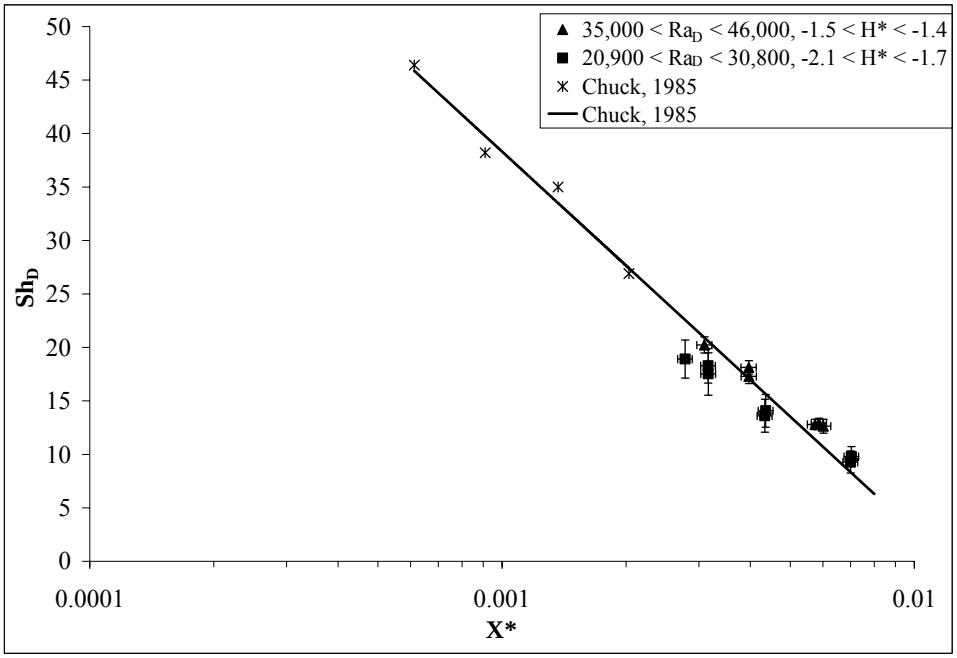

Figure 4.8 Comparison of the Sh_D determined in this thesis with Chuck (1985).

The effects of Ra_D for turbulent flow are correlated with X*, which results in

$$Sh_D = 0.012 \frac{Ra_D^{0.311}}{X^{*0.725}}, \tag{4.4}$$

where $r^2 = 0.98$, and 95% of the data falls within $\pm$ 7.1% of the correlated line.

If H* is correlated with the experimental results,

$$Sh_D = \frac{0.382}{X^{*0.719}|H^*|^{0.494}}, \tag{4.5}$$

which is valid over a range of $-2.1 < H^* < -1.4$. The above equation fits the experimental data with an r^2 of 0.99, and 95% of the experimental data falls within ±3.5%. The curve fit of equation (4.5) has better agreement than equation (4.4), which suggests that for turbulent flow, the operating condition factor (H*) is a better fitting parameter than Ra_D.

Experimental data of Chuck (1985) are shown in Figure 4.8 for test section lengths of 12.5 cm and 27.9 cm at a Re_D of 7,200 and 10,700. Since the data of Chuck (1985) are for step heights (h) ranging from 3.8 mm to 15.2 mm, the experimental results are extrapolated to h = 0 mm for comparison to the present work. Even though the average h in the present work is 0.5 mm, there is no seen effect on Sh_D when neglecting this small height drop of water in the pan. A linear decreasing Sh_D with increasing X* for both studies confirms that the concentration boundary layers within the ducts are not fully developed. A linear curve fit of Chuck (1985) data fits well with the present work, especially for the larger range of Ra_D (35,000 - 46,000). The testing conditions for the larger range of Ra_D occurs when $15\% < \phi_1 < 30\%$, and the testing conditions of Chuck (1985) are within this range.

4.3 Convective Heat Transfer

The following section develops an analogy between heat and mass transfer, which allows the convective heat transfer coefficient to be determined from the measured mass transfer coefficients presented previously (Tables 4.1 to 4.4). The analogy is validated

by comparing its prediction to the convective heat transfer coefficient determined from the measured temperature data.

4.3.1 Convective Heat and Mass Transfer Analogy

Due to the evaporation process, sensible and latent heat are exchanged between the surface of the water and the airflow. The convective heat transfer coefficient is represented by a Nusselt number (Nu_D), which is analogous to the form of the Sherwood number (equation (3.20)).

$$Nu_D = \frac{h_h D_h}{k_f} \quad , \tag{4.6}$$

where h_h is the convective heat transfer coefficient and D_h is the hydraulic diameter of the test section (equation (3.7)). The thermal conductivity (k_f), determined at T_f (equation (3.5)) is the thermal conductivity of dry air because humidity has a small effect (less than 0.2% (ASHRAE Fundamentals, 2005)) for the conditions in this thesis. The dry air thermal conductivity is based on a curve fit to a table of values given in Incropera and DeWitt (2002), over a temperature range of 250 K to 350K.

$$k_f = -6\times10^{-8}T_f^2 + 1.13\times10^{-4}T_f + 2\times10^{-3}, \tag{4.7}$$

which has an r^2 of 1 and can calculate the values given in Incropera and DeWitt (2002) exactly.

When steady-state evaporation within the TMT facility is obtained, the latent energy lost by the liquid water from evaporation must be replenished by energy transfer to the liquid from its surroundings. If radiation effects are neglected, the heat transfer is due to convective heat transfer from the bulk airflow above the water and/or from heat transfer

from the surroundings. If conservation of energy is applied to a control surface on the water surface, an analogy between heat and mass transfer can be obtained based on the sensible heat (q_s) and any external heat (q_e) transfer being equal to the latent heat (q_l) transfer.

$$q_s + q_e = q_l, \tag{4.8}$$

where,

$$q_s = h_h A_s \Delta T_{lm}, \tag{4.9}$$

$$\Delta T_{lm} = \frac{(T_2 - T_s) - (T_1 - T_s)}{\ln[(T_2 - T_s)/(T_1 - T_s)]} \tag{4.10}$$

and

$$q_l = h_m A_s \Delta \rho_v h_{fg}. \tag{4.11}$$

The enthalpy of vaporization (h_{fg}) (J/kg) is based on the temperature of the surface of the water (T_s), and is determined from a curve fit to data given in ASHRAE Fundamentals (2005) over a temperature range of 283 K to 298 K.

$$h_{fg} = 2363 T_s + 3146 \times 10^3, \tag{4.12}$$

which has an r^2 of 1.000 and is within ±0.01% of the values given in ASHRAE Fundamentals (2005). Substituting equations (4.9) and (4.11) into equation (4.8), and solving for the convective heat transfer coefficient gives

$$h_h = h_m \left(\frac{\Delta \rho_v h_{fg}}{\Delta T_{lm}} \right) - q_e \left(\frac{1}{\Delta T_{lm} A_s} \right). \tag{4.13}$$

Substituting equations (3.20) and (4.6) into equation (4.13) yields,

$$Nu_D = Sh_D \left(\frac{D_{AB}}{k_f} \right) \left(\frac{\Delta \rho_v h_{fg}}{\Delta T_{lm}} \right) - q_e \left(\frac{D_h}{\Delta T_{lm} A_s k_f} \right), \tag{4.14}$$

which can be rearranged to give

$$Nu_D = Sh_D\left(\frac{Pr}{Sc}\right)\left(\frac{\Delta W_{lm} h_{fg}}{\Delta T_{lm} C_{p,f}}\right) - q_e\left(\frac{D_h}{\Delta T_{lm} A_s k_f}\right), \tag{4.15}$$

where,

$$Sc = \frac{\nu_f}{D_{AB}}, \tag{4.16}$$

$$Pr = \frac{\nu_f}{\alpha_f}, \tag{4.17}$$

$$\alpha_f = \frac{k_f}{\bar{\rho}_g C_{p,f}}, \tag{4.18}$$

and

$$\Delta W_{lm} = \frac{\Delta \rho_v}{\bar{\rho}_g}. \tag{4.19}$$

The specific heat capacity ($C_{p,f}$) is a sum of the partial specific heat capacities of dry air and water vapor.

$$C_{p,f} = (1 - W_f)1007 + W_f\left(0.0086T_f^2 - 4.3T_f + 2382\right), \tag{4.20}$$

where W_f is the average humidty ratio between the surface of the water and the bulk airflow. The specific heat capacity of dry air (1007 J/kg K) in equation (4.20) is constant since temperature has a small effect on it for the conditions in the experiment. The specific heat capacity of moist air (the second term in equation (4.20)) is based on a curve fit to data given in Incopera and Dewitt (2002), which has an r^2 of 0.9999 and fits the data within ±0.3% for a temperature range between 280 K and 300K.

Equation (4.15) is a relationship between heat and mass transfer that enables the determination of Nu_D based on Sh_D and the operating conditions of the experiment. If the test section of the TMT facility is assumed to be perfectly insulated, then no external heat addition from the environment to the surface of the water occurs. If this assumption is applied, equation (4.15) reduces to,

$$Nu_D = Sh_D\left(\frac{Pr}{Sc}\right)\left(\frac{\Delta W_{lm} h_{fg}}{\Delta T_{lm} C_{p,f}}\right). \tag{4.21}$$

Equation (4.21) is similar to the well known analogy between heat and mass transfer given by equation (4.3). The difference between the two equations is that equation (4.21) includes an extra term that represents the energy transport through mass diffusion relative to that through thermal diffusion. Also, the exponent n does not appear in equation (4.21) as it does in equation (4.3) since the Lewis analogy (Incropera and DeWitt, 2002) is not required in the derivation of equation (4.21).

When substituting equation (4.19) into equation (4.14), and assuming there is no external heat transfer (q_e),

$$Nu_D = Sh_D S^*_{lm}. \tag{4.22}$$

Equation (3.16) is used to calculate S^*_{lm}, where the humidity ratio difference (ΔW) and temperature difference (ΔT) are substituted for ΔW_{lm} and ΔT_{lm}. Equation (4.22) shows that Nu_D depends on both Sh_D and S^*_{lm}. In section 4.2, H* is used as a fitting parameter for the experimental data. H* is not used in this case, since the difference between

S_{lm}^{*} and H* is approximately ±15%, since H* assumes constant properties (2500) and S_{lm}^{*} does not.

4.3.2 Convective Heat Transfer Coefficient

Figures 4.9 and 4.10 compare Nu_D calculated by the analogy (equation 4.22) and Nu_D determined by measuring the heat transfer (latent and sensible) within the test section. The sensible heat transfer is calculated based on the temperature difference between the airflow upstream and downstream of the test section as follows:

$$q_s = \dot{m} C_p \left(T_2 - T_1\right). \tag{4.23}$$

The latent heat transfer is calculated based on the heat of phase change due to the evaporation of the water as follows:

$$q_l = \dot{m}_{evap} h_{fg}. \tag{4.24}$$

Figures 4.9 and 4.10 include only data measured when the mixing section is installed downstream of the test section and are plotted as a function of X_h^*. X_h^* is similar to X* (equation 3.15) except Sc is replaced with Pr in equation (3.l5) for heat transfer. Figure 4.9 compares Nu_D determined from the three different methods for laminar and turbulent flow and includes the 95% uncertainty error bars. The uncertainty in the Nu_D determined from the sensible heat transfer (equation 4.23) is larger than the Nu_D with the other two methods since the uncertainty is highly dependant on the small temperature difference in the bulk airflow (typically 1 – 2.5°C) across the test section.

(a)

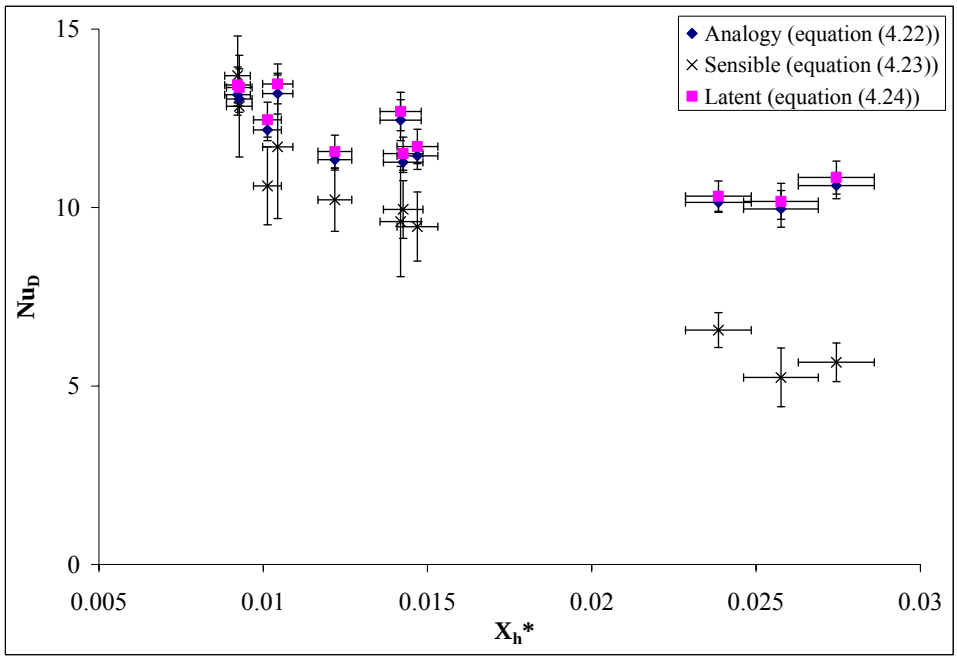

(b)

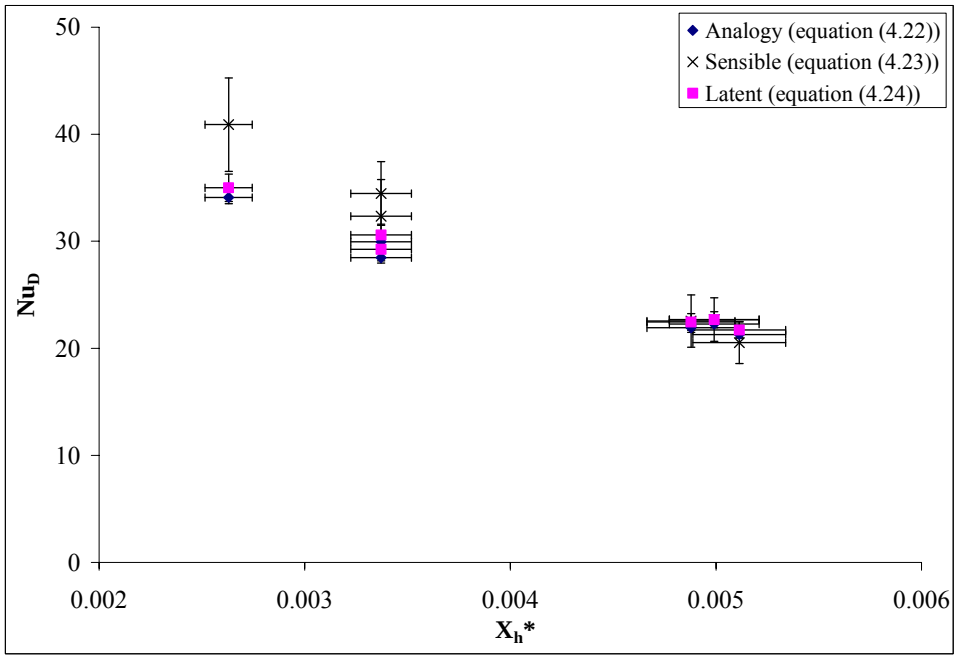

Figure 4.9 Graphs showing Nu_D calculated from the heat and mass transfer analogy equation (4.22) and the measured sensible and latent heat transfers when the mixing section is used for (a) laminar flow and (b) turbulent flow.

It is shown that the Nu_D determined from the latent heat transfer compares to the analogy within the uncertainty bounds. In Figure 4.9(a), the sensible Nu_D is consistently less than the analogy prediction, and only compares within uncertainty at smaller values of X_h^*. As X_h^* increases, the difference between the sensible Nu_D and the analogy increases. This can be seen more clearly in Figure 4.10, which presents the percentage difference of the sensible and latent Nu_D to the Nu_D determined from the analogy for a range of X_h^*.

It is suspected that the sensible Nu_D does not compare in all cases with the analogy due to external heat transfer (q_e) from the ambient. Equation (4.15) shows that Nu_D decreases with the addition of external heat transfer into the water surface. As Re_D decreases (X* increases), the convective heat transfer between the airflow and the surface of the water decreases, and any external heat transfer would have a larger effect on the sensible Nu_D.

(a)

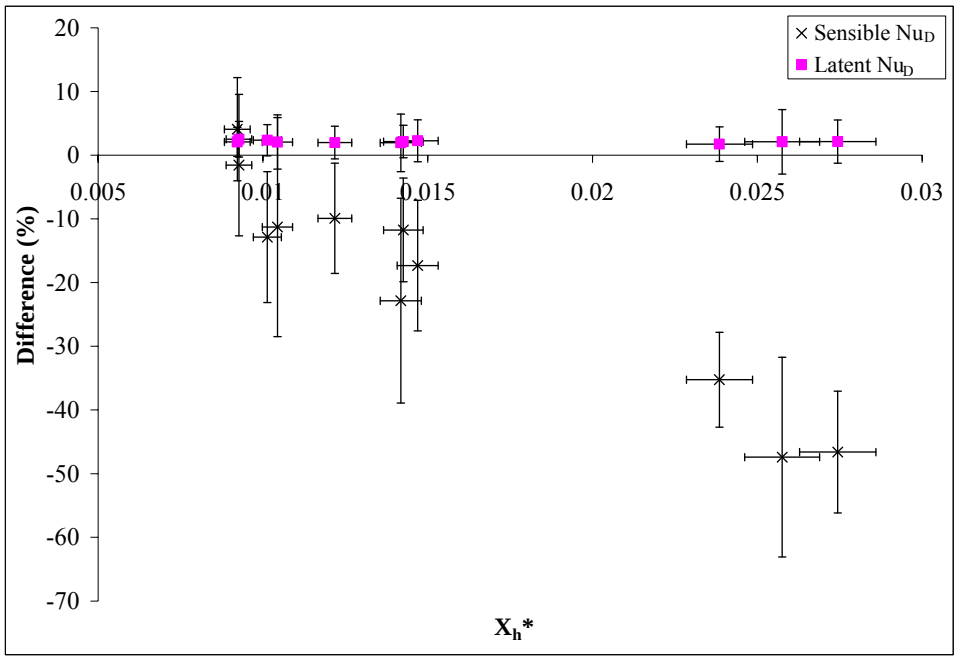

(b)

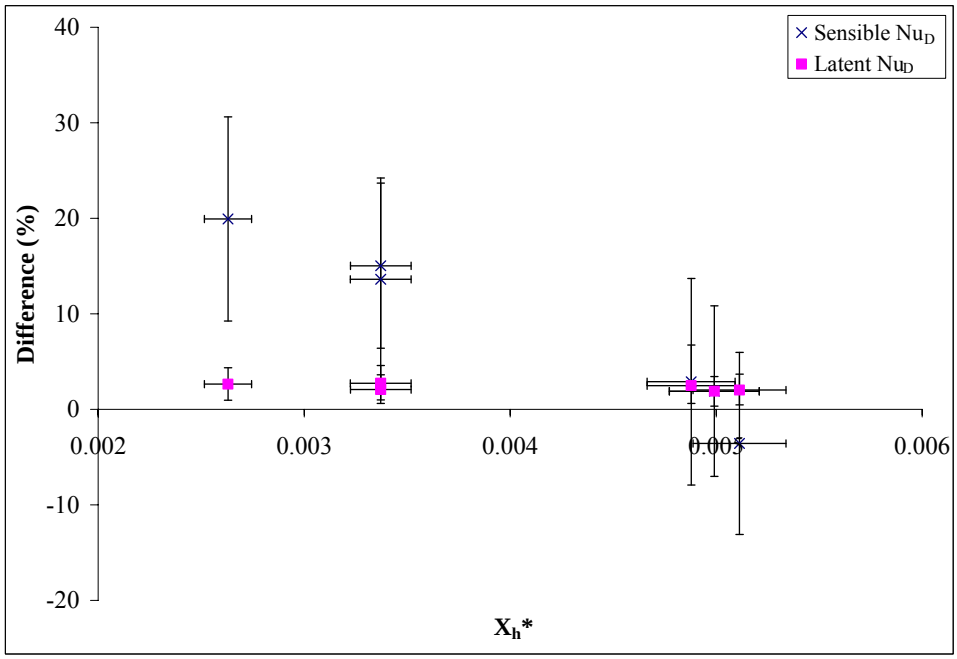

Figure 4.10 Graphs showing the percentage difference between Nu_D using equation (4.22) and Nu_D determined from sensible and latent heat transfers when the mixing section is used for (a) laminar flow and (b) turbulent flow.

Figure 4.11 compares Nu_D calculated by the analogy (equation 4.22) and Nu_D determined by measuring the heat transfer (latent and sensible) within the test section for laminar and turbulent flow, when the mixing section is not used. Nu_D agrees within the uncertainty bounds for all the latent and sensible heat transfer cases. The sensible Nu_D in Figure 4.11 agrees better than in Figures 4.9 and 4.10, since conservation equations for heat and mass are used to calculate the downstream temperature and relative humidity of the airflow. By doing this, it is assumed that the test section is perfectly insulated, and there is no external heat transfer.

(a)

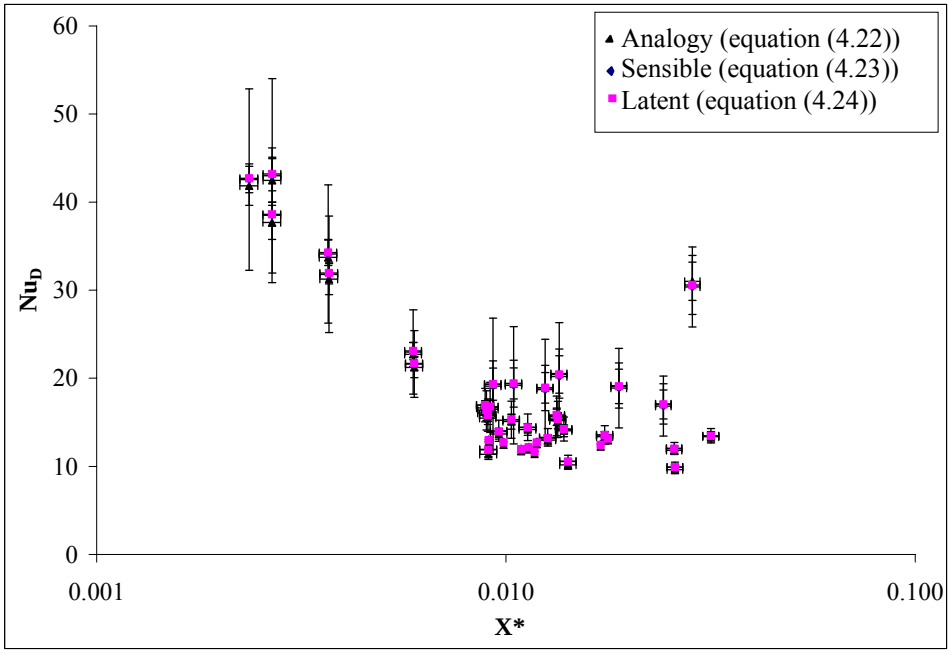

(b)

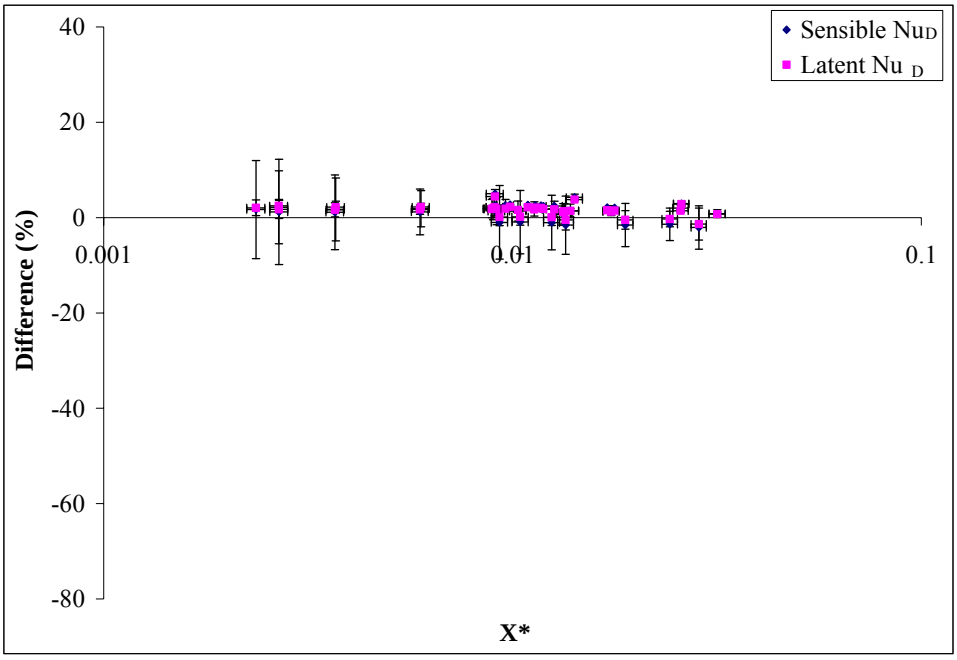

Figure 4.11 Graphs showing (a) Nu_D calculated from the heat and mass transfer analogy equation (4.22) and the measured sensible and latent heat transfer (b) the percentage difference between Nu_D using equation (4.22) and Nu_D determined from sensible and latent heat transfers for when the mixing section is not used.

Figures 4.9, 4.10 and 4.11 show that the convective heat transfer coefficient is dependent on the heat exchange between the bulk airflow and the surface of water, and any external heat transfer to the water surface. Lin et al. (1992) shows the same effect for a heated water surface. The values of S* in the work of Lin et al. (1992) were always positive and larger than unity since an external heat source heated the water surface above the temperature of the bulk airflow. The analysis of Lin et al. (1992) shows that the sensible Nu_D was always less than the latent Nu_D when the water surface was heated. Based on the work of Lin et al. (1992), it is feasible to assume that the test section of the TMT facility is not perfectly insulated, and external heat transfer causes the water surface temperature to be higher than if it were perfectly insulated. In some tests the heat transfer is negligible and in other tests it is not.

4.3.3 Convective Heat Transfer Validity

Equation (4.21) reduces to the approximate form of equation (4.3) when the energy transport through mass diffusion is equal to that through thermal diffusion.

$$Nu_D = Sh_D\left(\frac{Pr}{Sc}\right) \tag{4.25}$$

when

$$\frac{\Delta W_{lm} h_{fg}}{\Delta T_{lm} C_{p,f}} = 1 \tag{4.26}$$

in equation (4.21). Equation (4.26) occurs when the enthalpy of the air remains constant as the water is evaporated in the test section. Figure 4.12 shows a constant enthalpy process on a psychrometric chart for evaporation of water vapor into air. If air enters the test section at conditions A, sensible and latent heat is exchanged such that the conditions of the air move along a line of constant enthalpy (from A to B) as the airflow

moves through the test section. If the air becomes saturated with water vapor, the conditions of the airflow and that at the surface of the water (C) become equal. For a line of constant enthalpy (Figure 4.12), the ratio of $\Delta W_{lm}/\Delta T_{lm}$ is approximately 0.4, and equation (4.26) is approximately 1.

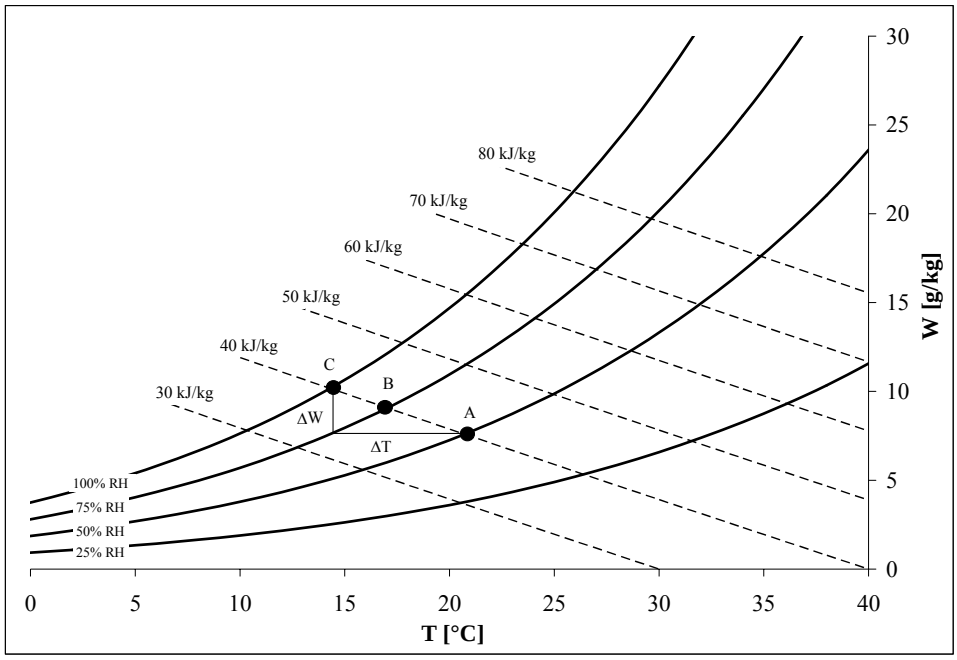

Figure 4.12 Psychrometric chart showing constant lines of enthalpy for evaporation of water into air.

Since equation (4.26) is not equal to 1 for the experimental conditions in this thesis, it is concluded that there is some external heat transfer in the experiment. When there is heat gain from the surroundings, the temperature of points B and C would increase, resulting in an increase in $\Delta W_{lm}/\Delta T_{lm}$, and consequently an increase in S^*_{lm} ($S^*_{lm} > 1$), which is seen in the experiments.

Equation (4.25) differs from equation (4.3) in that it does not include exponent n. The exponent has a small but noticeable effect on the result. The Sh_D predicted by equation

(4.25) is approximately 10% less than that predicted by equation (4.3) for the testing conditions in this thesis. Chen et al. (2002) also found a similar 10% effect for the evaporation of a thin layer of water.

Equation (4.22) is an analogy between heat and mass transfer that can determine either the convective heat or mass transfer coefficient from knowledge of the other coefficient and the operating conditions. Equation (4.22) is valid when simultaneous heat and mass transfer are occurring, since it is derived on this principle. This validity is tested when equation (4.22) is used to convert Nu_D given by Lyczkowski et al. (1981) into Sh_D for the range of S^*_{lm} measured in this thesis. Sh_D given in this thesis and Sh_D from the conversion differ between 30% and 50% over the range of S^*_{lm} (1.5 to 3.0). This difference is larger than the (30%) seen in Figure 4.7, indicating that the traditional analogy (equation (4.3)) is more applicable in this case. Therefore, equation (4.22) can not correctly convert the Nu_D results of Lyczkowski et al. (1981) into the Sh_D found in this thesis, since the convective heat transfer coefficient of Lyczkowski et al. (1981) was determined when mass transfer was not present. On the other hand, the Nu_D measured in this thesis are approximately 65% different than those of Lyczkowski et al. (1981) because of the simultaneous heat and mass transfer.

4.3.4 Nu_D and Sh_D for Simultaneous Heat and Mass Transfer

In section 4.2.1, the traditional analogy between heat and mass transfer (equation (4.3)) is used to convert Nu_D of Lyczkowski et al. (1981) into Sh_D, where equation (4.3) is repeated below for convenience (subscript D is neglected to show the analogy in a more generic form).

$$\mathrm{Sh} = \mathrm{Nu}\left(\frac{\mathrm{Sc}}{\mathrm{Pr}}\right)^{1/3} \tag{4.27}$$

The Sh_D of Lyczkowski et al. (1981) are up to 30% different than the Sh_D measured in this thesis. The large differences are due to the inability of equation (4.27) to correctly account for the simultaneous heat and mass transfer experimental conditions in this thesis. Therefore, a new method is needed to improve the Nu_D of Lyczkowski et al. (1981) (which is determined under heat transfer alone with no mass transfer) with the Sh_D measured in this thesis under simultaneous heat and mass transfer conditions.

The method described in this section will enable the conversion of a Nusselt number determined from a pure heat transfer analysis (Nu_h), i.e. heat transfer alone with no mass transfer as studied by Lyczkowski et al. (1981) for example, into a Sherwood number that is valid for simultaneous heat and mass transfer ($Sh_{h/m}$) as studied in this thesis. In addition to the traditional analogy between heat and mass transfer (equation (4.27)), the method makes use of correlation equation (4.2), which is repeated below.

$$\mathrm{Sh}_D = \frac{2.11}{X^{*\,0.308}\left|H^*\right|^{0.371}} \tag{4.28}$$

Equation (4.28) is for laminar flow and simultaneous heat and mass transfer and gives the functional relationship between $Sh_{h/m}$ and H*:

$$\mathrm{Sh}_{h/m} = f\left(\frac{1}{\left|H^*\right|^{0.371}}\right). \tag{4.29}$$

Equation (4.29) shows that Sh for simultaneous heat and mass transfer conditions ($Sh_{h/m}$) is inversely proportional to H* and this relationship is needed to convert Nu_h into $Sh_{h/m}$ as described in the following steps:

1. Convert a Nu_h into a Sh_m with the traditional analogy between heat and mass transfer (equation (4.27)).

For example, step 1 is shown in Section 4.2.1 and presented in Figure 4.7 for Lyczkowski et al. (1981). When using the traditional analogy, the resultant Sh is valid for pure mass transfer (Sh_m) (i.e., mass transfer in the absence of heat transfer) since Nu_h includes heat transfer only.

2. Convert the pure mass transfer Sh (Sh_m) into a Sh that is valid for simultaneous heat and mass transfer ($Sh_{h/m}$), by using the functional relationship given by equation (4.29). The resulting equation is

$$Sh_{h/m} = \frac{Sh_m}{|H^*|^{0.371}}, \tag{4.30}$$

where $Sh_{h/m}$ and Sh_m represent a Sherwood number based on simultaneous heat and mass transfer and for pure mass transfer, respectively.

To test the validity of the new method, the $Nu_{D,h}$ of Lyczkowski et al. (1981) are converted into a $Sh_{D,h/m}$. A comparison of Lyczkowski et al. (1981) $Sh_{D,h/m}$ based on equation (4.30) to the experimentally determined Sh_D (determined from correlation equation (4.28)) are shown in Figure 4.13. Figure 4.13 shows the predicted $Sh_{D,h/m}$ at the minimum and maximum H* for the test conditions in this thesis. The 95% uncertainty bounds in $Sh_{D,h/m}$ determined with correlation equation (4.28) are ±9.4% (determined in section 4.2.1), which are shown with error bars in Figure 4.13.

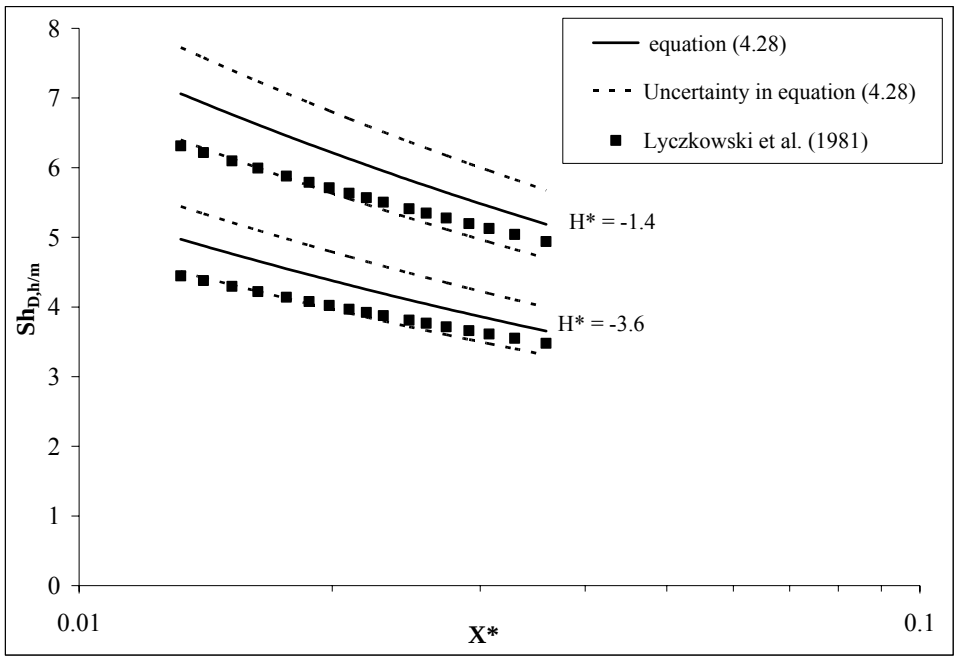

Figure 4.13 Comparison of the Sh_D correlation developed in this thesis for simultaneous heat and mass transfer and the $Sh_{D,h/m}$ obtained from the Nu_D data of Lyczkowski et al. (1981) using the new method (equation (4.30)) over a range of H*.

Figure 4.13 shows that the $Sh_{D,h/m}$ measured in this thesis and that of Lyczkowski et al. (1981) compare within experimental uncertainty (an improvement over the 30% difference shown in Figure 4.7) when the effects of H* are accounted for. Figure 4.13 shows the analogy between heat and mass transfer (equation (4.27)) and the effects of H* should be used to convert a pure heat transfer Nu to Sh for simultaneous heat and mass transfer.

It is also possible to convert a pure heat transfer Nu (Nu_h) into a Nu that is based on simultaneous heat and mass transfer ($Nu_{h/m}$). This is shown by converting the Nu_D of Lyczkowski et al. (1981) with equation (4.30) and the analogy between heat and mass transfer that is developed in this thesis (equation (4.22)). When substituting equation (4.30) into equation (4.22), the resultant Nu equation becomes

$$Nu_{h/m} = \frac{Sh_m}{|H^*|^{0.371}} S^*_{lm} . \quad (4.31)$$

Equation (4.31) is simplified by substituting in H* for S^*_{lm}. It is determined that for the experimental conditions in this thesis

$$S^*_{lm} = 1.18|H^*|, \quad (4.32)$$

which is able to predict the measured S^*_{lm} within ±4% over the range of H* in this thesis. When equation (4.32) is substituted into equation (4.31), the resulting equation is

$$Nu_{h/m} = 1.18 Sh_m |H^*|^{0.671} . \quad (4.33)$$

Figure 4.14 shows the original Nu_D of Lyczkowski et al. (1981) and the $Nu_{Dh/m}$ that has been calculated with equation (4.33) (at H* of –1.4 and –1.9). The original Nu_D of Lyczkowski et al. (1981) is consistently less than the $Nu_{Dm/h}$ determined in this thesis. When the effects of H* are considered, an improvement in the comparison between the Nusselt number of Lyczkowski et al. (1981) and the present study is achieved.

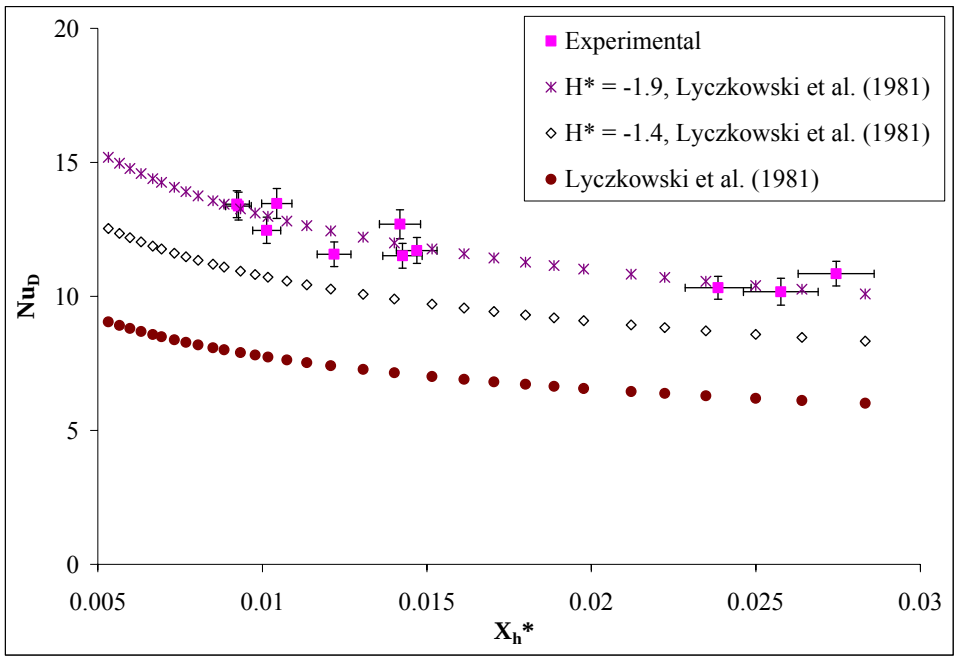

Figure 4.14 Comparison of Nu_D of Lyczkowski et al. (1981) using equation (4.33), the original Nu_D of Lyczkowski et al. (1981) and Nu_D measured in this thesis over a range of H*.

The work in this thesis has shown that a modified method is able to convert a pure heat transfer Nu ($Nu_{h/m}$) from the literature into a Nu and Sh for simultaneous heat and mass transfer by accounting for H*. Equation (4.30) and equation (4.33) provide an alternative method to using the traditional analogy between heat and mass transfer (equation (4.27)) when converting between heat and mass transfer coefficients for simultaneous heat and mass transfer conditions.

4.4 Summary of Equations

The following is a list of equations that have been developed in Chapter 4. The equations are valid over the range of conditions that they have been derived from.

For laminar flow:

$$Sh_D = 0.417 \frac{Ra_D^{0.124}}{X^{*0.334}} \quad (4.1)$$

$$Sh_D = \frac{2.11}{X^{*0.308}|H^*|^{0.371}} \quad (4.2)$$

$$Sh_{h/m} = \frac{Sh_m}{|H^*|^{0.371}} \quad (4.30)$$

$$Nu_{h/m} = 1.18 Sh_m |H^*|^{0.671} \quad (4.33)$$

These equations are valid over the range of:

$560 < Re_D < 2{,}100$

$0.011 < X^* < 0.037$

$6{,}100 < Ra_D < 82{,}500$

$-3.6 < H^* < -1.4$

For turbulent flow:

$$Sh_D = 0.012 \frac{Ra_D^{0.311}}{X^{*0.725}} \quad (4.4)$$

$$Sh_D = \frac{0.382}{X^{*0.719}|H^*|^{0.494}} \quad (4.5)$$

These equations are valid over the range of:

$3{,}100 < Re_D < 8{,}100$

$0.003 < X^* < 0.007$

$20{,}900 < Ra_D < 46{,}000$

$-2.1 < H^* < -1.4$

Analogy between heat and mass transfer:

$$Nu_D = Sh_D S_{lm}^* \quad (4.22)$$

This equation is valid for laminar and turbulent flow where the latent heat exchange is equal to the sensible heat exchange.

CHAPTER 5

CONVECTIVE MASS TRANSFER WITH A PERMEABLE MEMBRANE

5.1 Introduction

This chapter presents experimental measurements and numerical modeling of the moisture transfer through a vapor permeable membrane in the TMT facility. The results of the numerical model are compared to the experiment to determine the accuracy of the model.

5.2 Experiment

The main purpose of the TMT facility is to perform experiments on a variety of building materials (plywood, insulation and gypsum have been tested by Osanyintola 2005, Olutimayin 2004, and Talukdar and Simonson 2006) to determine their water vapor transfer properties. In this chapter, a water vapor permeable membrane (Tyvek®) is experimentally tested to gain an understanding of its moisture transfer characteristics for potential use in a panel-type enthalpy exchanger. An enthalpy exchanger is able to transfer sensible as well as latent heat between two fluids. The membrane would be used as the skin of the exchanger allowing heat and water vapor transfer between air and the fluid within the exchanger. Tyvek® is a permeable membrane that is made from a polyethylene sheet of ultra-fine fibers made from high density polyethylene. Tyvek® is formed by spinning the fibers and then bonding them into a sheet with heat and pressure.

5.2.1 Experimental Setup

The experiments measure the water vapor transfer across a Tyvek® membrane that is subjected to known boundary conditions at the surface of the material. The experiments are conducted within the rectangular test section of the TMT facility, which is described in Chapter 2. The experimental setup is similar to the description given in Chapter 2, where a pan of water is situated in the bottom panel of the rectangular test section. The only difference in the setup of the experiment in this chapter is that the membrane is attached to the top surface of the water pan (Figure 5.1).

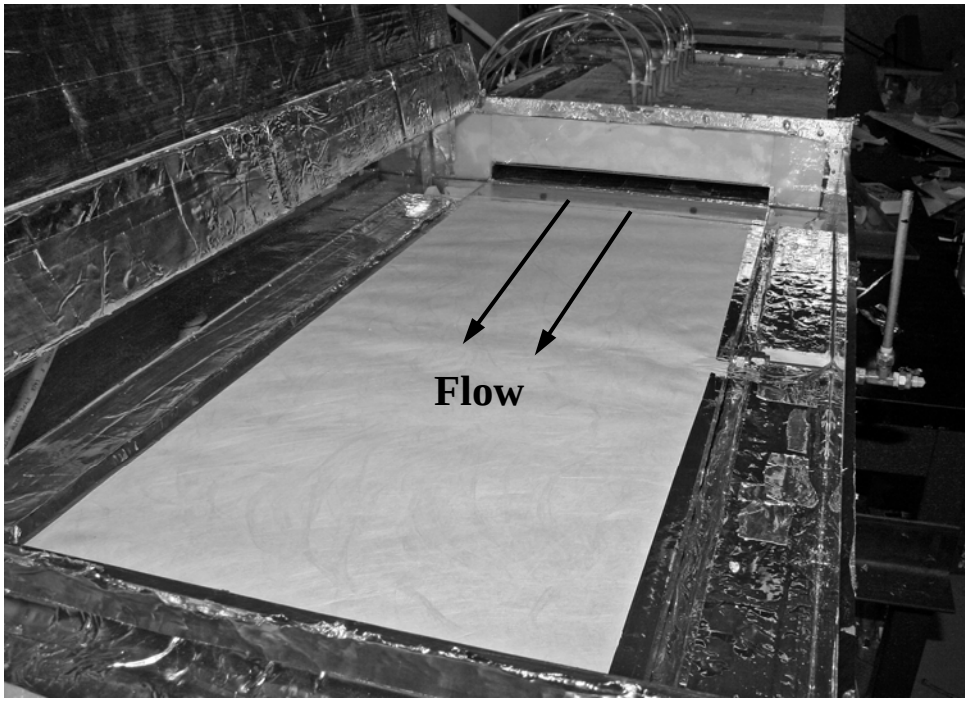

Figure 5.1 Tyvek® membrane attached to the top surface of the pan of water.

Six T-Type thermocouples are used to measure the water temperature at the surface of the membrane. The thermocouple leads (5 mm before the thermocouple tip) are attached to the underside of the membrane with the use of a waterproof adhesive. The thermocouple tips are then bent to provide contact with the underside of the membrane.

The thermocouple leads exit out of the container between the membrane and the top of the pan. The membrane is glued to the top surface of the pan with a waterproof adhesive, and is stretched across the pan to create a smooth and taught surface. Aluminum foil tape is used as a precautionary measure to seal the edges of the pan to prevent water leaking between the membrane and the edge of the pan. The water is poured into a copper pipe elbow that is tapped into the side of the pan to enable the filling of the pan with water. The pan of water is filled until the water surface touches the underside of the membrane.

Four experimental tests are performed at a Re_D of 940, 2000, 5140, and 5240 where the air entering the test section is approximately 30% RH and 22°C for each trial. The experiment is repeated in the turbulent flow regime (Re_D ~ 5200) to check if the measured moisture transfer rates are similar between the two tests. The operating procedure is similar to the experiments presented in Chapter 2. Experimental data are recorded once the air temperature, relative humidity and mass flow rate and the water temperature are viewed to be constant, as explained in Section (3.2). The water in the pan is continuously refilled until the temperature of the surface of the water is viewed to be constant. Once the air and water conditions are at steady state, the experiment is conducted for approximately 8 hours, and the data are averaged over this time.

5.2.2 Experimental Results

Table 5.1 presents the average experimental conditions over the testing time for four trials performed on the Tyvek® membrane.

Table 5.1 The test conditions and mass transfer rate for the Tyvek® experiments.

Trial	Re_D	T_s (°C)	RH [%]		T [°C]		$\dot{m}_{evap}$ [g/hr]
			Upstream	Downstream	Upstream	Downstream	
1	940	17.4	29.0	37.0	22.2	21.9	8.6
2	2000	17.6	30.5	35.7	21.6	21.2	10.8
3	5140	18.7	31.3	35.2	21.5	21.4	14.4
4	5240	18.7	30.7	35.4	21.6	21.5	14.0

5.2.3 Material Properties

Although the material properties are not needed for the experiment on the Tyvek® membrane within the TMT facility, property data are needed for the numerical model. In this section the sorption isotherm curve is measured for Tyvek®, as well as other properties determined from the literature.

The sorption isotherm represents the changes in the moisture content of a material as a function of the relative humidity at constant temperature. It describes the ability of a hygroscopic material to absorb or release water vapor from or into air. The moisture content of the material is the mass of the material's water content divided by the dry mass of the material.

The experiment to generate the sorption isotherm is performed according to ISO 12571 (1996) using salt solutions to generate the relative humidity (ASTM E104, 1985). Four Tyvek® samples are cut into 50-mm-wide by 316-mm-long strips. The samples are placed into individual perforated cups and the samples are dried in a sealed jar containing calcium sulphate. The dried samples are weighed and then placed in separate jars above a salt solution. The samples are first placed in a jar at 11% RH until equilibrium is reached. The mass of each sample is weighed, and then the specimens are

placed in a jar with a relative humidity of 33%. This process is then repeated at a relative humidity of 53 and 94%. Only the adsorption isotherm is measured.

The moisture content (u) at a given relative humidity is calculated as

$$u = \frac{m - m_{dry}}{m_{dry}} \tag{5.1}$$

where m is the final mass of the Tyvek® membrane after equilibrium is reached between the membrane and the air in the jar. m_{dry} is the mass of dry Tyvek®. The sorption isotherm curve for Tyvek® is shown in Figure 5.2.

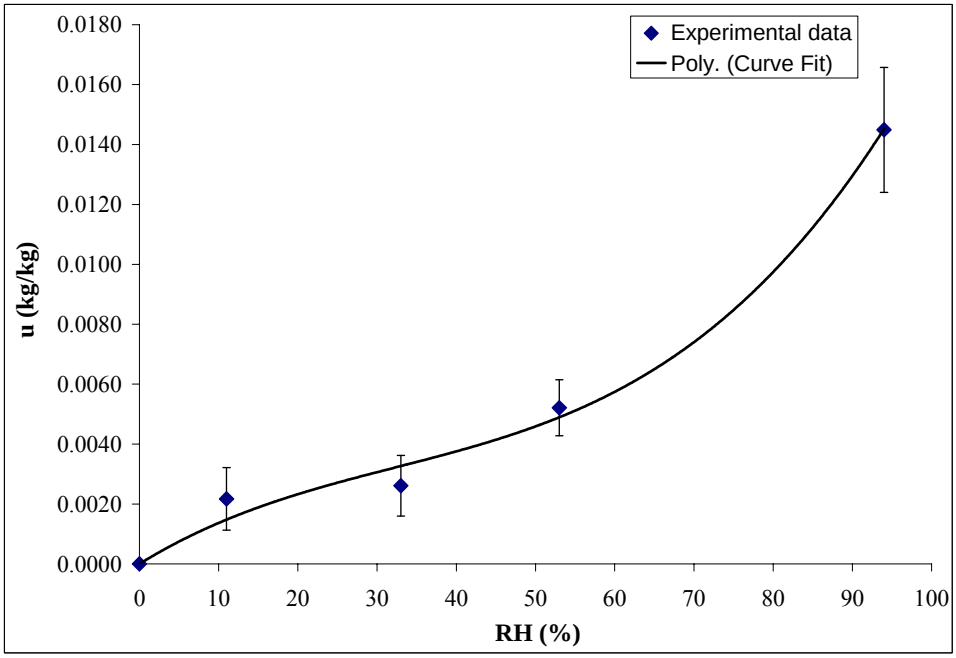

Figure 5.2 Sorption isotherm curve for Japanese Tyvek®

The equation for the curve fit is a third order polynomial and is,

$$u = 0.0303RH^3 - 0.02938RH^2 + 0.01629RH \tag{5.2}$$

where RH is a fraction. The curve fits the data with a correlation coefficient of $r^2 = 0.992$.

Table 5.2 gives the other properties of Tyvek® (defined in Section 5.3.2) that are used in the numerical model. Properties that are not found in literature are calculated from the known properties.

Table 5.2 Properties of dry Tyvek® used in the experiment and numerical simulation.

Property	**Value for Dry Tyvek®**
Density (ρ_{eff})	530 [kg/m^3]
Specific heat (C_{peff})	1440 [J/(kg·K)]
Thermal conductivity (K_{eff})	0.28 [W/(m·K)]
Porosity (ε_g)	0.45
Vapor diffusion coefficient (D_{eff})	3.75 E-07 [m^2/s]
Thickness (L)	150 μm

5.3 Theoretical Model and Numerical Solution Method

A numerical model is used to analyze the one-dimensional diffusion of heat and water vapor in Tyvek® subject to boundary conditions that are present in the experiment. The governing equations for thermal transport and mass diffusivity are used to solve the temperature and vapor density distribution in the membrane over time, as well as the moisture transfer rate through the membrane. An implicit numerical analysis is used to solve the governing equations. FORTRAN coding language is used to program the numerical problem, which solves for the governing equations.

The equations for the numerical model are for the one-dimensional heat and water vapor transfer in a Tyvek® membrane that is subjected to convective boundary conditions at the top surface of the material. The transport processes are representative of the conditions that occur during the experiments described in Section 5.2. The numerical model is used to determine the transient as well as the steady-state heat and moisture transfer response of the membrane. The steady-state mass transfer results from the model and the experimental results are compared to determine how well the model can predict the mass transfer rate through the membrane.

This section reviews the theory and assumptions that are made in deriving the theoretical model for calculating the heat and moisture transfer in the porous Tyvek® membrane. The governing equations for heat and moisture transfer are presented as well as the boundary conditions used in the model. The material properties are given as well as the equations to determine the changes in the properties due to the adsorption and desorption of water vapor in the material.

5.3.1 Local Volume Averaging Theory

The local volume averaging technique is applied to the governing equations that solve for the diffusion of heat and mass transfer through the Tyvek® membrane. This method averages the local properties and equations over a representative elementary volume, such that a macroscopic representation of the heat and mass transfer processes occurring within the membrane can be determined.

A microscopic view of the Tyvek® membrane and an elementary volume of the membrane are shown in Figure 5.3. The membrane thickness (L) is 150 μm, which

contains an elementary volume of polyurethane fibers that are surrounded by a fluid. The elementary volume is of length ℓ, which contains fibers of diameter d ranging between 5 and 10 μm.

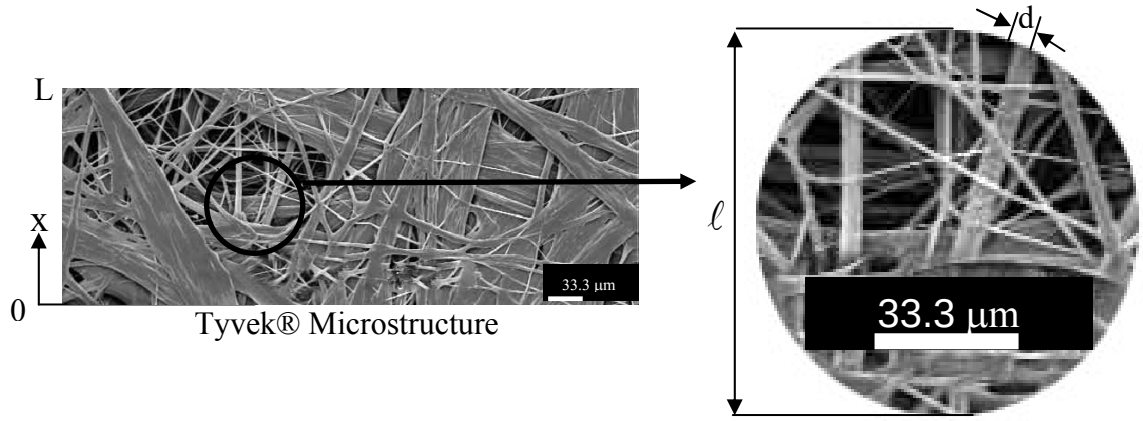

Figure 5.3 A representative elementary volume taken from the Tyvek® membrane, showing the material fibers and the characteristic length scales. Tyvek® microstructure accessed from http://www.wikimedia.org.

In order to use a local volume averaging technique, the length scales of the media should satisfy the requirements of

$$d < \ell << L \tag{5.3}$$

If these lengths scale are satisfied, and the variation of temperature across d is negligible compared to that across L for both the solid and fluid phases (Kaviany, 1991), it can be assumed that both phases are in local thermal equilibrium.

$$\Delta T_d < \Delta T_\ell << \Delta T_L \tag{5.4}$$

The assumption of local thermal equilibrium simplifies the problem from two energy equations (one for the solid and one for the fluid) to a single energy equation for the porous media.

Based on the criteria above, it is shown that the orders of magnitude between the different lengths are not large. If the representative elementary volume length (ℓ) is selected to be ten times as large as the fiber size (d), ℓ is 3 to 1.5 times smaller than the total material thickness (L). Since (L/ℓ) is not large, a temperature gradient across the membrane may be large enough such that local thermal equilibrium between the solid and fluid phase in the representative elementary volume is not satisfied.

Nevertheless, the assumption of local thermal equilibrium is still applied for this material, because other researchers have found it to be valid for diffusion through their materials. The works of Fohr et al. (2002) and Fengzhi et al. (2004) assumed local thermal equilibrium when their material was thin, and the numerical results of Fohr et al. (2002) compared well to experimental results.

5.3.2 Assumptions and Governing Equations

Besides the assumptions used to develop the local volume averaged equations, the following assumptions are made in order to derive the heat and mass transfer equations. The assumptions represent the conditions that occur during the experiment and to simplify the analysis of the problem.

1. Heat and moisture transfer through the porous membrane is one-dimensional.
2. The only transport process within the membrane is heat and water vapor diffusion with phase change.
3. Air and water vapor in the gaseous state behave as an ideal gas.
4. The solid, liquid and gas phases are in thermal and moisture equilibrium.

5. The only heat source in the membrane is the heat of phase change due to adsorption/desorption of water vapor on the membrane fibers.
6. Natural convection within the membrane is neglected since it is considered to be small compared to diffusion of heat and mass that is occurring within the media.
7. Radiation is neglected since the temperature gradient between the water and air is small.

The governing equations for conservation of mass and energy are averaged over the elementary volume, and are presented next. The first equation (5.5) is the mass diffusivity equation. It describes the vapor density distribution throughout the media. The first term is the time rate of change of vapor density, the second is the rate of phase change in the membrane and the third term is the net mass flux through the membrane.

The mass diffusion equation is,

$$\frac{\partial\left(\varepsilon_g \rho_v\right)}{\partial t} - \dot{m} = \frac{\partial}{\partial x}\left(D_{eff}\frac{\partial \rho_v}{\partial x}\right) \tag{5.5}$$

To solve for the temperature distribution in the membrane, the heat diffusion equation is used. The first term is the time rate of change of temperature, the second is the heat of phase change and the third is the net conduction heat flux through the membrane.

The heat diffusion equation is,

$$\left(\rho C\right)_{eff}\frac{\partial T}{\partial t} + \dot{m} h_{fg} = \frac{\partial}{\partial x}\left(k_{eff}\frac{\partial T}{\partial x}\right) \tag{5.6}$$

The mass and heat diffusion equations are coupled by the rate of phase change.

The continuity equation for the adsorbed liquid phase is,

$$\frac{\partial \varepsilon_l}{\partial t} + \frac{\dot{m}}{\rho_l} = 0 \tag{5.7}$$

The rate of phase change is,

$$\dot{m} = -\frac{\partial u}{\partial t}\rho_{eff,dry}, \tag{5.8}$$

where u is the moisture content (kg/kg) of Tyvek® and is determined from the sorption isotherm (equation (5.2) and Figure 5.2).

The volume constraint is,

$$\varepsilon_s + \varepsilon_l + \varepsilon_g = 1 \tag{5.9}$$

The changes in the properties of the membrane are due to moisture adsorption and the temperature of the membrane. They are given as;

$$\rho_{eff} = \varepsilon_s\rho_s + \varepsilon_l\rho_l + \varepsilon_g\rho_g; \tag{5.10}$$

$$C_{p,eff} = \frac{(\varepsilon\rho C)_s + (\varepsilon\rho C)_l + (\varepsilon\rho C)_g}{\rho_{eff}}; \text{ and} \tag{5.11}$$

$$k_{eff} = \varepsilon_s k_s + \varepsilon_l k_l + \varepsilon_g k_g. \tag{5.12}$$

There are many other properties that are used to solve for unknowns present in the previous equations, and these are given in Appendix B.

The thermodynamic relationships are,

$$\phi = \frac{p_v}{p_{sat}}; \tag{5.13}$$

$$p_v = \rho_v R_v T; \tag{5.14}$$

$$p_g = p_a + p_v; \tag{5.15}$$

$$p_a = \rho_a R_a T_a; \text{ and} \tag{5.16}$$

$$\rho_g = \rho_a + \rho_v / \tag{5.17}$$

5.3.3 Boundary and Initial Conditions

The boundary conditions for the problem are:

specified temperature and vapor density at x = 0

$$T = T_s; \text{ and} \tag{5.18}$$

$$\rho_v = \rho_{sat}(T_s) \tag{5.19}$$

convection at x = L

$$h_h \left(T|_L - T_a \right) = -k_{eff} \left. \frac{\partial T}{\partial x} \right|_L; \text{ and} \tag{5.20}$$

$$h_m \left(\rho_v|_L - \rho_{v,a} \right) = -D_{eff} \left. \frac{\partial \rho_v}{\partial x} \right|_L. \tag{5.21}$$

The convective mass transfer coefficient is determined from the correlations developed in Chapter 4. The analogy between heat and mass transfer that has been developed in

this thesis (Nu = *f*(Sh, S*)) is used to derive the convective heat transfer coefficient from the mass transfer coefficient.

For laminar flow:

$$Sh_D = 0.417 \frac{Ra_D^{0.124}}{X^{*0.334}}. \quad (4.1)$$

For turbulent flow:

$$Sh_D = 0.012 \frac{Ra_D^{0.311}}{X^{*0.725}}. \quad (4.4)$$

5.3.4 Numerical Solution

The solution method is based on the finite-difference forms of the governing equations (Appendix C). The coupled, partial differential equations are discretized with second order accuracy for the spatial nodes and the implicit scheme for the time derivative. The central scheme is used for the spatial derivative of the central nodes, while the backward or forward scheme is used to provide a stable solution. The solution is considered to have converged, when for any time step, the percentage change in temperature (T) is less than $0.02\Delta X\Delta T$. The discretized equations and the computer program to solve the equations are presented in Appendix C.

5.3.5 Sensitivity Analysis

The time step (Δt) and grid size (ΔX) used in the numerical solution should be chosen such that the solution comes close to the continuous solution of the partial differential equations. A sensitivity analysis is performed to determine the appropriate time step and grid size, such that the solution is independent of these two parameters.

Figure 5.4 and Figure 5.5 present the numerical results of the temperature and vapor density within the Tyvek® membrane for uniform ΔX and Δt, respectively. The temperature and vapor density are shown at X = L (air-side of the membrane) at a time of 5 seconds. The conditions within the model are the conditions that are present in test 2 from Table 5.1. The initial conditions of the membrane are 17.6°C and 100% RH. The boundary conditions are 17.6°C and 100% RH on the water side (X = 0 m) of the membrane, and 21.4°C, 33.1% RH and $Re_D = 2000$ on the air-side of the membrane.

(a)

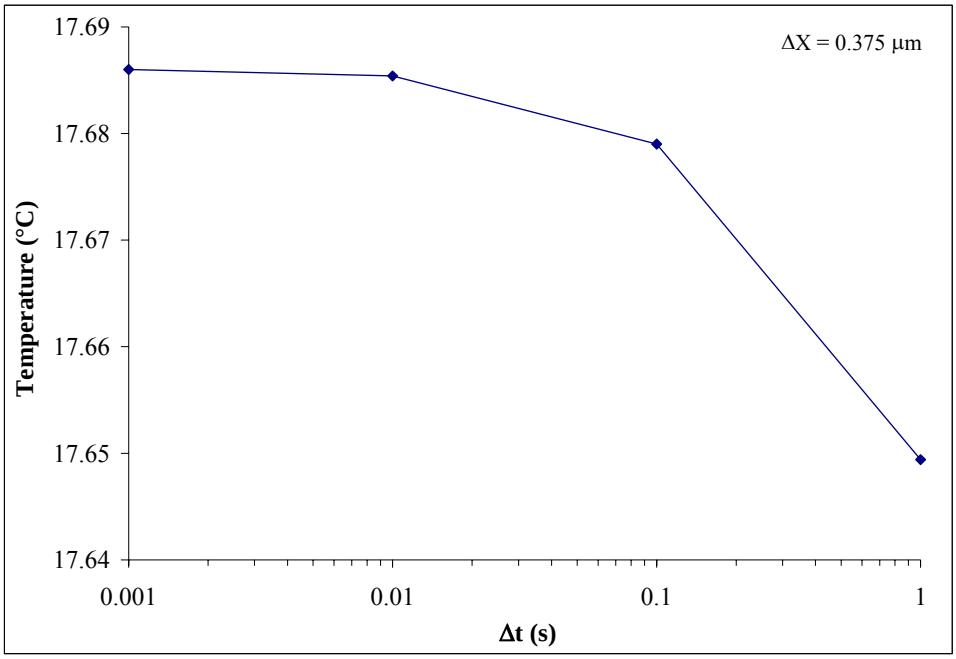

(b)

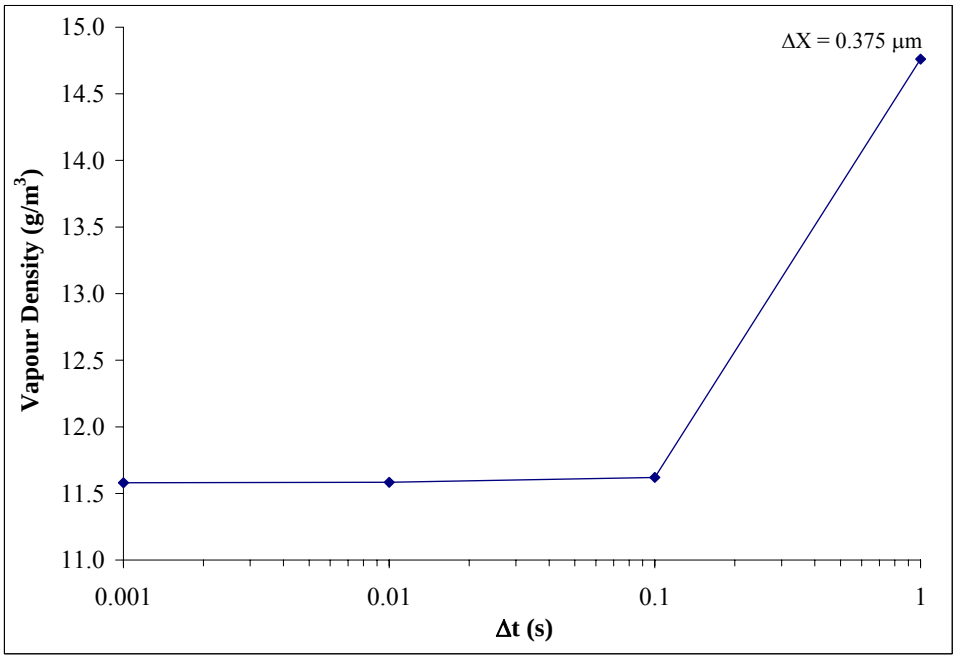

Figure 5.4 Sensitivity graph showing the effect of time step (Δt) on the (a) temperature and (b) vapor density at the air-side surface (X = 150 μm) of the Tyvek® membrane.

(a)

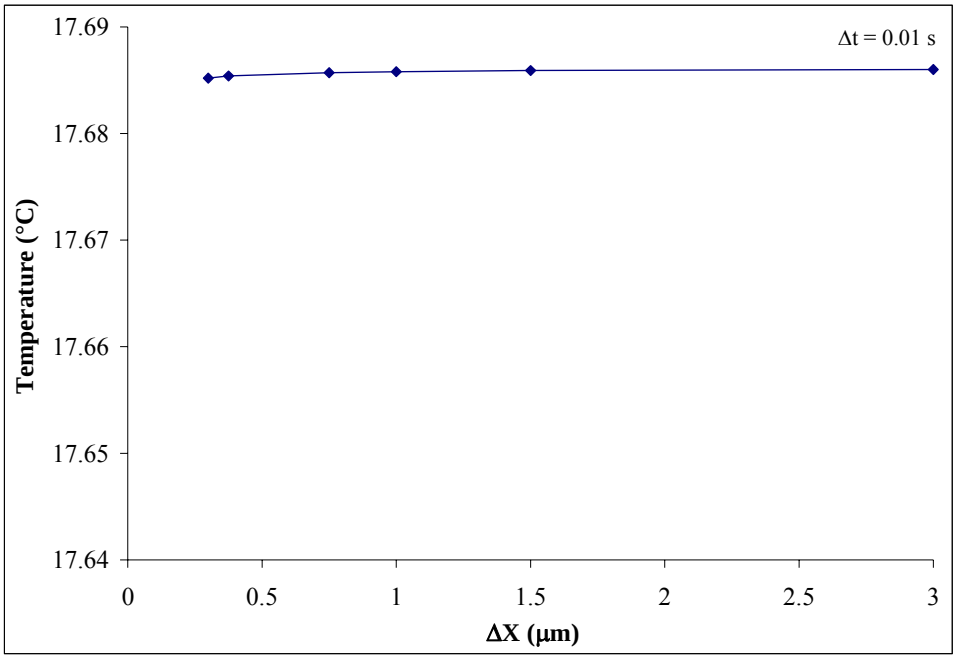

(b)

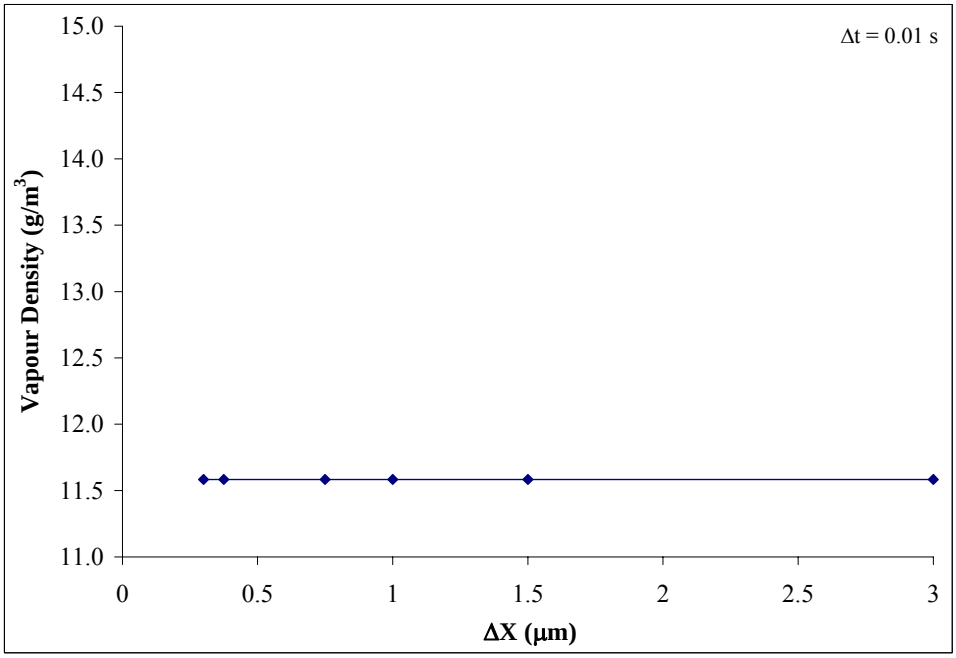

Figure 5.5 Sensitivity graph showing the effect of grid size (ΔX) on the (a) temperature and (b) vapor density at the air-side surface (X = 150 μm) of the Tyvek® membrane.

Figure 5.4 (a) and (b) show the effect of time step on the temperature and vapor density solutions when, respectively, when $\Delta X = 0.375$ μm. The solution approaches a converged value as the time step decreases. Even though the solutions become insensitive to time step when $\Delta t \leq 0.01$ s, a time step of 0.1 s is still a valid time step to use since the change in the solution is very small when the time step decreases below 0.1 s. Figure 5.5 (a) and (b) show that the temperature and vapor density, respectively, are insensitive to grid size (at $\Delta t = 0.01$ s) over a large range of grid sizes. Figures 5.4 and 5.5 show that a uniform time step less than 0.1 s and a grid size between 3 and 0.3 μm are appropriate choices for a converged numerical solution. When decreasing the grid size from 3 μm to 0.3 μm and decreasing the time step from 0.1 s to 0.01 s, the temperature increases by 0.002% and vapor density decreases by 0.3%, while the solution time increases by 66,000%.

Figure 5.6 shows the effect of time step and grid size on the numerical simulation for the moisture transfer rate through the Tyvek® membrane. Decreasing the time step from 0.1 s to 0.01 s and decreasing the grid size from 3 μm to 0.3 μm, decreases the mass transfer rate by 0.6%, and increases the solution time by 66,000%. Since these changes are small, a uniform grid size of 3 μm and time step of 0.1 s are used for all the remaining numerical solutions in this thesis.

(a)

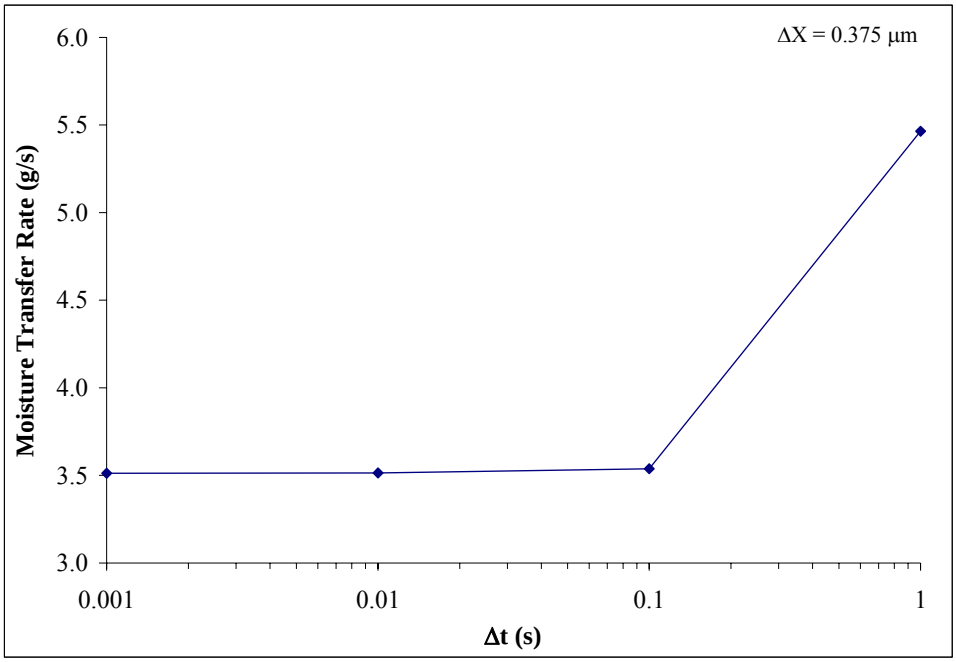

(b)

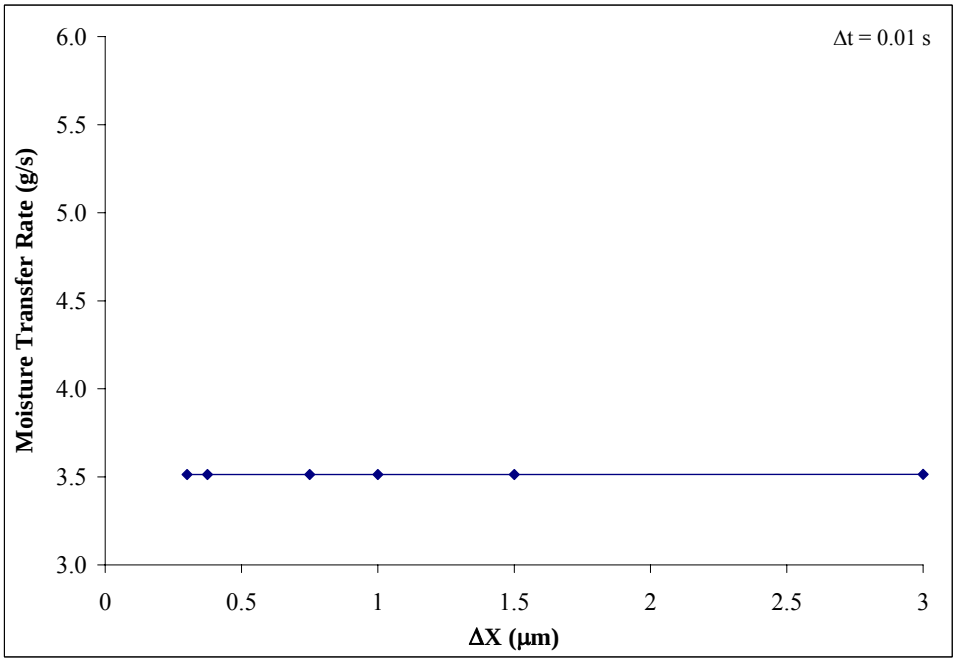

Figure 5.6 Sensitivity graph showing the effect of (a) time step (Δt) and (b) grid size (ΔX) on the simulated moisture transfer rate at the air-side surface (X = 150 μm) of the Tyvek® membrane.

5.3.6 Numerical Results

The numerical model is used to simulate the experiments that are performed on the Tyvek® membrane. The boundary conditions that are used in the numerical model are based on the experimental conditions for each test given in Table 5.1. In the numerical model, the initial temperature of the membrane is the measured water surface temperature and the vapor density is the saturation vapor density at the surface water temperature. The bulk mean temperature and relative humidity of airflow over the top surface of the membrane is the average of the measured upstream and downstream conditions of the airflow for each test in Table 5.1.

The model is used to determine the transient response of the membrane when subjected to a convective airflow at its surface. Figure 5.7 shows the transient response of temperature and vapor density at specific locations in the membrane for test 1. The initial temperature and relative humidity throughout the membrane is 17.4°C and 100% RH (14.8 g/m^3) and the air flow conditions are 22.1°C and 33% RH (6.4 g/m^3). Once the membrane is subjected to a step change in temperature and humidity of the air flowing above the membrane, the temperature throughout the membrane increases due to convective heat transfer from the air to the membrane, and the vapor density decreases, due to convective moisture transfer from the membrane surface to the air.

(a)

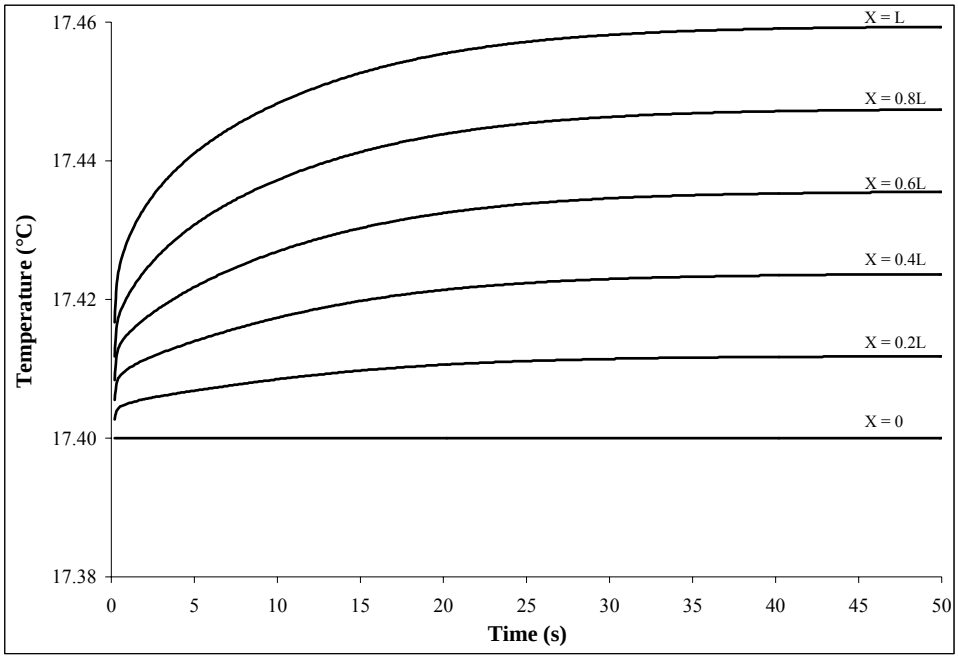

(b)

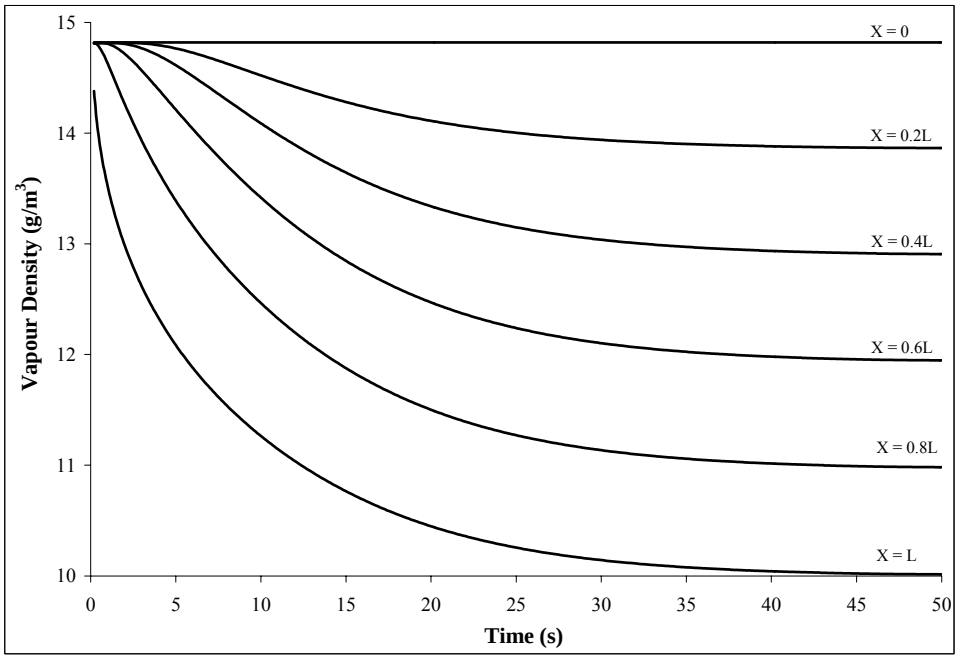

Figure 5.7 The transient profile throughout the membrane for (a) temperature and (b) vapor density for trial 1 in Table 5.1.

Figure 5.8 shows the moisture transfer response as a function of time at the water side of the membrane (X = 0), at the air side of the membrane (X = L), and the average change

throughout the membrane (stored). Initially, the moisture transfer at the air side is high, since the vapor density at the surface of the membrane is high. The moisture transfer rate begins to decrease as the vapor density at the surface of the membrane decreases with time (Figure 5.7). As the membrane losses moisture over time, the moisture stored within the membrane decreases, and the evaporation of water at X = 0 increases. This continues until the moisture transfer rate at the water surface (X = 0) equals the moisture transfer rate on the airside of the membrane (X = L). At this time the moisture content of the membrane remains constant and the moisture storage goes to zero.

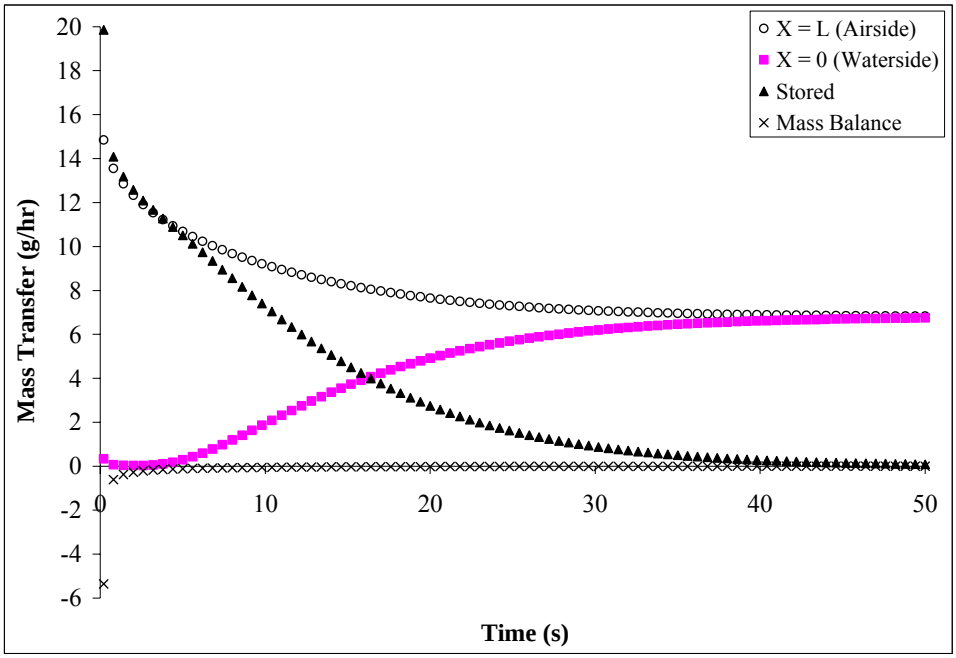

Figure 5.8 Transient moisture transfer rate at different locations within the Tyvek® membrane for trial 1 in Table 5.1.

At any point in time, the amount of moisture transfer at the air side of the membrane should be equal to the change in stored moisture and the amount evaporated. The mass balance in Figure 5.8 shows that the maximum error in the mass transfer rate is approximately 4 g/hr at the beginning, but quickly reduces as time increases. The cause

for this error is due to the grid size and time step used in the numerical model for this short time period. During the period of 5 s < t < 50 s, the mass balance is less than 0.1 g/hr or 1% of the steady state mass transfer rate.

Figure 5.7 and Figure 5.8 show that after approximately 50 s the temperature, vapor density and moisture transfer rate become constant with time. This transient period indicates that the membrane responds quickly to a change in boundary conditions. Since the membrane is thin (150 μm) and has a high vapor permeability, heat and moisture can diffuse quickly through the material. Since the transient period is short, it is feasible to use a steady-state model that can determine the mass transfer rate. The steady-state mass transfer rate is given as

$$m_{ss} = U_m A_s (\rho_{v,s} - \rho_{v,a}), \tag{5.22}$$

where m_{ss} is the steady state mass transfer rate and U_m is the overall mass transfer coefficient,

$$U_m = \left[\frac{L}{D_{eff}} + \frac{1}{h_m} \right]^{-1}. \tag{5.23}$$

U_m is the sum of the resistances to mass transfer between the surface of the water and the airflow, which is composed of the mass diffusion resistance of the membrane (D_{eff}), and the convective mass transfer coefficient (h_m) at the surface (X = L) of the membrane. The convective mass transfer coefficient can be obtained from the Sh_D correlation equations (4.1) or (4.4), depending if the airflow is laminar or turbulent.

The steady state moisture transfer rate determined by the numerical model for test 1 is 8.0 g/hr. Equation (5.25) is used to calculate the steady state moisture transfer rate for

the conditions of trial 1. The calculated steady state moisture transfer rate is 8.0 g/hr, which confirms that the numerical model is correctly calculating the steady state moisture transfer rate for the input data. Table 5.3 and Figure 5.9 present the calculated (equation 5.25) and experimentally determined moisture transfer rates for all experimental tests.

Table 5.3 Calculated and measured moisture transfer rates through a Tyvek® membrane for a range of Re_D.

Test	Re_D	$\dot{m}_{evap}$ [g/hr]		Difference [%]
		Numerical	Experimental	
1	940	8.0	8.6	7
2	2000	8.2	10.8	24
3	5140	10.7	14.4	26
4	5240	10.8	14.0	23

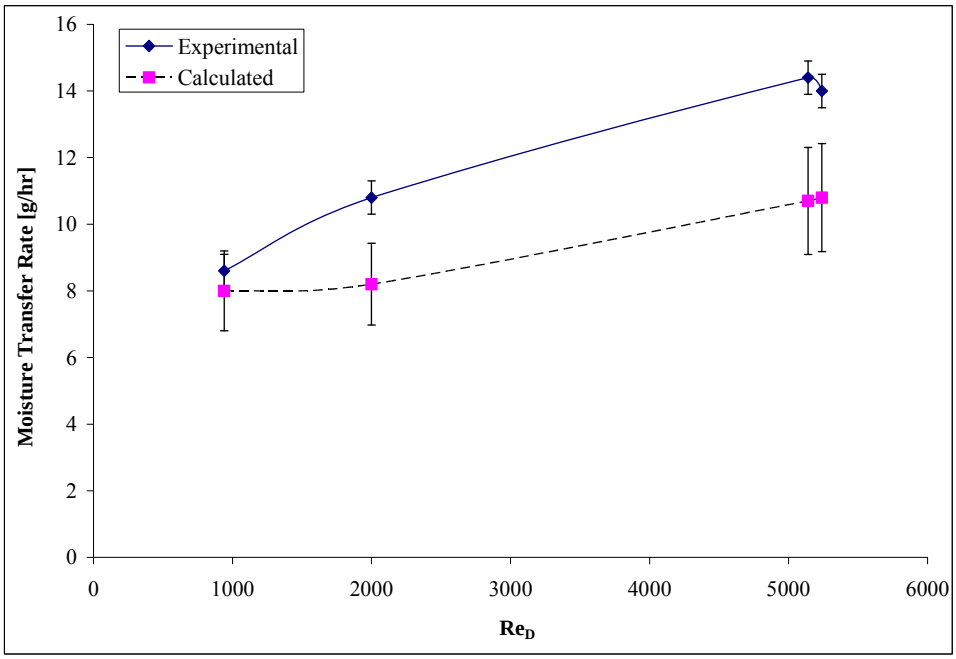

Figure 5.9 Calculated and measured moisture transfer rates through a Tyvek® membrane for a range of Re_D.

The uncertainty in m_{ss} (shown with uncertainty bars in Figure 5.9) is approximately ±15%, since the mass diffusion coefficient (D_{eff}) has an uncertainty of ±25%, the

convective mass transfer coefficient has an uncertainty of ±10%, and the vapor density difference has an uncertainty of ±2%. The uncertainty in the measured moisture rates are approximately ±0.5 g/h, and are shown with uncertainty bars in Figure 5.9. (Considering that the uncertainty in m_{ss} is 15%, the differences between the experimental and calculated data (7% to 26%) are reasonable, but not totally accounted for. The differences between the experiment and the steady state model could be due to a slightly different mass transfer coefficient for flow over Tyvek® than for flow over a free water surface. This requires further research.

CHAPTER 6

CONCLUSION AND FUTURE WORK

6.1 Conclusion

The goal of this thesis is to measure the convective mass transfer coefficients for a horizontal rectangular duct within the TMT facility, and use the results to study heat and moisture transfer through a Tyvek® membrane.

6.1.1 Measured Convective Coefficients

In this thesis, combined forced and natural convection evaporation of water from a pan forming the lower panel of a rectangular duct is investigated experimentally. Mass transfer measurements are made for a hydrodynamically developed airflow with developing concentration and thermal boundary layers. The effects of forced convection evaporation are investigated by varying the velocity of the air passing through the duct in the laminar and turbulent flow regimes between a Re_D of 560 and 8,100. The effect of the density difference between the bulk flow and the air at the surface of the water is determined for Ra_D between 6,100 and 82,500. The convective mass transfer coefficient is dependent on the strength of natural and forced convection, as well the temperature and humidity of the bulk airflow. The effect of the temperature and humidity of the air stream can be accounted for by using the operating condition factor H* or S*, which are ratios between the heat and moisture transfer potentials in the experiment. Correlations for Sh_D as a function of X*, Ra_D and H* are developed to account for the effects of the

entrance region, forced and natural convection, as well as the operating conditions of the experiment on the evaporation process for laminar and turbulent airflow. The correlations in the laminar flow region are:

$$Sh_D = 0.417 \frac{Ra_D^{0.124}}{X^{*0.334}} \tag{6.1}$$

and

$$Sh_D = \frac{2.11}{X^{*0.308}|H^*|^{0.371}}, \tag{6.2}$$

which are valid for $6{,}100 \le Ra_D \le 82{,}500$, $0.011 \le X^* \le 0.037$ and $-3.6 \le H^* \le -1.4$.

The correlations in the turbulent flow regime are:

$$Sh_D = 0.012 \frac{Ra_D^{0.311}}{X^{*0.725}}, \tag{6.3}$$

and

$$Sh_D = \frac{0.382}{X^{*0.719}|H^*|^{0.494}}, \tag{6.4}$$

which are valid for $20{,}900 \le Ra_D \le 46{,}000$, $0.003 \le X^* \le 0.007$ and $-2.1 \le H^* \le -1.4$.

The experimental data in this thesis compare favorably to numerical and experimental data in the literature. These comparisons show that the magnitude and direction of heat and mass transfer affect Sh_D. Sh_D is always larger when the water surface is heated above the air temperature than when the water is cooled below the air temperature. This research extends the literature for the case of a cooled water surface. The comparisons also show that it is possible to use Nu_D data from the literature together with the traditional analogy between heat and mass transfer,

$$Sh = Nu\left(\frac{Sc}{Pr}\right)^{1/3}, \tag{6.5}$$

which can be found in convection heat/mass transfer textbooks to estimate Sh_D. However, such an estimate can have errors as large as 30% if the effects of the temperature and humidity conditions of the air and resulting Ra_D, H* (S*) are not accounted for.

An analogy between heat and mass transfer is developed that uses the operating conditions (S^*_{lm}) and Sh_D from the experiment to calculated Nu_D, where

$$Nu_D = Sh_D S^*_{lm}. \tag{6.6}$$

Nu_D calculated from the new analogy is compared to Nu_D determined from the measured sensible and latent heat transfer between the bulk airflow and the surface of the water (Figures 4.9, 4.10 and 4.11). Nu_D calculated by the analogy agrees within experimental uncertainty bounds with Nu_D determined from the measured latent heat transfer for all experimental data. However, agreement with the sensible heat transfer Nu_D is not as good due to sensible heat transfer between the ambient and the test section, which heats the water surface and causes the sensible Nu_D to be up to 50% less than Nu_D calculated by the analogy.

A new method is developed that is able to convert a Nu determined under pure heat transfer conditions (i.e., heat transfer with no mass transfer) (Nu_h) or a pure mass transfer Sh (Sh_m) into a Nu and Sh that are valid for simultaneous heat and mass transfer. The new method uses the traditional analogy between heat and mass transfer (equation (6.5)) and the following equations:

$$Sh_{h/m} = \frac{Sh_m}{|H^*|^{0.371}} \tag{6.7}$$

and

$$Nu_{h/m} = 1.18 Sh_m |H^*|^{0.671} \tag{6.8}$$

The new method and equations (6.7) and (6.8) are verified with the $Nu_{D,h}$ data of Lyczkowski et al. (1981). It is shown that the $Nu_{D,h/m}$ and $Sh_{D,h/m}$ determined from Lyczkowski's $Nu_{D,h}$ data agree within experimental uncertainty bounds with the $Nu_{D,h/m}$ and $Sh_{D,h/m}$ measured in this thesis.

The turbulent flow experiments in this thesis compare well with similar experiments of Chuck (1985). The experimental data extends the data for different operating conditions, Ra_D as well as larger values of X*.

6.1.2 Convective Mass Transfer with a Permeable Membrane

To study moisture transfer through a permeable membrane, a numerical model is developed and experiments are performed to verify the numerical model. In the experiments, a Tyvek® membrane is placed over a water surface, and subjected to a convective airflow over the top surface of the membrane. Four experimental trials are performed over a range of Reynolds numbers (940 to 5240), and the moisture transfer rates through the membrane are measured. The differences between the predicted and measured moisture transfer rates range from 7% to 26%. Discrepancies between experimental and numerical results may due to a different mass transfer coefficient for air flow over Tyvek® than for flow over a free water surface. The numerical results show that the membrane responds very quickly to a step change in temperature and

relative humidity of the air stream. Since the transients occur over a short period of time (less than 1 minute), it is feasible to use a steady state model to determine the heat and mass transfer rates through the material for HVAC applications.

6.2 Future Work

The experimental investigation of determining the convective heat and mass transfer coefficients for a horizontal rectangular duct has opened areas of research that have not been explicitly discussed in past research. Future work can include developing a numerical model to simulate the experimental conditions, and verify the experimental results. A numerical model can simulate a larger range of boundary conditions that are not possible through experimentation, which could give a more detailed understanding of the heat and mass transfer relationship.

This thesis has introduced the concept of using a vapor permeable membrane as the critical component in a radiative type enthalpy exchanger. Extensive experimental testing over a larger range of boundary conditions can be performed to gain a larger understanding of the membrane's performance under different operating conditions. An investigation into the construction of a prototype enthalpy exchanger and the experimental testing of it under real world conditions can validate its practicality.

REFERENCES

Advanced Buildings - Technologies and Practices. http://www.advancedbuildings.org/ (September 2006).

ANSI/ASME PTC 19.1 – 1998, Test Uncertainty, ASME, New York.

ASHRAE Fundamentals Handbook 2005, ASHRAE, Atlanta.

ASHRAE HVAC Systems and Equipment Handbook 2004, ASHRAE, Atlanta.

ASTM E104, Maintaining constant relative humidity by means of aqueous solutions, ASTM, Philadelphia, 1985.

Basak T., Roy S., Balakrishnan A.R., Effects of thermal boundary conditions on natural convection flows within a square cavity, Int. J. Heat Mass Transfer 49 (2006) 4525-4535.

Chen X.D., Lin S.X., Chen G., On the ratio of heat to mass transfer coefficient for water evaporation and its impact upon drying modeling, Int. J. Heat Mass Transfer 45 (2002) 4369-4372.

Chuck W., Evaporation of water from a recessed surface to a parallel forced convection airflow, Ph.D. thesis, Department of Mechanical Engineering, University of Minnesota, Minneapolis, MN, 1985.

Chuck W., Sparrow E.M., Evaporative mass transfer in turbulent forced convection duct flows, Int. J. Heat Mass Transfer 30 (2) (1987) 215-222.

Chue S.H., Pressure probes for fluid measurement, Progress in Aerospace Science 16 (2) (1975) 147-223.

Fan H., Modeling a run-around heat and moisture recovery system, M.Sc. thesis, Department of Mechanical Engineering, University of Saskatchewan, Saskatoon, SK, Canada, 2005, (http://library2.usask.ca/theses/available/etd-05172005-160018).

Fengzhi L., Yi L., Yingxi L., Zhongxuan L., Numerical simulation of coupled heat and mass transfer in hygroscopic porous materials considering the influence of atmospheric pressure, Numerical Heat Transfer 45 (Part B) (2004) 249-262.

Findley M.E., Tanna V.V., Rao Y.B., Yeh C.L., Mass and heat transfer relations in evaporation through porous membranes, AIChe Journal 15 (4) (1969) 483-489.

Fohr J.P., Couton D., Treguier G., Dynamic heat and water transfer through layered fabrics, Textile Res. J. 72 (1) (2002) 1-12.

Goldstein, R.J., Cho, H.H. Review of mass transfer measurements using naphthalene sublimation, Experimental Thermal and Fluid Science 10 (4) (1995) 416-434.

Huang C.C., Yan W.M., Jang J.H., Laminar mixed convection heat and mass transfer in vertical rectangular ducts with film evaporation and condensation, Int. J. Heat Mass Transfer 48 (2005) 1772-1784.

Incropera F.P., DeWitt D.P., Fundamentals of Heat and Mass Transfer, fifth ed., John Wiley & Sons, New York, 2002, pp. 465-531.

Iskra C.R., Simonson C.J., Convective mass transfer coefficient for a hydrodynamically developed airflow in a short rectangular duct, Int. J. Heat Mass Transfer 50 (2007) 2376-2393.

ISO, Measurement of fluid flow by means of pressure differential devices, ISO 5167-1, Switzerland, 1991.

ISO 12571, Building Materials – Determination of hygroscopic sorption curves, ISO, Brussels, 1996.

Jang J.H., Yan W.M., Huang C.C., Mixed convection heat transfer enhancement through film evaporation in inclined square ducts, Int. J. Heat Mass Transfer 48 (2005) 2117-2125.

Kaviany, M., Principles of heat transfer in porous media, Springler-Verlag, New York, 1991.

Kondjoyan A., Daudin J.D., Determination of transfer coefficients by psychrometry, Int. J. Heat Mass Transfer 36 (7) (1993) 1807-1818.

Li Y., Holcombe B.V., A two-stage sorption model of the coupled diffusion of moisture and heat in wool fabrics, Textile Res. J. 62 (4) (1992) 211-217.

Lin J.N., Tzeng P.Y., Chou F.C., Yan W.M., Convective instability of heat and mass transfer for laminar forced convection in the thermal entrance region of horizontal rectangular channels, Int. J. Heat and Fluid Flow 13 (3) (1992) 250-258.

Lyczkowski R.W., Solbrig C.W., Gidaspow D., Forced convection heat transfer in rectangular ducts – General case of wall resistance and peripheral conduction for ventilation cooling of nuclear waste repositories, Nuclear Engineering and Design 67 (3) (1981) 357-378.

Olutimayin S.O., Vapor boundary layer growth during transient heat and moisture transfer in cellulose insulation, M.Sc. thesis, Department of Mechanical Engineering, University of Saskatchewan, Saskatoon, SK, Canada, 2004.

Olutimayin S.O., Simonson C.J., Measuring and modeling vapor boundary layer growth during transient diffusion heat and moisture transfer in cellulose insulation, Int. J. Heat Mass Transfer 48 (2005) 3319-3330.

Osanyintola F.O., Transient moisture characteristics of spruce plywood, M.Sc. thesis, Department of Mechanical Engineering, University of Saskatchewan, Saskatoon, SK, Canada, 2005, (http://library2.usask.ca/theses/available/etd-12222005-082100).

Osanyintola F.O., Iskra C.R., Simonson C.J., Ojanen T., Ahonen J., Moisture characteristics of plywood - part II: Moisture buffering capacity of plywood interior sheathing, Proceedings of the Nordic Building Physics Conference, Reykjavík, Iceland, June 13-15, 2005, 8 pages.

Ou J.W., Cheng K.C., Lin R.C., Natural convection effects on Graetz problem in horizontal rectangular channels with uniform wall temperature for large Pr, Int. J. Heat Mass Transfer 17 (1974) 835-843.

Pauken M.T., An experimental investigation of combined turbulent free and forced evaporation, Experimental Thermal and Fluid Science 18 (1999) 334-340.

Prata A.T., Sparrow E.M., Evaporation of water from a partially filled cylindrical container to a forced convection airflow, Int. J. Heat Mass Transfer 29 (4) (1986) 539-547.

Raju K.G., Porey P.D., Asawa G.L., Displacement effect in Pitot tube measurements in shear flows, J. of Wind Engineering 66 (1997) 95-105.

Sadek H., Robinson A.J., Cotton J.S., Ching C.Y., Shoukri M., Electrohydrodynamic enhancement of in-tube convective condensation heat transfer, Int. J. Heat Mass Transfer 49 (2006) 1647-1657.

Sander U., Janssen H., Industrial application of vapor permeation, Journal of Membrane Science 61 (1991) 113-129.

Shah R.K., London A.L., Laminar Flow Forced Convection in Ducts, Academic Press, New York, 1978, Ch. VII.

Simonson C.J., Besant R.W., Energy wheel effectiveness: Part I - Development of dimensionless groups, Int. J. Heat Mass Transfer 42 (12) (1999a) 2161-2170.

Simonson C.J., Besant R.W., Energy wheel effectiveness: Part ĨĨ - Correlations, Int. J. Heat Mass Transfer, 42 (12) (1999b) 2171-2185.

Sparrow E.M., Kratz G.K., Schuerger M.J., Evaporation of water from a horizontal surface by natural convection, J. Heat Transfer-Trans. ASME 105 (3) (1983) 469-475.

Tao Y.X., Besant R.W., Rezkallah K.S., A mathematical model for predicting the densification and growth of frost on a flat plate, Int. J. Heat Mass Transfer 36 (2) (1993) 353-363.

Talukdar P., Simonson C., Transient Heat and Moisture Transfer within Gypsum, IEA/ECBCS Annex 41 Conference, Kyoto, Japan, April 3-5, 2006, 9 pages.

Wehner J., Miller B., Rebenfeld L., Dynamics of water vapor transmission through fabric barriers, Textile Res. J. 58 (1988) 581-592.

Wexler A., Wildhack W.A., Humidity and Moisture: Measurement and Control in Science and Industry, Vol. 3, Reinhold, New York, 1965, pp. 257-272.

White F.M., Fluid Mechanics, fourth ed., McGraw-Hill, Boston, 1999, pp. 771.

Wikimedia – A Multilingual Free Encyclopedia. http://www.wikimedia.org (August, 2006).

Xia Y., Jacobi A.M., Air-side data interpretation and performance analysis for heat exchangers with simultaneous heat and mass transfer: Wet and frosted surfaces, Int. J. Heat Mass Transfer 48 (2005) 5089-5102.

Yan, W.M, Combined buoyancy effects of thermal and mass diffusion on laminar forced convection in horizontal rectangular ducts, Int. J. Heat Mass Transfer 39 (4) (1996) 1479-1488.

Yasuda T., Miyama M., Yasuda H., Dynamic water vapor and heat transport through layered fabrics, Part II: Effect of the chemical nature of fibers, Textile Res. J. 62 (4) (1992) 227-235.

Yasuda T., Miyama M., Muramoto A., Yasuda H., Dynamic water vapor and heat transport through layered fabrics, Part III: Surface temperature change, Textile Res. J. 64 (8) (1994) 457-461.

Yun R., Kim Y., Kim M.S., Convective boiling heat transfer characteristics of CO_2 in microchannels, Int. J. Heat Mass Transfer 48 (2005) 235-242.

Zhang L.Z., Investigation of moisture transfer effectiveness through a hydrophilic polymer membrane with a field and laboratory emission cell, Int. J. Heat Mass Transfer 49 (2006) 1176-1184.

Zhang L.Z., Jiang Y., Heat and mass transfer in a membrane-based energy recovery ventilator, J. of Membrane Science 163 (1999) 29-38.

Zhang L.Z., Niu J.L., Effectiveness correlations for heat and moisture transfer processes in an enthalpy exchanger with membrane cores, J. Heat Transfer-Trans. ASME 124 (5) (2002) 922–929.

Zhang L.Z., Niu J.L., Laminar fluid flow and mass transfer in a standard field and laboratory emission cell, Int. J. Heat Mass Transfer 46 (2003) 91-100.

Zhang X., Zhang W., Hao X., Zhang H., Zhang Z., Zhang J., Mathematical model of gas permeation through PTFE porous membrane and the effect of membrane pore structure, Chinese J. Chemical Engineering 11 (4) (2003) 383-387.

APPENDIX A

UNCERTAINTY ANALYSIS

The uncertainty analysis used in determining the uncertainties in the results in this thesis are presented in this appendix. An uncertainty analysis helps to estimate the accuracy of measurements and calculations in order to give a level of confidence in the results obtained in this thesis.

The purpose of an uncertainty analysis is to quantify the degree of confidence in measured and calculated data. The ASME standard (ANSI/ASME PTC 19.1, 1998) defines the total 95% confidence uncertainty as the room-sum-square uncertainty (U_{RSS}) by combining the total bias uncertainty (U_B) with the total precision uncertainty (U_P) as follows:

$$U_{RSS}=\left(U_B^2+U_P^2\right)^{1/2}. \tag{A.1}$$

The bias error is a systematic error that causes measured values to deviate from the true value by a consistent amount. These types of errors may result from calibration of measurement equipment, data acquisition equipment or the setup of the experiment. Precision uncertainties are statistical fluctuations in the measured data due to the precision limitations of the measurement device, and how constant the measured parameters are during an experimental trial. The precision uncertainty is defined as:

$$U_P = tS_{\bar{x}}, \tag{A.2}$$

where t is the Student's t value at a 95% confidence level, and $S_{\bar{x}}$ is the estimate of the standard deviation of the mean of N measurements.

$$S_{\bar{x}} = \frac{S_x}{\sqrt{N}}, \tag{A.3}$$

where

$$S_x = \left[\frac{\sum_{k=1}^{N} \left(X_k - \bar{X} \right)^2}{N - 1} \right]^{1/2} . \tag{A.4}$$

The uncertainty in the calculated independent and dependent parameters in this thesis are determined from the uncertainties of the measured properties. For example, in the calculation of the Sherwood number (Sh_D),

$$Sh_D = \frac{h_m D_h}{D_{AB}}, \tag{A.5}$$

the total uncertainty is the root-sum-square uncertainty (U_{RSS}), which includes the individual uncertainties of the measured data as shown below,

$$\frac{USh_D}{Sh_D} = \left(\left(\frac{Uh_m}{h_m} \right)^2 + \left(\frac{UD_h}{D_h} \right)^2 + \left(\frac{UD_{AB}}{D_{AB}} \right)^2 \right)^{1/2} . \tag{A.6}$$

USh_D is the uncertainty in the calculated Sherwood number, Uh_m is the uncertainty in the measured convective mass transfer coefficient, UD_h is the uncertainty in the calculated hydraulic diameter of the test section duct and UD_{AB} is the uncertainty in the binary mass diffusion coefficient.

APPENDIX B

PROPERTIES USED IN THE NUMERICAL MODEL

This appendix contains all the property data used in the numerical model presented in Chapter 6. These properties are obtained from literature or calculated from other properties. The following property data are assumed to stay constant over the temperature range present in the numerical analysis.

Property Data for Water

$C_w = 4184\ \text{J/kg}\cdot\text{K}$ (Incropera and DeWitt, 2002)
$k_w = 0.65\ \text{W/m}\cdot\text{K}$ (Incropera and DeWitt, 2002)
$\rho_w = 984\ \text{kg/m}^3$ (Incropera and DeWitt, 2002)

Property Data for Air

$C_{p,a} = 1007\ \text{J/kg}\cdot\text{K}$ (Incropera and DeWitt, 2002)
$k_a = 0.026\ \text{W/m}\cdot\text{K}$ (Incropera and DeWitt, 2002)
$R_a = 287\ \text{J/kg}\cdot\text{K}$ (ASHRAE Fundamentals, 2005)
h_h = Calculated
h_m = Calculated

Property Data for Water Vapor:

$C_{p,v} = 1862\ \text{J/kg}\cdot\text{K}$ (Incropera and DeWitt, 2002)
$R_v = 462\ \text{J/kg}\cdot\text{K}$ (ASHRAE Fundamentals, 2005)
$k_v = 0.017\ \text{W/m}\cdot\text{K}$ (Incropera and DeWitt, 2002)
ρ_v = Calculated

Solid (Polyethylene) Properties

$\rho_s = 950$ kg/m^3 (Goodfellow, 2006)
$C_{p,s} = 1900$ J/kg$\cdot$K (Goodfellow, 2006)
$k_s = 0.48$ W/m$\cdot$K (Goodfellow, 2006)

Other Properties:

$D_{AB} = 2.6E^{-5}$ m^2/s (Incropera and DeWitt, 2002)
$h_{fg} = 2455$ kJ/kg (Incropera and DeWitt, 2002)

APPENDIX C

DISCRETIZED EQUATIONS AND THE COMPUTER SIMULATION PROGRAM

The discretized equations used within the numerical model present in Chapter 6 are given in this appendix.

C.1 Discretized Equations

The rate of phase change is,

$$\dot{m}_{(I,J)} = \rho_{eff,dry} \frac{(u_{(I,J)} - u_{(I,J-1)})}{\Delta t} \tag{C.1}$$

The continuity for the adsorbed phase is,

$$\frac{\varepsilon_{l(I,J)} - \varepsilon_{l(I,J-1)}}{\Delta t} + \frac{\dot{m}(I,J)}{\rho_l} = 0 \tag{C.2}$$

The gas diffusion of water vapor is,

$$\rho_{v(I,J)} \left(\frac{\varepsilon_{g(I,J)} - \varepsilon_{g(I,J-1)}}{\Delta t} \right) + \varepsilon_{g(I,J)} \left(\frac{\rho_{v(I,J)} - \rho_{v(I,J-1)}}{\Delta t} \right) - \dot{m}_{(I,J)} =$$

$$D_{eff(I,J)} \left(\frac{\rho_{v(I-1,J)} - 2\rho_{v(I,J)} + \rho_{v(I+1,J)}}{\Delta X^2} \right) + \tag{C.3}$$

$$\left(\frac{\left(D_{eff(I+1,J)} - D_{eff(I-1,J)} \right) \left(\rho_{v(I+1,J)} - \rho_{v(I-1,J)} \right)}{4\Delta X^2} \right)$$

The energy transport equation is ,

$$\left(\rho_{(I,J)}C_{(I,J)}\right)_{eff}\left(\frac{T_{(I,J)}-T_{(I,J-1)}}{\Delta t}\right)+\dot{m}_{(I,J)}h_{fg}=$$

$$k_{eff\,(I,J)}\left(\frac{T_{(I-1,J)}-2T_{(I,J)}+T_{(I+1,J)}}{DX^2}\right)+ \tag{C.4}$$

$$\left(\frac{\left(k_{eff(I+1,J)}-k_{eff(I-1,J)}\right)\left(T_{(I+1,J)}-T_{(I-1,J)}\right)}{4DX^2}\right).$$

The volume constraint is,

$$\varepsilon_s(I,J)+\varepsilon_l(I,J)+\varepsilon_g(I,J)=1. \tag{C.5}$$

The thermodynamic relationships are:

$$\phi(I,J)=\frac{p_v(I,J)}{P_{vsat}(I,J)} \tag{C.6}$$

$$P_v(I,J)=\rho_v(I,J)R_vT(I,J) \tag{C.7}$$

$$P_g(I,J)=P_v(I,J)+P_a(I,J) \tag{C.8}$$

$$P_a(I,J)=\rho_a(I,J)R_aT(I,J) \tag{C.9}$$

$$\rho_g(I,J)=\rho_v(I,J)+\rho_a(I,J) \tag{C.10}$$

The effective properties of the Tyvek® medium are,

$$\rho_{eff\,(I,J)}=\varepsilon_s\rho_s+\varepsilon_{l(I,J)}\rho_l+\varepsilon_{g(I,J)}\rho_{g(I,J)} \tag{C.11}$$

$$Cp_{eff\,(I,J)}=\frac{(\varepsilon\rho C)_s+\varepsilon_{l(I,J)}\rho_lC_l+\varepsilon_{g(I,J)}\rho_{g(I,J)}C_{g(I,J)}}{\rho_{eff\,(I,J)}} \tag{C.12}$$

$$k_{eff\,(I,J)}=(\varepsilon k)_s+\varepsilon_{l(I,J)}k_l+\varepsilon_{g(I,J)}k_{g(I,J)} \tag{C.13}$$

The boundary conditions are

adiabatic at X = 0

$$T(0,J) = T_w \quad , \tag{C.14}$$

$$\rho_{v(0,J)} = \rho_{v,sat}(T_w) \tag{C.15}$$

convection at X = L

$$h_h\left(T_{(L,J)} - T_a\right) = -K_{eff}\left(\frac{T_{(L-2,J)} - 4T_{(L-1,J)} + 3T_{(L,J)}}{2\Delta X}\right) \tag{C.16}$$

$$h_m\left(\rho_{v(L,J)} - \rho_{v,a}\right) = -D_{eff\,(I,J)}\left(\frac{\rho_{v(L-2,J)} - 4\rho_{v(L-1,J)} + 3\rho_{v(L,J)}}{2\Delta X}\right) \tag{C.17}$$

The initial conditions are

$$T_{(I,0)} = T_w \tag{C.18}$$

$$\rho_{v(I,0)} = \rho_{v,sat}(T_w) \tag{C.19}$$

C.2 Computer Simulation Program

The computer simulation program presented below is written in FORTRAN program language

DECLARE ALL VARIABLES AND CONSTANTS

```
DOUBLE PRECISION   ATMP, C8, C9, C10, C11, C12, C13, CONVCR, CONVH
DOUBLE PRECISION   CONVM, CPA, CPEFF(3000), CPG(3000), CPL, CPS, CPV
DOUBLE PRECISION   CPW, DAB, DEFF(3000), DENEFF(3000)
DOUBLE PRECISION   DENEFFPREV(3000), DENL, DHYD, DIFFMAX, DENAI
DOUBLE PRECISION   DIFFTEMP(3000), DENA(3000), DENS, DENW, DRYDEN
DOUBLE PRECISION   DENG(3000), DIFFVD(3000), GVF(3000), GVFPREV(3000),
DOUBLR PRECISION   HFG , INIDENEFF, INIM, INIT, INIU, INILVF, INIGVF
DOUBLE PRECISION   INIVD, KEFF(3000), KG(3000), KL, KV, KS, KW, KA
DOUBLE PRECISION   LVF(3000), LVFPREV(3000), MSTORE, MCONV, M(3000)
DOUBLE PRECISION   MASSDIFF, MAXDIFF, MINPUT, MPREV(3000), NU
DOUBLE PRECISION   POROS, PRESSA(3000), PVSATA, PVSAT(3000)
DOUBLE PRECISION   PRESSV(3000), QCONV,QCOND,QSTORE, QDIFF
DOUBLE PRECISION   QSTOREPRESSV(3000), REYNOLDS, RA, RAD
DOUBLE PRECISION   RT3(3000), RT1(3000), RELAX, RESIDTOL RTTOTAL
DOUBLE PRECISION   RT2(3000), RT2TOTAL, RVD1(3000), RVD2(3000)
DOUBLE PRECISION   RVD3(3000), RVDTOTAL, RVD2TOTAL, R1(3000)
DOUBLE PRECISION   R2(3000), RHA, RH(3000), RV, SUMTEMP1, SUMTEMP2
DOUBLE PRECISION   SVF, SSCONV, SH, T(3000), TEMPDIFF(3000)
DOUBLE PRECISION   TPREV(3000), TPI(3000), TMAX, TMIN, TORTU, TW
DOUBLE PRECISION   U(3000), UPREV(3000), VD(3000), VDPREV(3000)
DOUBLE PRECISION   VDPREV(3000), VDPI(3000), VDSAT, VDA
DOUBLE PRECISION   VDDIFF(3000), XSTAR

REAL DELTAX, DELTAT

OPEN (UNIT=1, FILE='TEMPERATUREDIST.TXT', STATUS='REPLACE')
OPEN (UNIT=2, FILE='VAPORDENSITYDIST.TXT', STATUS='REPLACE')
OPEN (UNIT=3, FILE='LVF.TXT', STATUS='REPLACE')
OPEN (UNIT=4, FILE='U.TXT', STATUS='REPLACE')
OPEN (UNIT=5, FILE='MSTORE.TXT', STATUS='REPLACE')
OPEN (UNIT=6, FILE='MCONV.TXT', STATUS='REPLACE')
OPEN (UNIT=7, FILE='MINPUT.TXT', STATUS='REPLACE')
OPEN (UNIT=8, FILE='QSTORE.TXT', STATUS='REPLACE')
OPEN (UNIT=9, FILE='QCONV.TXT', STATUS='REPLACE')
OPEN (UNIT=10,FILE='QCOND.TXT', STATUS='REPLACE')
OPEN (UNIT=11,FILE='MASSDIFF.TXT', STATUS='REPLACE')
OPEN (UNIT=12,FILE='QDIFF.TXT', STATUS='REPLACE')
OPEN (UNIT=13,FILE='M.TXT', STATUS='REPLACE')
OPEN (UNIT=14,FILE='CONVM.TXT', STATUS='REPLACE')
OPEN (UNIT=15,FILE='CONVH.TXT', STATUS='REPLACE')
OPEN (UNIT=16,FILE='K.TXT', STATUS='REPLACE')
OPEN (UNIT=17,FILE='DIFFMAX.TXT', STATUS='REPLACE')
```

ASSIGN VALUE TO CONSTANTS

```
DELTAT = 0.1                          ! TIME STEP
DELTAX = 0.000003                     ! SPATIAL STEP
NGRID = 51                            ! NUMBER OF GRID POINTS
CONVCR = 0.0002*DELTAT*DELTAX         ! CONVERGENCE CRITERIA FOR
```

```
                                        ! NUMBER OF ITERATIONS
SSCONV = 0.0000001                      ! CONVERGENCE CRITERIA FOR TIME STEPS
RESIDTOL = 0.000001                     ! RESIDUAL TOLERANCE
RELAX = 0.5                             ! RELAXATION FACTOR
DHYD = 0.0384                           ! HYDRAULIC DIAMETER OF TEST SECTION
REYNOLDS = 939                          ! REYNOLDS NUMBER OF AIRFLOW
XSTAR = 0.6/(DHYD * REYNOLDS * 0.6)! DIMENSIONLESS DEVELOPMENT LENGTH

SOLID PROPERTIES OF MEMBRANE
DENS = 950                              ! DENSITY
SVF = 0.45                              ! VOLUME FRACTION
CPS = 1900                              ! SPECIFIC HEAT
KS = 0.48                               ! THERMAL CONDUCTIVITY

MEMBRANE PROPERTIES
POROS = 0.45                            ! DRY POROSITY

AIR PROPERTIES
TA = 295.2                              ! TEMPERATURE
CPA = 1007                              ! SPECIFIC HEAT
KA = 0.026                              ! THERMAL CONDUCTIVITY
DAB = 0.000026                          ! BINARY DIFFUSION COEFFICIENT
RA = 287.0                              ! GAS CONSTANT
RHA = 33                                ! RELATIVE HUMIDITY
VDA = 0.00642                           ! VAPOR DENSITY
ATMP = 95500                            ! ATMOSPHERIC PRESSURE

VAPOR PROPERTIES
CPV = 1862                              ! SPECIFIC HEAT
KV = 0.017                              ! THERMAL CONDUCTIVITY
RV = 462                                ! GAS CONSTANT

WATER PROPERTIES
TW = 290.55                             ! TEMPERATURE
CPW = 4184.0                            ! SPECIFIC HEAT
DENW = 984                              ! DENSITY
HFG = 2455000                           ! HEAT OF VAPORIZATION
KW = 0.650                              ! THERMAL CONDUCTIVITY
VDSAT = 0.01482                         ! SATURATED VAPOR DENSITY

CONSTANTS TO CALCULATE SATURATED WATER VAPOR PRESSURE
C8 = -5800.2206
C9 = 1.3914993
C10 = -0.048640239
C11 = 0.000041764768
C12 = -0.000000014452093
C13 = 6.5459673

INITIAL PROPERTIES
INIT = TW                               ! TEMPERATURE
INIVD = VDSAT                           ! VAPOR DENSITY
INILVF = 0.14                           ! LIQUID VOLUME FRACTION
INIGVF = 0.41                           ! GAS VOLUME FRACTION
INIDENEFF = 320                         ! EFFECTIVE DENSITY
INIM = 0.0                              ! PHASE CHANGE RATE
INIU = 0.01721                          ! MOISTURE ACCUMULATION
```

```
DEFINE PROPERTIES FOR INITIAL TIME STEP
DO 10, I = 1, NGRID
TPREV(I) = INIT
VDPREV(I) = INIVD
LVFPREV(I) = INILVF
GVFPREV(I) = INIGVF
DENEFFPREV(I) = INIDENEFF
MPREV(I) = INIM
UPREV(I) = INIU
VD(I) = INIVD
T(I) = INIT
GVF(I) = INIGVF
LVF(I) = INILVF
M(I) = INIM
U(I) = INIU

10        CONTINUE

START OF TIME LOOP
DO 20, J = 2, NSTEP

START OF ITERATION LOOP
DO 50 K = 1, NITER

START OF POSITION LOOP
DO 40 I = 1, NGRID

ASSIGN PREVIOUS ITERATION VALUES AS THE CURRENT
AND CALCULATE PROPERTIES
VDPI(I) = VD(I)                          ! VAPOR DENSITY FROM PREVIOUS ITERATION
TPI(I) = T(I)                            ! TEMPERATURE FROM PREVIOUS ITERATION

PRESSV(I) = VD(I)*RV*T(I)                ! VAPOR PRESSURE

PVSAT(I) = EXP(C8/T(I) + C9 + C10*T(I) + C11*T(I)**2 + C12*T(I)**3 + C13 * LOG(T(I)))
                                         ! SATURATED VAPOR PRESSURE

RH(I) = PRESSV(I) / PVSAT(I)             ! RELATIVE HUMIDITY

DEFF(I) = 0.000000375                    ! EFFECTIVE DIFFUSIVITY

CALCULATE VAPOR DENSITY THROUGHOUT MEMBRANE
IF(I = 1) THEN                           !WATER/MEMBRANE INTERACE
VD(1) = VDSAT                            !SATURATED WATER VAPOR OF WATER SIDE
ENDIF

IF(I > 1 . AND . I < NGRID) THEN         !INTERNAL NODES IN MEMBRANE

VD(I) = ((DEFF(I+1) - DEFF(I-1)) * (VD(I+1) - VD(I-1)) / (4 * DELTAX**2) + M(I) + DEFF(I) *
          (VD(I+1) + VD(I-1))/(DELTAX**2) + GVF(I) * VDPREV(I) / DELTAT) / ((2 * GVF(I) -
          GVFPREV(I)) / DELTAT + 2*DEFF(I) / (DELTAX**2))

VD(I) = VDPI(I) + RELAX*(VD(I) - VDPI(I))      !RELAX VAPOR DENSITY

ENDIF
```

```
IF(I = NGRID) THEN                          ! AIR/MEMBRANE INTERFACE

RAD = 9.81 * ((DENG(I) + DENAI) / 2) * (DENG(I) -DENAI) * (DHYD**3) * 0.60 / (0.000018**2)
                                            ! RAYLEIGH NUMBER

SH = 0.417 * (ABS(RAD)**0.124) / (XSTAR**0.334)          !SHERWOOD NUMBER

CONVM = SH * DAB / DHYD                     ! CONVECTIVE MASS TRANSFER COEFFICIENT

NU = SH * (0.71 / 0.60) * (DENG(I) - DENAI) * HFG / (((DENG(I) + DENAI) / 2) * CPA * (TA - T(I)))
                                            ! NUSSELT NUMBER

CONVH = NU * KA / DHYD                      ! CONVECTIVE HEAT TRANSFER COEFFICIENT

VD(NGRID) = (-DEFF(NGRID) * (VD(NGRID-2) – 4 * VD(NGRID-1)) / (2 * DELTAX * CONVM) +
                    VDA) / (1 + (3 * DEFF(I) / (2 * DELTAX * CONVM)))
ENDIF
```

CALCULATE PROPERTIES

```
PRESSA(I) = ATMP - PRESSV(I)                ! AIR PRESSURE
DENA(I) = PRESSA(I) / (RA * T(I))           ! AIR DENSITY
DENG(I) = DENA(I) + VD(I)                   ! GAS DENSITY
DENEFF(I) = SVF * DENS + LVF(I) * DENW + GVF(I) * DENG(I)
                                            ! EFFECTIVE MEMBRANE DENSITY
CPG(I) = (DENA(I) * CPA + VD(I) * CPV) / (DENG(I))       !GAS SPECIFIC HEAT
CPEFF(I) = (SVF * DENS * CPS + LVF(I) * DENW * CPW + GVF(I) * DENG(I) * CPG(I)) /
                DENEFF(I)
KG(I) = (DENA(I) * KA + VD(I) * KV) / (DENG(I))!THERMAL CONDUCTIVITY
                                                        !OF GAS PHASE
KEFF(I) = SVF * KS + LVF(I) * KW + GVF(I) * KG(I)               !EFFECTIVE THERMAL
                                                        !CONDUCTIVITY
```

CALCULATE TEMPERATURE THROUGHOUT MEMBRANE

```
IF(I = 1) THEN                              ! WATER/MEMBRANE INTERFACE
T(1) = TW
ENDIF

IF(I > 1 .AND. I < NGRID) THEN              ! INTERNAL NODES IN MEMBRANE
T(I) = (KEFF(I) * (T(I+1) + T(I-1)) / (DELTAX**2) + (KEFF(I+1) - KEFF(I-1)) * (T(I+1) - T(I-1)) / (4 *
        DELTAX**2) - M(I) * HFG + DENEFF(I) * CPEFF(I) * TPREV(I) / DELTAT) / (DENEFF(I) *
        CPEFF(I) / DELTAT + 2 * KEFF(I) / (DELTAX**2))
T(I) = TPI(I) + RELAX * (T(I) - TPI(I))
ENDIF

IF(I = NGRID) THEN                          ! AIR/MEMBRANE INTERFACE (CONVECTIVE HEAT
                                            ! TRANSFER)
T(NGRID) = (-KEFF(NGRID) * (T(NGRID - 2) – 4 * T(NGRID - 1)) / (2 * DELTAX * CONVH) + TA)
/ (1 + (3 * KEFF(I) / (2 * DELTAX * CONVH)))
ENDIF
```

CALCULATE PROPERTIES

```
U(I)=0.0303RH(I)**3-0.02938*RH(I)**2+0.01629    ! ABSORBED PHASE
M(I) = -(U(I) - UPREV(I)) * DRYDEN / DELTAT
LVF(I) = LVFPREV(I) - M(I) * DELTAT / DENW
GVF(I) = 1 – SVF - LVF(I)
```

```
40 CONTINUE                              ! LOOPS TO NEW POSITION POINT
```

DETERMINATION OF CONVERGENCE

```
SUMTEMP1 = 0.0
SUMTEMP1 = SUMTEMP1 + ABS(TPI(I) - T(I))
60      CONTINUE
SUMTEMP2 = 0.0

DO 65, I = 1, NGRID
SUMTEMP2 = SUMTEMP2 +TPI(I)
65      CONTINUE

IF((SUMTEMP1 / SUMTEMP2)<= CONVCR) THEN
GO TO 100
ELSE
GO TO 50
END IF

50      CONTINUE                         ! LOOPS TO NEW ITERATION POINT
100     PRINT*,'TEMP-CONVERGED'
```

CHECK RESIDUAL OF EQUATIONS

RESIDUAL OF TEMPERATURES

```
DO 110, I = 1, NGRID
IF(I=1) THEN                             ! WATER/MEMBRANE INTERFACE
RT1(1) = TW - T(1)
ENDIF

IF(I > 1 .AND. I < NGRID) THEN           ! INTERNAL NODES IN MEMBRANE
RT2(I) = (KEFF(I) * (T(I+1) + T(I-1)) / (DELTAX**2) + (KEFF(I+1) - KEFF(I-1)) * (T(I+1) - T(I-1)) /
          (4 * DELTAX**2) - M(I) * HFG + DENEFF(I) * CPEFF(I) * TPREV(I) / DELTAT) /
          (DENEFF(I) * CPEFF(I) / DELTAT + 2 * KEFF(I) / (DELTAX**2)) - T(I)
ENDIF

IF(I=NGRID) THEN                         ! AIR/MEMBRANE INTERFACE
RT3(NGRID) = (-KEFF(NGRID) * (T(NGRID-2) – 4 * T(NGRID-1)) / (2 * DELTAX * CONVH) + TA)
                / (1 + (3 * KEFF(I) / (2 * DELTAX * CONVH))) - T(NGRID)
ENDIF
```

CALCULATE VAPOR DENSITY RESIDUAL

```
IF(I=1) THEN             !WATER/MEMBRANE INTERACE
RVD1(1) = VDSAT - VD(1)
ENDIF

IF(I > 1 .AND. I < NGRID) THEN  !INTERNAL NODES IN MEMBRANE
RVD2(I) = ((DEFF(I+1) - DEFF(I-1)) * (VD(I+1) - VD(I-1)) / (4 * DELTAX**2) + M(I) + DEFF(I) *
            (VD(I+1) + VD(I-1)) / (DELTAX**2) + GVF(I) * VDPREV(I) / DELTAT) / ((2 * GVF(I)
            - GVFPREV(I)) / DELTAT + 2 * DEFF(I) / (DELTAX**2)) - VD(I)
ENDIF

IF(I=NGRID) THEN        ! AIR/MEMBRANE INTERFACE (CONVECTIVE MASS TRANSFER)
RVD3(NGRID) = (-DEFF(NGRID) * (VD(NGRID-2) – 4 * VD(NGRID-1)) / (2 * DELTAX * CONVM)
                + VDA) / (1 + (3 * DEFF(I) / (2 * DELTAX * CONVM))) - VD(NGRID)
ENDIF
```

```
110       CONTINUE

CHECK FOR CONVERGENCE
RT2TOTAL = 0.0
RVD2TOTAL = 0.0
DO 120, I = 2, NGRID-1
RT2TOTAL = RT2TOTAL + RT2(I)**2
RVD2TOTAL = RVD2TOTAL + RVD2(I)**2

120       CONTINUE

RTTOTAL = SQRT((RT1(1)**2 + RT2TOTAL + RT3(NGRID)**2) / NGRID)
RVDTOTAL = SQRT((RVD1(1)**2 + RVD2TOTAL + RVD3(NGRID)**2) / NGRID)

IF (RTTOTAL<RESIDTOL) THEN
PRINT*,'CONV-TEMP-RESIDUAL'
ELSE
PRINT*,'NONCONV-TEMP-RESIDUAL'
ENDIF

IF (RVDTOTAL<RESIDTOL) THEN
PRINT*,'CONV-VD-RESIDUAL'
ELSE
PRINT*,'NONCONV-VD-RESIDUAL'
ENDIF

MCONV = CONVM * (VDA - VD(NGRID)) * 0.6 * 0.28 * 1000
MINPUT=-(DEFF(1)) * (VD(2) - VD(1)) * 0.6 * 0.28 * 1000 / DELTAX
QCONV = CONVH * (TA - T(NGRID)) * DELTAT
QCOND = -KEFF(1) * (T(2) - T(1)) * DELTAT / DELTAX

MSTORE = 0
QSTORE = 0

DO 145 I = 1, NGRID
MSTORE = MSTORE + DRYDEN * (UPREV(I)-U(I)) * DELTAX * 0.6 * .28 * 1000 / DELTAT
QSTORE = QSTORE + DENEFF(I) * CPEFF(I) * (TPREV(I) - T(I)) * DELTAX

145       CONTINUE

MASSDIFF = (MINPUT + MCONV + MSTORE) * 100 / ((MINPUT – MCONV – MSTORE) / 2)
QDIFF = (QCOND + QCONV + QSTORE) * 100 / ((QCOND – QCONV - QSTORE) / 2)

WRITE DATA TO FILE
WRITE(1,150)J, T(1), T(51), T(101), T(151), T(201), T(251), T(301), (351), T(NGRID)
150       FORMAT(I6, 1X, 9(D15.7, 1X))

WRITE(2, 160)J, VD(1), VD(51), VD(101), VD(151), VD(201), VD(251), VD(301), VD(351),
VD(NGRID)
160       FORMAT(I6, 1X, 9(D15.7, 1X))

WRITE(3, 170)J, LVF(1), LVF(51), LVF(101), LVF(151), LVF(201), LVF(251), LVF(301), LVF(351),
LVF(NGRID)
170       FORMAT(I6, 1X, 9(D15.6, 1X))
```

```
WRITE(4, 180)J, U(1), U(51), U(101), U(151), U(201), U(251), U(301), U(351), U(NGRID)
180       FORMAT(I6, 1X, 9(D15.6, 1X))

WRITE(5, 190)J, MSTORE
190       FORMAT(I6, 1X, 9(D15.6, 1X))

WRITE(6, 200)J, MCONV
200       FORMAT(I6, 1X, 9(D15.6, 1X))

WRITE(7, 210)J, MINPUT
210       FORMAT(I6, 1X, 9(D15.6, 1X))

WRITE(8, 220)J, QSTORE
220       FORMAT(I6, 1X, 9(D15.6, 1X))

WRITE(9, 230)J, QCONV
230       FORMAT(I6, 1X, 9(D15.6, 1X))

WRITE(10, 240)J, QCOND
240       FORMAT(I6, 1X, 9(D15.6, 1X))

WRITE(11, 250)J, MASSDIFF
250       FORMAT(I6, 1X, 9(D15.6,  1X))

WRITE(12, 260)J, QDIFF
260       FORMAT(I6,1X, 9(D15.6, 1X))

WRITE(13, 270)J, M(1), M(51), M(101), M(151), M(201), M(251), M(301), M(351), M(NGRID)
270       FORMAT(I6, 1X, 9(D15.6, 1X))

WRITE(14, 280)J, CONVM
280       FORMAT(I6, 1X, 9(D15.6, 1X))

WRITE(15, 290)J, CONVH
290       FORMAT(I6, 1X, 9(D15.6, 1X))
```

CHECK FOR CONVERGENCE BETWEEN TIME STEPS

```
DIFFMAX = 0
DO 300, I = 1, NGRID
TEMPDIFF(I) = ABS((T(I) - TPREV(I)) / TPREV(I))
VDDIFF(I) = ABS((VD(I) - VDPREV(I)) / VDPREV(I))
IF(TEMPDIFF(I) > DIFFMAX) THEN
DIFFMAX = TEMPDIFF(I)
ENDIF
IF(VDDIFF(I) > DIFFMAX) THEN
DIFFMAX = VDDIFF(I)
ENDIF

300       CONTINUE

IF (DIFFMAX < SSCONV)THEN
GO TO 500
ENDIF
DO 310, I = 1, NGRID
TPREV(I) = T(I)
```

```
VDPREV(I) = VD(I)
LVFPREV(I) = LVF(I)
GVFPREV(I) = GVF(I)
DENEFFPREV(I) = DENEFF(I)
MPREV(I) = M(I)
UPREV(I) = U(I)

310     CONTINUE

WRITE(16,*)J , K
WRITE(17,320)J , DIFFMAX
320     FORMAT(I6, 1X, 9(D15.6, 1X))

20      CONTINUE                        ! LOOPS TO NEW TIME STEP
500     CONTINUE

END
```